Doctoral Dissertation

Application of Satellite Radar Interferometry to Monitoring Subsidence and Slope Displacement Induced by Mining Activities

鉱山採鉱活動に伴う地盤沈下および斜面変位監視に対する干渉 SAR の適用に関する研究

March 2020

I Nyoman Sudi Parwata

Graduate School of Science and Engineering

Yamaguchi University

A dissertation submitted to the Graduate School of Science and Engineering of Yamaguchi University
in partial fulfillment of the requirements for the Degree of Doctor of Engineering

Summary

The mining industry is involved in the excavation of the ground and the extraction of resources from the surface and the underground, human activities which may affect the natural ground and cause it to become unstable. Monitoring ground behavior is important for assessing the stability of the ground. Several useful methods can be employed to measure ground surface displacements, for example, geotechnical instruments, surveying methods, and GPS. Those methods are indeed useful. However, they measure the ground surface displacements only at certain points that have been installed with sensors. If the area to be monitored is very expansive, the number of required devices greatly increases. This leads to high costs and inefficiency. To solve these problems, alternative methods/tools are required.

Differential Interferometric Synthetic Aperture Radar (DInSAR) has the potential to solve the above limitations. On the other hand, there are still issues to be addressed in the practical application of this method for monitoring displacements in rock and geotechnical engineering projects, although the fundamental DInSAR technology has basically been established.

The aim of this study is to investigate the applicability of DInSAR for monitoring surface ground displacements induced by mining activities.

The main objectives of this study are 1) to investigate the effect of different Digital Elevation Models (DEMs) on the displacement measurement results obtained by DInSAR, 2) to evaluate the applicability of DInSAR for monitoring land subsidence induced by salt mining activities, and 3) to assess the advantages and limitations of DInSAR in cases related to landslide phenomena.

The dissertation is composed of seven chapters as follows:

Chapter 1 explains the background, motivations, problem statement, and objectives of this study. The theoretical background and a review of the literature relevant to this study are given in Chapter 2.

In Chapter 3, the applicability of DInSAR for monitoring the slope stability in an open-pit mine is investigated. DInSAR has the potential to be a cost-effective method for monitoring surface displacements in such areas. DInSAR requires an appropriate DEM for its analysis. However, since the topography of the ground surface in open-pit mines changes year by year, measurement errors can occur due to the lack of an appropriate DEM. The effect of different DEMs on the displacement results by DInSAR is investigated at a limestone quarry. And, the accuracy of DInSAR is examined by comparing the DInSAR results with the results obtained by GPS monitoring.

It is verified that the uncertainty of DEMs induces large errors in the displacement monitoring results if the baseline length of the satellites is long. After comparing the monitoring results of DInSAR and GPS, it is found that the root mean square error (RMSE) of the discrepancy between the two sets of results is less than 10 mm. DInSAR can be applied for monitoring the displacements of mine slopes with centimeter-level accuracy by using an updated DEM and selecting SAR data with short perpendicular baselines of less than 100-150 m (for L-band SAR data).

In Chapter 4, an advanced time-series analysis, Small Baseline Subset DInSAR (SBAS-DInSAR), proposed by Berardino et al. (2002), is applied for monitoring the subsidence induced by extracting salt water from underground salt deposits in Tuzla City, Bosnia and Herzegovina. The main purpose of this chapter is to enhance the former studies on the subsidence in this city and to investigate whether SBAS-DInSAR could be a better method for monitoring the subsidence. The SBAS-DInSAR results are evaluated by the results of a GPS survey. It is found that the subsidence obtained by GPS coincides with that obtained by SBAS-DInSAR within just a few cm.

SBAS-DInSAR can be used as a cost-effective tool and sustainable ground subsidence monitoring method. Recently, Sentinel-1A and -1B satellites provide SAR data continuously every 6-12 days. The main limitation of Sentinel-1 data is high decorrelation in vegetated areas. This limitation can be solved by combining SAR data images with longer wavelengths provided by ALOS-2 data. However, the number of ALOS-2 images is very limited and only 3-5 SAR images can be obtained for such areas in a year. Thus, this is a limitation that still needs to be addressed.

In Chapter 5, SBAS-DInSAR is applied to two cases of monitoring landslide displacements located near a residential area. In the first case, it is found that this method shows a good applicability for monitoring slow displacement behavior of a few centimeters a year. However, due to the geometrical relationship between the Line of Sight (LOS) of the satellite and the displacement direction, it has low sensitivity when measuring displacements in the north-south direction. This is explained through a comparison of displacements measured by SBAS-DInSAR and GPS. In the second case, SBAS-DInSAR is applied to a slope where a landslide failure has occurred, in order to investigate whether any signs of slope failure can be detected. It is found that the SBAS-DInSAR method cannot detect a clear sign of sudden large displacements or failure.

In Chapter 6, a new fundamental equation for InSAR, derived by the author and his colleagues, is presented and verified using SAR data. The equation is newly formulated

based on a different concept from that of the original InSAR. Practical applications will be the target of future work.

The general conclusions of this study and recommendations for future research are given in Chapter 7. The chapter includes the significant findings of this study and the remaining issues which will comprise future studies.

Acknowledgments

This study could not have been completed without the financial support of the Remote Sensing Research Group of Yamaguchi University, Yamaguchi University scholarship for self-financed students, and research funding from my supervisor, Professor Norikazu Shimizu. I am very grateful for having obtained all of the above financial support.

I would like to express my sincere gratitude to my supervisor, Professor Norikazu Shimizu, for his kind support, constant motivation, knowledge, and assistance during my years of doctoral study and also my daily life in Ube, Japan. He is the key person who contributed the most to the accomplishments I have achieved during my doctoral study.

I also want to thank my second supervisor, Associate Professor Shinichiro Nakashima, for his invaluable suggestions and comments during my doctoral study. He has been the best partner in research discussions and in relation to various technical problems encountered in our Shimizu Laboratory.

Besides my supervisors, I would like to offer my sincere thanks to the members of the examination committee for reviewing my dissertation, namely, Professor Masahiko Nagai, Professor Toshihiko Aso, Professor Yukio Nakata, and Professor Motoyuki Suzuki. Their comments and suggestions were very important and useful for improving my dissertation manuscript.

My gratitude and special thanks are given to Uesaka-san and Furukawa-san for their support in administrative and official matters during my study. The most important assistance I received with these matters was from Uesaka-san when applying for the scholarship which required writing “Kanji” in the application process. I will never forget her kindness and support.

I also thank the lab members for creating such an amazing and comfortable research atmosphere and for all the enjoyable times we had for over three years, Edi, Kien, Oka, Kawamoto-Sensei, Yoshida, Tochigi, Yamato, Ozawa, Kameyama, Ueno, Kodama, Shigetani, Kiso, Koumoto, Tsunemine, Shimai, and Shigehiro. I also thank other friends who have already graduated, namely, Amafuji, Terada, Sakamoto, Taguchi, Okuda, Hayashi, and Nichihara.

I thank Professor Tasuku Tanaka for his hard work, dedication, and contributions during my study. He was the key person in bringing me to Japan.

Last, but most important to my life, I offer special thanks to my beloved wife, Ni Made Cintya Dwi Pramesti, and our son, Made Takumi Parwata. I appreciate the patience, support,

help, and love they provide in my life. Thanks also goes to my parents and other family members. Thank you all so very much.

Table of Contents

List of Tables

List of Figures

List of Abbreviations

3-D	Three-Dimensional
ALOS-PALSAR	Advanced Land Observing Satellite Phased Array Type of L-band Synthetic Aperture Radar
ALOS-PALSAR-2	Advanced Land Observing Satellite Phased Array Type of L-band Synthetic Aperture Radar-2
ASTER-GDEM	Advanced Spaceborne Thermal Emission and Reflection Radiometer Global Digital Elevation Model
AW3D30-DEM	ALOS World Three-Dimensional 30-meter Resolution Digital Elevation Model
DEM	Digital Elevation Model
DInSAR	Differential Interferometry Synthetic Aperture Radar
ESA	European Space Agency
GNSS	Global Navigation Satellite System
GPS	Global Positioning System
GSI	Geospatial Information Authority of Japan
InSAR	Interferometry Synthetic Aperture Radar
JAXA-EORC	Japan Aerospace Exploration Agency Earth Observation Research Center
LOS	Line of Sight
MCF	Minimum Cost Flow
PRISM	Panchromatic Remote-Sensing Instrument for Stereo Mapping
RMSE	Root Mean Square Error
SAR	Synthetic Aperture Radar
SBAS-DInSAR	Small BAseline Subset Differential Interferometry Synthetic Aperture Radar
SIR-C/X-SAR	Spaceborne Imaging Radar C/X-band Synthetic Aperture Radar
SLC	Single Look Complex
SRTM	Shuttle Radar Topography Mission
SVD	Singular Value Decomposition
TOPSAR	Terrain Observation with Progressive Scans SAR
WGS84	World Geodetic System 1984

List of Symbols

$\boldsymbol{A}$	Matrix of $M \times N$ (M is number of interferograms and N is number of SAR images)
$\boldsymbol{B}$	Matrix of $M \times N$ (M is number of interferograms and N is number of SAR images) for SBAS-DInSAR considering mean displacement velocity.
b	Satellite baseline
$b_{\perp}$	Perpendicular baseline
$b_{\perp,critical}$	Critical perpendicular baseline
c	Speed of light
D_{E-W}	Displacement provided by GPS in east-west direction
D_{LOS}	Displacement in satellite's line of sight direction
D_{N-S}	Displacement provided by GPS in north-south direction
D_{Sub}	Displacement in vertical direction (subsidence)
D_{U-D}	Displacement provided by GPS in up-down direction
H	Satellite altitude
IE	Master image
IS	Slave image
M	Number of interferograms
N	Number of SAR images
r	Slant range distance
S_1	Satellite position at first acquisition
S_2	Satellite position at second acquisition
T	Measured at specific point
t_0	First acquisition of SAR data
t_N	SAR data acquisition at specific time
$\boldsymbol{v}$	Mean phase velocity between time-adjacent acquisitions
W	SAR system bandwidth
Z	Ground surface elevation
α	Angle between baseline and horizontal plane
β	Satellite heading angle
λ	SAR wavelength

ϑ	Satellite look angle
ϑ_i	Local incident angle
φ	InSAR phase difference
φ_{flat}	Flat-Earth phase
φ_{topo}	Phase due to topography
σz	Standard deviation of estimated topographic height by InSAR
$\sigma\varphi_{topo}$	Error of InSAR phase measurement
Δr	Slant range difference
$\Delta\varphi$	DInSAR phase
$\Delta\varphi_{atm}$	Phase component due to variation in propagation conditions of atmospheric conditions (including ionospheric and tropospheric delays)
$\Delta\varphi_{disp}$	Phase due to surface displacement
$\Delta\varphi_{noise}$	Phase due to all phase noise contributions
$\Delta\varphi_{orb}$	Residual phase due to use of inaccurate satellite orbital data
$\Delta\varphi_{scatt}$	Phase component due to changes in scattering behavior
$\Delta\varphi_{topo}$	Residual topography phase due to DEM error
ΔZ	DEM error
$\Delta z'$	Elevation difference between InSAR-DEM and other DEMs

Chapter 1. Introduction

1.1 Background

Monitoring ground surface displacements due to natural phenomena or human activities is very important. Several useful methods can be applied to measure ground surface displacements, for example, field surveying, leveling, GPS surveying, etc. These methods provide highly accurate measurement results (centimeter- to millimeter-level accuracy). However, the methods measure the ground surface displacements only at certain points and in limited areas (a few hundred square meters). If the area to be monitored is large (several square kilometers), the number of required devices greatly increases. This leads to high costs and inefficiency. To solve these problems, alternative methods or tools are required.

Interferometric Synthetic Aperture Radar (InSAR) has the high potential to solve the above limitations. InSAR is widely used for ground surface topographic estimation and surface displacement monitoring. Due to its ability to monitor ground surface displacements independent of sun illumination and weather conditions, InSAR can be used as a continuous monitoring tool.

The first application of InSAR was to estimate the topographic height of the ground surface (Graham, 1974; Zebker and Goldstein, 1986). The capability of InSAR to map the world topographically was proven by the performances of Shuttle Radar Topography Mission (SRTM) (Rabus et al., 2003) and TerraSAR-X (Tandem-X) (Zink, 2015).

More recent applications of InSAR have been to measure ground surface displacements with a method referred to as Differential Interferometric Synthetic Aperture Radar (DInSAR). The application of DInSAR for measuring ground surface displacements has been reported in research works related to many topics, such as ground subsidence (Chaussard et al., 2014; Moghaddam et al., 2013; Stramondo et al., 2008), slope stability and landslides (Liu et al., 2016a; Rott and Nagler, 2006; Singhroy and Molch, 2004), volcanic activities (Chen et al., 2017; Tomiyama et al., 2004; Wnuk and Wauthier, 2017), and displacements due to earthquakes (Klein et al., 2017; Wang et al., 2017).

The above-mentioned applications were mostly performed over vast areas of several hundred square kilometers. Although DInSAR is capable of measuring large areas, discussions on how DInSAR can be applied to small areas (a few square kilometers) should be promoted.

In addition to the advantages of DInSAR, there are also some limitations which must be considered. The measurement accuracy of DInSAR is affected by several errors which are related to the measurement results, such as satellite orbit data inaccuracy, DEM inaccuracy, atmospheric delays, the chances of a target's scattering behavior, and other noises.

In this thesis, the study is focused on the application of DInSAR to the measurement and interpretation of surface displacements, such as ground subsidence and slope displacements induced by mining activities.

This chapter provides a problem statement, research objectives, and thesis organization.

1.2 Problem statement

DInSAR requires an appropriate digital elevation model (DEM) for its analysis. In this study, the first research location is an open-pit mine. Since the topography of the ground surface in open-pit mines changes largely, measurement errors can occur due to the lack of an appropriate DEM. The effect of DEM inaccuracy on the DInSAR results should be evaluated. DInSAR has usually been applied to vast areas of more than several hundred square kilometers, but its applicability to areas of only a few square kilometers, like mining regions, also needs to be investigated.

Underground mining activities near residential areas tend to have negative impacts. One common problem is ground subsidence. There are several conventional tools and methods for monitoring ground subsidence, for example, field surveying, optical leveling, GPS surveys, etc. However, these methods measure the ground subsidence only at certain points and in limited areas. If the ground subsidence is large and requires continuous monitoring, it leads to high costs and inefficiency. The applicability of DInSAR as a powerful tool or a cost-effective method with sustainable monitoring ability needs to be evaluated.

It is important to conduct an investigation of the advantages and limitations of DInSAR to monitor slope stability and landslides. Few comprehensive discussions have been reported on how DInSAR can measure slope displacements if slope failures (landslides) occur during the measurement period.

There are still fundamental issues related to the formulation of InSAR for mapping the topography which must be addressed. A new formulation is proposed for future advances in InSAR technology.

1.3 Research objectives

The main objectives of this thesis are as follows:

1. To investigate the effect of different DEMs on the displacement measurement results obtained by DInSAR (Chapter 3).
2. To evaluate the applicability of SBAS-DInSAR for monitoring land subsidence induced by mining activities (Chapter 4).
3. To assess the advantages and limitations of SBAS-DInSAR in two cases related to slope displacements and landslide phenomena (Chapter 5).
4. To propose a new equation for use in the process of InSAR to determine the topographic height (Chapter 6).

1.4 Thesis organization

This thesis is organized as follows:

Chapter 1 explains the background, motivations, problem statement, and objectives of this study.

Chapter 2 provides the theoretical background and a review of the literature relevant to this study. This chapter explains the basic concepts of SAR, InSAR for measuring the ground surface topography, and DInSAR for measuring ground surface displacements. The key idea and main steps of a displacement time-series analysis by the Small BAseline Subset (SBAS) are explained in this chapter.

Chapter 3 focuses on investigating the effect of different Digital Elevation Models on the displacement measurement results by DInSAR. This chapter provides an application of DInSAR for monitoring the displacements in a small open-pit mine. An assessment and an evaluation of the DInSAR results using precise GPS are presented in this chapter.

Chapter 4 presents the applicability of SBAS-DInSAR for monitoring the land subsidence induced by salt mining activities. In this chapter, the performance of SBAS-DInSAR is evaluated as a powerful tool and sustainable monitoring system.

Chapter 5 provides a discussion on the advantages and limitations of DInSAR using two case studies. The cases presented in this chapter are related to slope stability monitoring and landslide phenomena. The chapter focuses on evaluating the advantages and limitations of DInSAR in measuring slope displacements and landslide occurrences.

Chapter 6 presents a new concept and fundamental equation for use with InSAR for estimating the topographic height. A comparison of the original InSAR and the new InSAR approaches are presented. The new InSAR approach is also tested using real satellite data.

Chapter 7 presents the general conclusions of this study, followed by suggestions for future research works.

Chapter 2. Theoretical Background and Literature Review

This chapter presents the basic concept or theoretical background relevant to all the studies in this dissertation. The chapter also consists of a review of several high-quality research articles related to the dissertation. The aim of this chapter is to know the state of the art of DInSAR and to summarize the remaining issues.

2.1 Theoretical background

This section presents the basic concepts of SAR, InSAR, and DInSAR. An overview of the basic rationale of SBAS-DInSAR is presented, followed by an explanation of the main steps in a SBAS-DInSAR analysis. The last part of theoretical background is the geometrical projection of 3-dimensional displacements into LOS displacements and the conversion of LOS displacements into vertical displacements (such as subsidence).

2.1.1 Basic concept of SAR

Synthetic Aperture Radar (SAR) consists of a radar device mounted on an aircraft or artificial satellite that transmits microwaves to the Earth's surface, observes the intensity and phase of the reflected waves from the surface, and generates high-resolution imagery (Hanssen, 2001). It can be operated all day and all night, and is independent of the weather conditions. SAR is a side-looking imaging system, as shown in Figure 2.1.

Interferometry SAR (InSAR) is a method for taking the signal phase difference from two scenes of SAR data (Bürgmann et al., 2000; Massonnet and Feigl, 1998), which are observed in the same area at different times. InSAR can be used to create a topography map of the ground under certain conditions (Bürgmann et al., 2000; Graham, 1974; Massonnet and Feigl, 1998; Rocca et al., 2000). Differential InSAR (DInSAR) can measure the changes in the distance between the radar and the ground surface after removing the topographic contribution from the interferograms (Ferretti et al., 2007). The advantage of DInSAR is that the distribution of the ground surface displacements in the direction of the microwave radiation can be observed over vast areas with a spatial resolution of 3-30 m without the necessity for installing any devices on the ground.

In this section, outlines of InSAR and DInSAR are given to clarify the focus of this study.

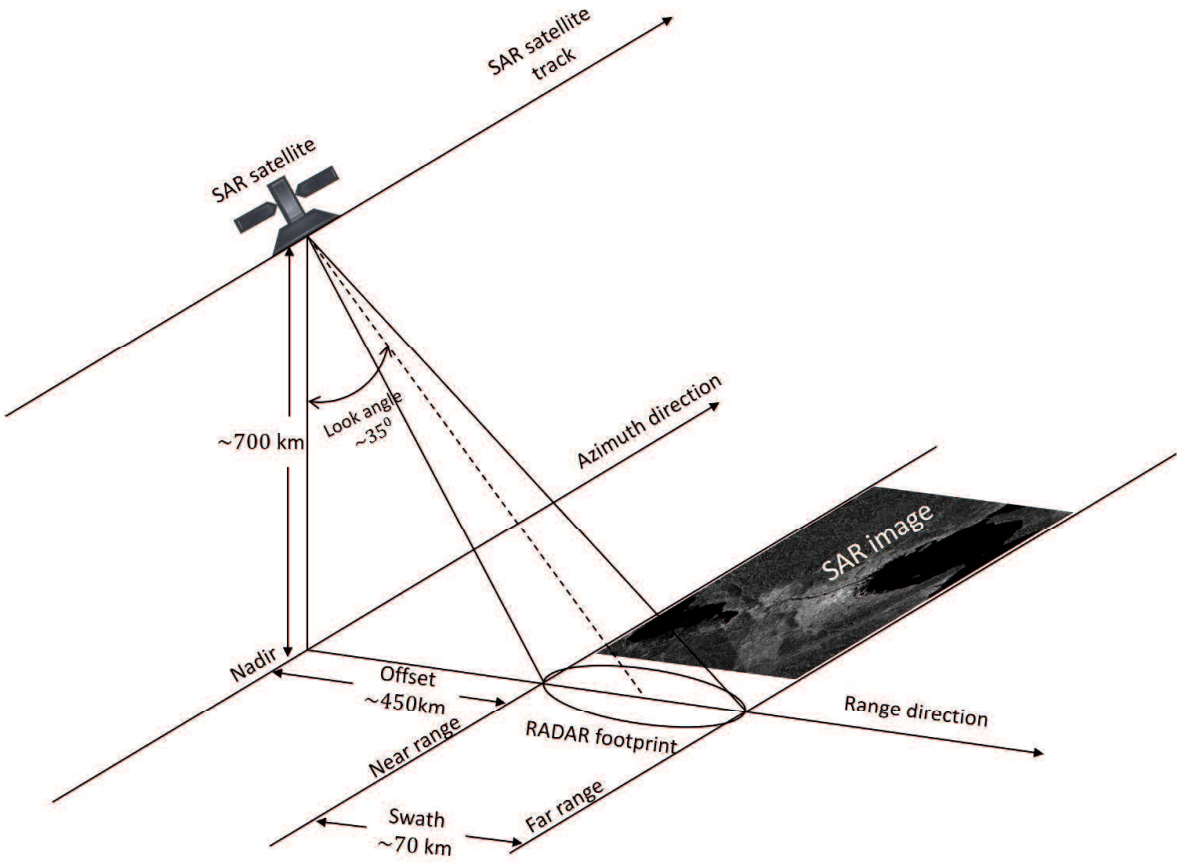

Figure 2.1. Side-looking geometry of SAR satellite (figure was created based on specifications of ALOS-PALSAR strip map in fine resolution mode).

2.1.2 InSAR technique to measure topography of Earth's surface

Supposing a SAR satellite acquires two sets of SAR data over the same area at different times, the first SAR data set comprises the master data and the second set comprises the slave data (Massonnet and Feigl, 1998; Pepe and Calò, 2017). The phase difference φ between the reflection waves of the two sets of SAR data can be expressed considering the geometrical relation among the master satellite position, the slave satellite position, and a point on the Earth's surface (Figure 2.2), as follows (Pepe and Calò, 2017):

$$\varphi \simeq -\frac{4\pi}{\lambda} b \sin(\vartheta_0 - \alpha) - \frac{4\pi}{\lambda} \frac{b_\perp}{r \sin\vartheta} z \tag{2.1}$$

where φ is the phase difference observed by the master and slave satellite positions, whose value is between $-\pi$ and π (Ferretti et al., 2007). λ is the wavelength of each microwave transmitted from the satellites, b is the baseline length (the distance between satellite positions M and S), r is the distance between a satellite and a point T on the ground surface, ϑ_0 indicates the side-looking angle for transmitting the microwaves from the satellites that correspond to the case when the Earth's surface is flat (i.e., $z = 0$), ϑ is the side-looking angle

that corresponds to the case when the Earth's surface is not flat (i.e., $z \neq 0$), α is the inclination angle of the baseline with respect to the horizontal direction, $b_\perp$ is the perpendicular baseline length, and z is the topographic height or elevation (see Figure 2.2) (Pepe and Calò, 2017).

The right side of Eq. (2.1) is created by two phase forms, namely, flat-Earth component φ_{flat} and topographic phase component φ_{topo}, as follows (Pepe and Calò, 2017):

$$\varphi_{flat} = -\frac{4\pi}{\lambda} b \sin(\vartheta_0 - \alpha) \tag{2.2}$$

$$\varphi_{topo} = -\frac{4\pi}{\lambda} \frac{b_\perp}{r \sin\vartheta} z \tag{2.3}$$

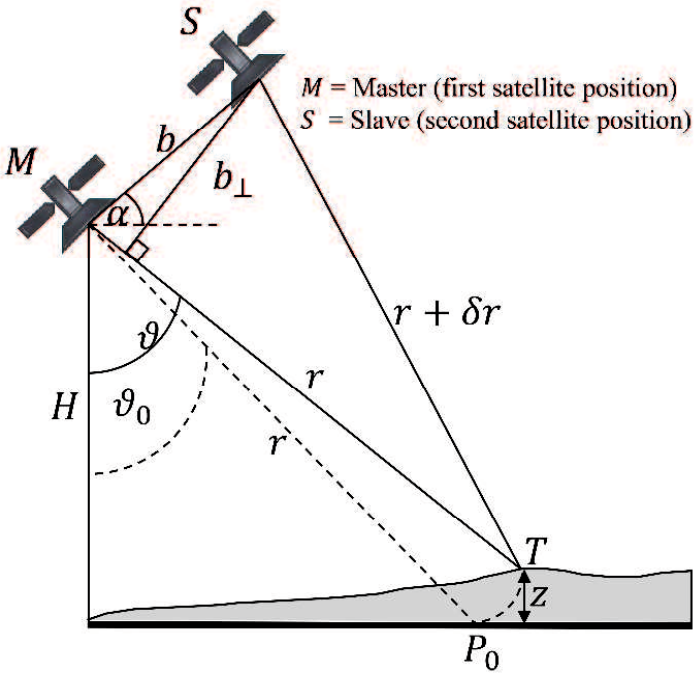

Figure 2.2. InSAR geometry (Pepe and Calò, 2017).

From Eq. (2.1), topographic height z can be estimated from observed phase difference φ by removing flat-Earth phase component φ_{flat}, as follows (Hanssen, 2001; Pepe and Calò, 2017):

$$z = -\frac{\lambda}{4\pi} \frac{r \sin\vartheta}{b_\perp} (\varphi - \varphi_{flat}) \tag{2.4}$$

The phase value of $(\varphi - \varphi_{flat})$ is still between $-\pi$ and π. In order to estimate topographic height z using Eq. (2.4), the phase $(\varphi - \varphi_{flat})$ is integrated to obtain the absolute value. This process is called "phase unwrapping" (Ferretti et al., 2007).

From Eq. (2.4), it can be seen that a longer perpendicular baseline $b_\perp$ produces a more accurate topographic height estimation. It can be expressed as the standard deviation of the estimated topographic height (σz), as follows (Pepe and Calò, 2017):

$$\sigma z = -\frac{\lambda}{4\pi}\frac{r \sin\vartheta}{b_\perp}\sigma\varphi_{topo} \tag{2.5}$$

where $\sigma\varphi_{topo}$ is the error in the InSAR phase measurement. Eq. (2.5) indicates that a longer perpendicular baseline length $b_\perp$ produces a more accurate estimated topographic height. However, there is a limit value for perpendicular baseline length $b_\perp$, referred to as critical baseline $b_{\perp,critical}$, which can be expressed as follows (Bamler, 1997):

$$b_{\perp,critical} = \frac{\lambda \cdot W \cdot r \cdot tan(\vartheta - \alpha)}{c} \tag{2.6}$$

where W is the SAR system bandwidth and c is the speed of light. Once perpendicular baseline $b_\perp$ exceeds critical perpendicular baseline $b_{\perp,critical}$, the interferometric phase is completely decorrelated and useless as a topographic height estimation.

Figure 2.3 depicts a plot of the standard deviations in estimated topographic height Δz and perpendicular baseline $b_\perp$, calculated by Eq. (2.5).

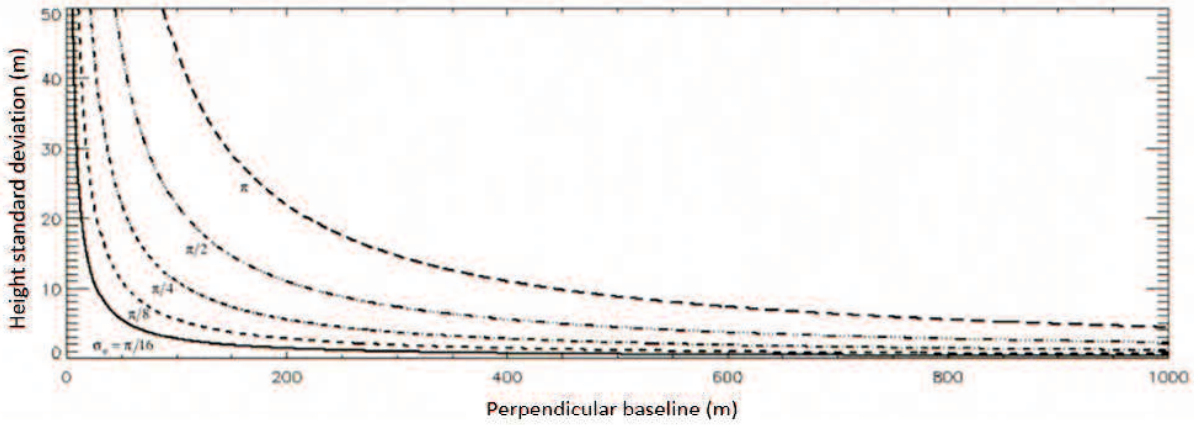

Figure 2.3. Relationship between perpendicular baseline and height standard deviations (Pepe and Calò, 2017).

The topographic height estimation by InSAR was successfully demonstrated in 1986 using SAR sensors mounted on an aircraft (Zebker and Goldstein, 1986). The topographic

mapping on a global scale using InSAR (spaceborne and satellite-based) was effectively presented by Shuttle Radar Topography Mission (SRTM) (Rabus et al., 2003) and TerraSAR-X (Tandem-X) (Zink, 2015).

2.1.3 Differential InSAR to measure displacements of Earth's surface

Differential InSAR (DInSAR) is a technique for measuring the displacements of the Earth's surface; it is based on the process of InSAR. Removing topographic component φ_{topo} and flat-Earth phase component φ_{flat} (see Eqs. (2.2) and (2.3)) from observed phase difference φ, the remaining phase can be expressed as follows (Pepe and Calò, 2017):

$$\Delta\varphi = \frac{4\pi}{\lambda} D_{LOS} + \Delta\varphi_{topo} + \Delta\varphi_{orb} + \Delta\varphi_{atmo} + \Delta\varphi_{scatt} + \Delta\varphi_{noise} \tag{2.7}$$

where $\Delta\varphi = \varphi - \varphi_{topo} - \varphi_{flat}$ can be computed by the observed φ and Eqs. (2.2) and (2.3). D_{LOS} is the unknown ground surface displacement in the direction between a satellite and the Earth's surface, which is called the Line of Sight (LOS) displacement. $\Delta\varphi_{topo}$ is the residual phase due to the error in the topographic elevation of the Earth's surface, $\Delta\varphi_{orb}$ is the residual phase due to the use of an inaccurate satellite orbital position, $\Delta\varphi_{atmo}$ is the effect of the atmospheric phase delay, $\Delta\varphi_{scatt}$ indicates the phase scatter due to changes in the conditions on the ground surface, and $\Delta\varphi_{noise}$ is the phase due to the noise contribution. The phase unwrapping process is applied to phase $\Delta\varphi$ to compute the LOS displacement, d_{LOS}, in a similar manner to that given in section **2.1.2.**

Focusing on the errors due to the residual topography, $\Delta\varphi_{\mathrm{topo}}$, they can be expressed as follows:

$$\Delta\varphi_{topo} = -\frac{4\pi}{\lambda}\frac{b_{\perp}}{r\,sin\,\vartheta}\,\Delta Z \tag{2.8}$$

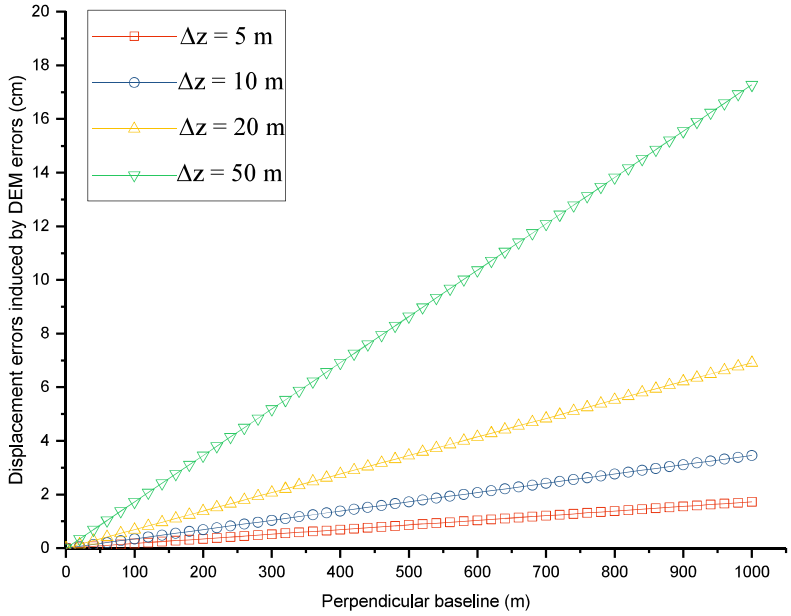

Figure 2.4. Relationship between LOS displacement errors induced by DEM errors ΔZ and perpendicular baseline ($b_\perp$).

Figure 2.4 shows the deformation errors induced by the DEM errors based on Eq. (2.8). In the ALOS-PALSAR case, r is about 865 km and the incidence angle (ϑ) = 34.4 degrees. If $b_\perp$ is small (near zero), there is almost no effect of the DEM errors on the displacement. Conversely, a longer $b_\perp$ length introduces larger errors to the monitored displacements. The best way to reduce the effect of DEM errors is to use SAR image pairs with small or near zero $b_\perp$. However, in the ALOS-PALSAR case, the number of image pairs with near zero $b_\perp$ is very limited, since the ALOS-PALSAR orbit tube is about 3 km (even in 2007, it had decreased to 1 km) (Sandwell et al., 2008). This kind of residual topography error is discussed comprehensively in Chapter 3.

D_{LOS} is obtained from Eq. (2.7), while $\Delta\varphi_{topo}, \Delta\varphi_{orb}, \Delta\varphi_{atmo}, \Delta\varphi_{scatt}$, and $\Delta\varphi_{noise}$ are included as errors. If the errors can be removed completely, the displacement in the LOS direction can be calculated as follows:

$$D_{LOS} = \frac{4\pi}{\lambda} \cdot \Delta\varphi \tag{2.9}$$

This is the fundamental procedure of DInSAR for measuring displacements of the Earth's surface. The procedures for InSAR and DInSAR are outlined in Figure 2.5 (Franceschetti and Lanari, 1999; Hein, 2004).

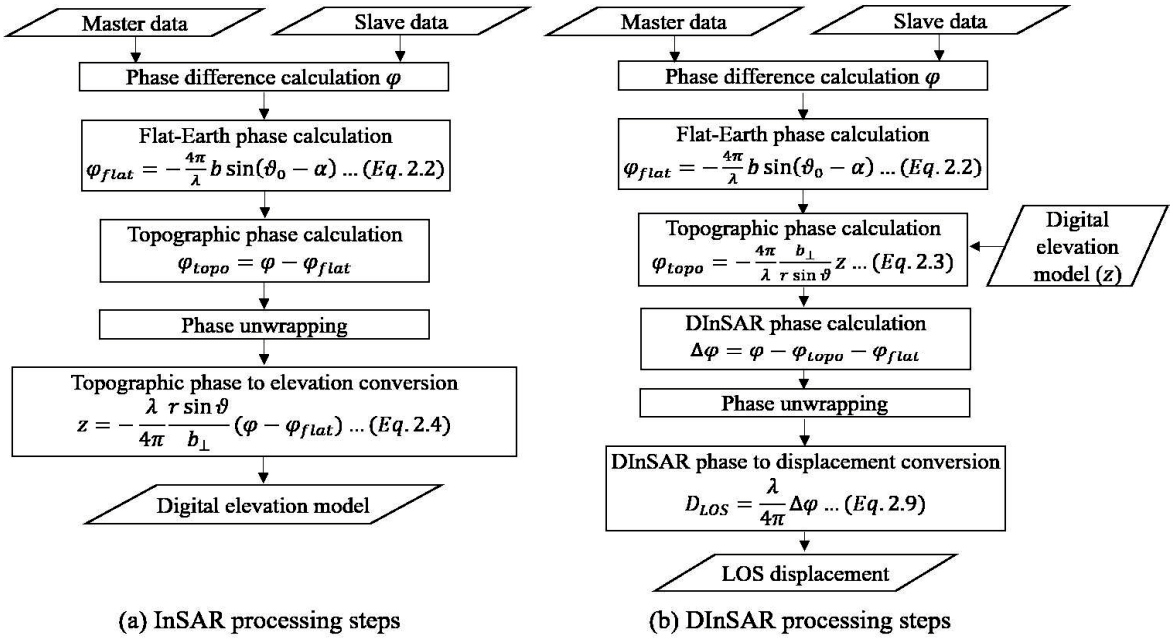

Figure 2.5. Outline of processing steps for InSAR and DInSAR: (a) InSAR for obtaining a digital elevation model and (b) DInSAR for obtaining surface displacements.

2.1.4 Overview of SBAS-DInSAR

The interferograms produced by a single SAR data pair (DInSAR) tend to be affected by noises, as shown by Eq. (2.7). Such errors can be reduced by using multiple SAR pairs and the stacking process (i.e., DInSAR time-series approaches). Several DInSAR time-series algorithms have been developed. One such algorithm was proposed by Ferretti et al. (2000) and is referred to as the Permanent Scatterers (PS) method. Another algorithm was proposed by Berardino et al. (2002) and is referred to as the Small BAseline Subset method (SBAS).

In this study, the SBAS method is employed to generate time-series displacements. This method employs a simple combination of interferograms produced by multiple SAR data pairs. The SAR data pairs are characterized by small spatial and temporal baselines. The key objective of the selection of SAR data pairs with small spatial and temporal baselines is to mitigate the decorrelation phenomena and maximize the number of pixels exploited (Tizzani et al., 2007).

This section briefly summarizes the basic rationale of the SBAS method and provides a short explanation of the main steps involved in implementing the approach. The availability of a set of $N + 1$ SAR data images relevant to the same area is supposed and then acquired at ordered times $(t_0, \ldots, t_N)$. Those SAR data images are co-registered with respect to a single SAR data image (referred as the super master) in order to obtain a common reference grid.

The SBAS analysis is started from an unwrapped interferogram, referred to as M. M interferograms can be produced as $\Delta\varphi_1, \dots, \Delta\varphi_M$. Let us now refer to a pixel of SAR images with azimuth and range coordinates (x, y), respectively. Assume that the unwrapped interferograms are calibrated using at least one known displacement value (reference point). Usually the reference point is located in a stable area with zero displacement (stable point).

The expression of the $j-th$ unwrapped interferogram produced by the SAR images acquired at time t_B and t_A is as follows (Berardino et al., 2002):

$$\Delta\varphi_j(x,r) = \varphi(t_B,x,r) - \varphi(t_B,x,r), \qquad \forall j = 1,\dots,M \tag{2.10}$$

where $\varphi(t_B, x, r)$ and $\varphi(t_A, x, r)$ are the phases of the SAR images acquired at times t_B and t_A, respectively, and with respect to t_0 assumed as a reference. In this case, $\varphi(t_0, x, r)$=0, $\forall(x, r)$.

Let

$$\varphi^T = [\varphi(t_1), \dots, \varphi(t_N)] \tag{2.11}$$

be the vector of the N (unknown) phase values associated with the displacement of the considered pixel and

$$\Delta\varphi^T = [\Delta\varphi_1, \dots, \Delta\varphi_M] \tag{2.12}$$

be the vector of the M (known) values of the computed unwrapped interferograms.

The following two vectors are then defined as

$$IE = [IE_1, \dots, IE_M], \quad IS = [IS_1, \dots, IS_M] \tag{2.13}$$

where IE represents the master images and IS represents the slave images in chronological order, i.e., $IE_j > IS_j, \forall j = 1, \dots, M$. From these index vectors, Eq. (2.10) can be rewritten as follows:

$$\Delta\varphi_j(x,r) = \varphi\left(t_{IE_j}\right) - \varphi\left(t_{IS_j}\right), \qquad \forall j = 1,\dots,M \tag{2.14}$$

Eq. (2.14) defines a system of M equations for N unknowns which can be recognized by using matrix formalism, namely,

$$\boldsymbol{A} \cdot \varphi = \Delta\varphi \tag{2.15}$$

Matrix **A** is an M × N matrix for which $\forall j = 1, \dots, M$. It makes $\mathbf{A}\left(j, IS_j\right) = -1$ if $IS_j \neq 0$, $\mathbf{A}\left(j, IE_j\right) = +1$ and 0 otherwise. For instance, if $\Delta\varphi_1 = \varphi_4 - \varphi_2$ and $\Delta\varphi_2 = \varphi_3 - \varphi_0$, then **A** will have the following form:

$$\mathbf{A} = \begin{bmatrix} 0 & -1 & 0 & +1 & \dots \\ 0 & 0 & +1 & 0 & \dots \\ \dots & \dots & \dots & \dots & \dots \\ \dots & \dots & \dots & \dots & \dots \end{bmatrix} \tag{2.16}$$

Note that **A** is an incidence-like matrix, directly depending on the set of interferograms generated from the available data. Due to this characteristic, if all the acquisitions belong to a single subset, it turns out that M ≥ N and **A** is an N-rank matrix. If the acquisitions belong to two or more subsets, an additional mathematic formulation, i.e., the Singular Value Decomposition (SVD), should be performed to solve this problem. A more detailed explanation of the SVD operation in the SBAS-DInSAR concept can be found in Berardino et al. (2002).

In this study, all acquisitions belong to a single subset and the SBAS-DInSAR with a linear model is employed. The SBAS considering the mean displacement velocity between time-adjacent acquisitions is applied and can be expressed as follows:

$$\mathbf{B}v = \Delta\varphi \tag{2.17}$$

where **B** is an M × N matrix and v is the mean phase velocity between time-adjacent acquisitions. It can be expressed as follows:

$$v^T = \left[v_1 = \frac{\varphi_1}{t_1 - t_0}, \dots, v_N = \frac{\varphi_N - \varphi_{N-1}}{t_N - t_{N-1}}\right] \tag{2.18}$$

The M × N matrix in Eq. (2.17) defines several elements, as follows:

$$B[j,k] = \begin{cases} t_{k+1} - t_k & IS_j \leq k \leq IE_j, \quad \forall j = 1, \dots, M \\ 0 & elsewhere \end{cases} \tag{2.19}$$

2.1.5 Main steps of SBAS-DInSAR

The main steps of the SBAS method are shown in Figure 2.6 (Lanari et al., 2007); each step will be explained briefly.

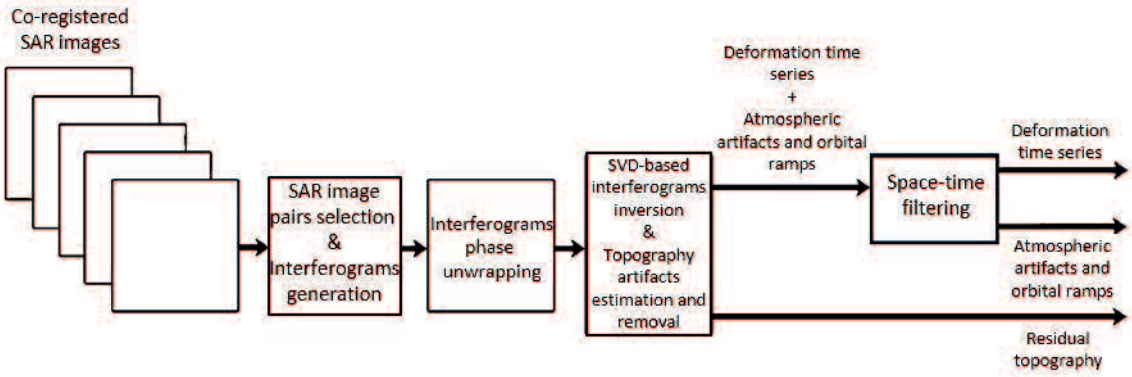

Figure 2.6. Block diagram of SBAS algorithm (Lanari et al., 2007).

a) Selection of SAR data pairs. The first step of the SBAS process is the selection of SAR data pairs done by giving threshold values to the temporal and spatial baselines. This process will produce a graph showing the possible pairs that will be analyzed after assigning the baseline thresholds (spatial and temporal baselines), as seen by Figure 2.7.

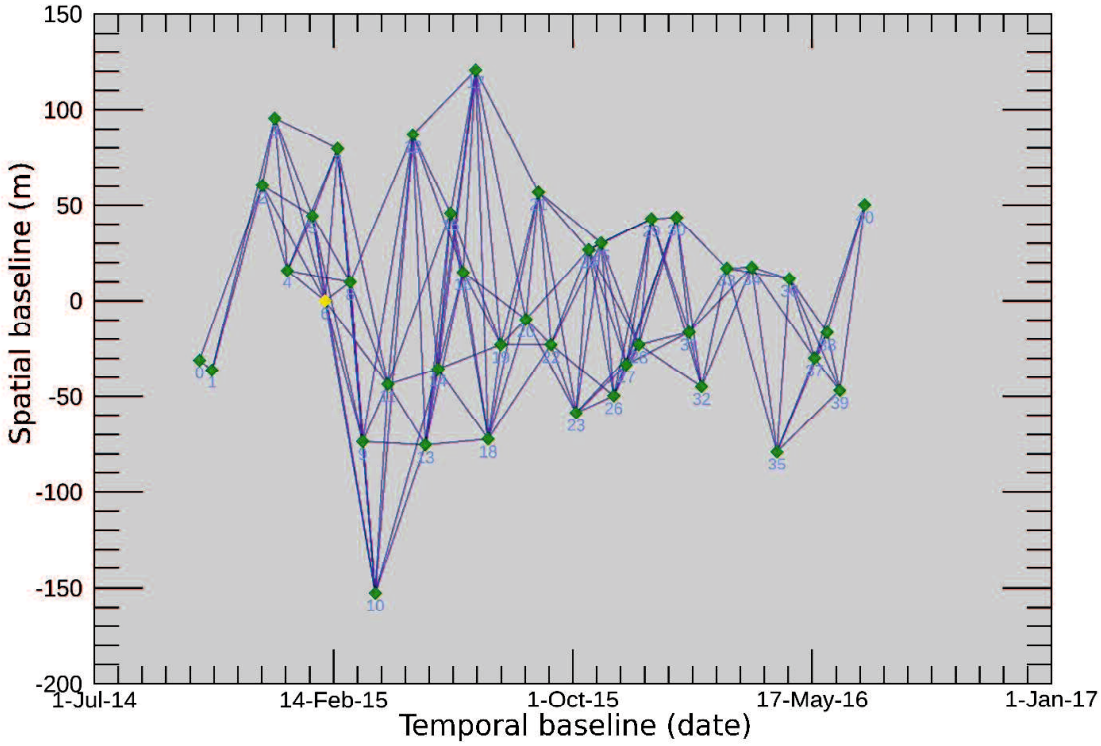

Figure 2.7. Plot of spatial and temporal baselines of SBAS-DInSAR.

All the SAR images are shown by diamonds. The super master is indicated by the yellow diamond. In total, there are 41 SAR images in Figure 2.7. The lines indicate the possible combinations of SAR data pairs. In this case, the total number of possible SAR data pair combinations is 148.

b) Interferogram generation (DInSAR), filtering, and phase unwrapping. In this step, the differential interferograms are generated followed by multi-looking and the co-registration process. The reduction of noise, the phase filtering process, is conducted. Then, phase unwrapping is done to obtain unwrapped interferograms. These processes are applied for all combinations, and several interferograms are produced (in this case, 148 unwrapped interferograms). The products of these steps are interferograms, coherence images, and unwrapped interferograms.

c) Inversion of Singular Value Decomposition (SVD)-based interferograms and removal of topography artifacts. The inversion process is conducted to generate the LOS displacement time-series. However, the LOS displacement products contain the residual topographic phase (topography artifacts), $\Delta\varphi_{\mathrm{topo}}$. The residual topographic phase will be removed in this step for each interferogram.

d) Space-time filtering. This filtering process removes such atmospheric artifacts ($\Delta\varphi_{\mathrm{atm}}$). It is based on the observation that the atmospheric artifacts are highly correlated in space, but have very low correlation in time (Ferretti et al., 2000; Goldstein, 1995). This process applies a square-shaped filter with a spatial size of 1.2 km x 1.2 km, according to the spatial correlation length of atmospheric artifacts (Hanssen, 2001). This step is followed by a temporal high-pass filter operation using a window whose size is 365 days. Finally, after the atmospheric artifacts and other errors are removed, the generation of the LOS displacement time-series is conducted.

2.1.6 Projection of 3-D displacements in LOS direction

In order to evaluate the accuracy of the displacements obtained by DInSAR, the 3-D displacements provided by GPS are converted into displacements in the LOS direction. Figures 2.8 a and b show the vector projection from the 3-D displacements provided by GPS into LOS displacements for descending and ascending directions, respectively.

Based on Figure 2.8, the conversion of the 3-D GPS displacements into LOS displacements in the ascending direction can be expressed as follows (Fialko et al., 2001; He et al., 2015; Jo et al., 2017; Polcari et al., 2016):

$$D_{LOS} = [D_{N-S} \quad D_{E-W} \quad D_{U-D}] \cdot \begin{bmatrix} -\sin\beta \cdot \sin\vartheta \\ -\cos\beta \cdot \sin\vartheta \\ \cos\vartheta \end{bmatrix} \tag{2.20}$$

The conversion of the 3-D GPS displacements to LOS displacements in the descending direction can be expressed as follows (Fialko et al., 2001; He et al., 2015; Jo et al., 2017; Polcari et al., 2016):

$$D_{LOS} = [D_{N-S} \quad D_{E-W} \quad D_{U-D}] \cdot \begin{bmatrix} -\sin\vartheta \cdot \sin\beta \\ \sin\vartheta \cdot \cos\beta \\ \cos\vartheta \end{bmatrix} \tag{2.21}$$

where β is the azimuth angle of the SAR satellite orbit (flight direction). D_{N-S}, D_{E-W}, and D_{U-D} are displacement components in the directions of latitude, longitude, and height, respectively. ϑ is the incident angle (see Figure 2.2).

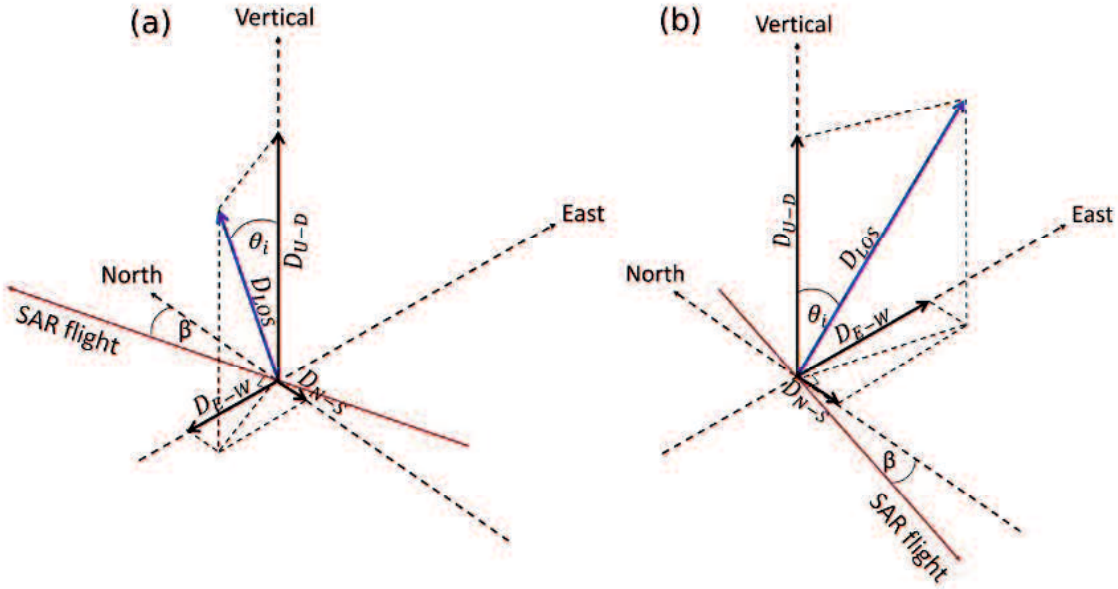

Figure 2.8. Geometrical view of 3-D displacements projected into LOS displacements: (a) for LOS in descending direction and (b) for LOS in ascending direction.

2.1.7 Derivation of subsidence from LOS displacements

The displacements obtained by DInSAR are one dimensional along the line of sight (LOS), as shown in Figures 2.8 a and b. An additional operation is required to convert the LOS displacements to subsidence. It is simply assumed in this study that the displacements are mainly caused by subsidence (vertical movements) and that the horizontal displacements are very small compared to the subsidence and can be ignored. The relationship between the LOS displacement and the subsidence is shown in Figure 2.9. ϑ_i is the local incident angle.

Following the above assumption, the vertical displacement or subsidence can then be obtained from the LOS displacement by Eq. (2.22). Subsidence D_{Sub} is assigned with a minus sign.

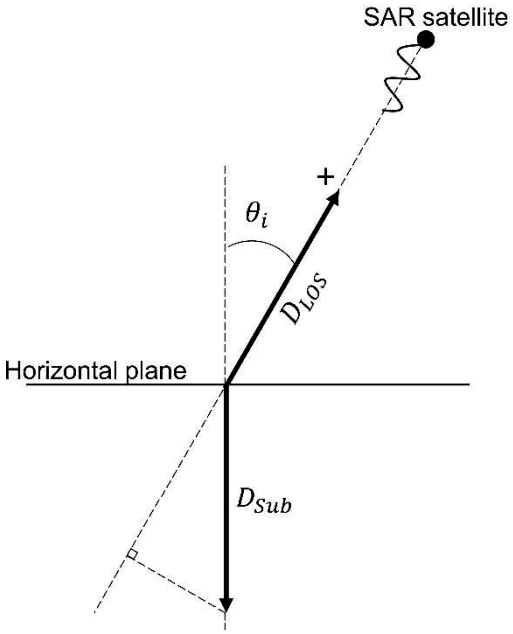

Figure 2.9. Illustration of relationship between LOS displacement and subsidence under assumption of no horizontal displacement.

$$D_{Sub} = -\frac{D_{LOS}}{cos\,\vartheta_i} \tag{2.22}$$

2.2 Literature review

The literature review focuses on several issues related to the measurement accuracy of DInSAR, the application of DInSAR for monitoring subsidence induced by underground mining activities, and the application of DInSAR for slope stability and landslide monitoring.

2.2.1 Effect of different DEMs on DInSAR results

Having an understanding of the limitations or error sources of DInSAR is very important. The main error sources of DInSAR are the satellite orbit data inaccuracy, the DEM inaccuracy, atmospheric delays, the chances of a target's scattering behavior, and other noises (Pepe and Calò, 2017). This section focuses on a review of the research work related to the effect of an external DEM on the DInSAR results (DEM inaccuracy). The accuracy of DEMs becomes very important when the target area of DInSAR experiences very large changes in elevation, for example, open-pit mines. DEMs should be updated regularly to ensure that the elevation provided by the DEMs is appropriate for representing the most recent mining elevation. If an inappropriate DEM is input into a DInSAR analysis, the phase

error due the DEM inaccuracy will become very large and cause artificial LOS displacements.

The research works that have been reviewed below mostly used term 2-pass, 3-pass, and 4-pass DInSAR. Details on those methods are given in Figure 2.10. Basically, 2-pass DInSAR is the same as the DInSAR term used in this dissertation.

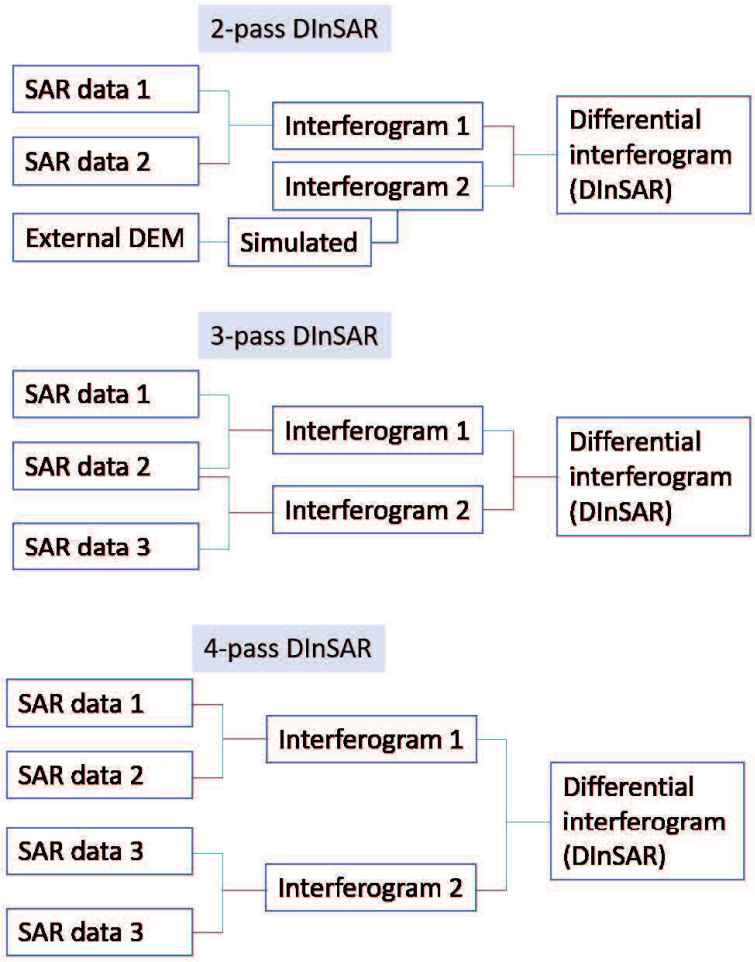

Figure 2.10. Block diagram of 2-pass, 3-pass, and 4-pass DInSAR.

Sowter and Warren (2005) investigated the effect of DEMs on the LOS displacements of DInSAR. Their research target was the Bam earthquake in Iran. They conducted 2-pass DInSAR and 3-pass DInSAR (without using a DEM). Theoretically, 3-pass DInSAR produces better accuracy of the LOS displacements because the effect of the DEMs is very small. Unfortunately, this is not realistic as the phase errors of 3-pass DInSAR are very large. 2-pass DInSAR using a DEM, referred as DInSAR, is still more appropriate for displacement monitoring than 3-pass DInSAR. Sowter and Warren (2005) mentioned that DInSAR using

a high-resolution DEM (e.g., SRTM 90-meter resolution) shows better results than DInSAR using a low-resolution DEM (low resolution and low accuracy).

Similar to Sowter and Warren (2005), Anh et al. (2015) conducted research on 2-pass DInSAR using a DEM and 3-pass DInSAR without a DEM. However, the target area of Anh et al. (2015) was subsidence in a city area. Their results show that 2-pass DInSAR using a SRTM 90-meter resolution presents better results than 3-pass DInSAR (Figure 2.11). However, they recognized that SRTM 90-meter was not accurate enough because they used Envisat SAR data in 2004, while SRTM was acquired in 2000. Within that period of 4 years, many buildings were constructed. Therefore, a great deal of artificial subsidence and uplift were recognized in the DInSAR results due the DEM inaccuracy.

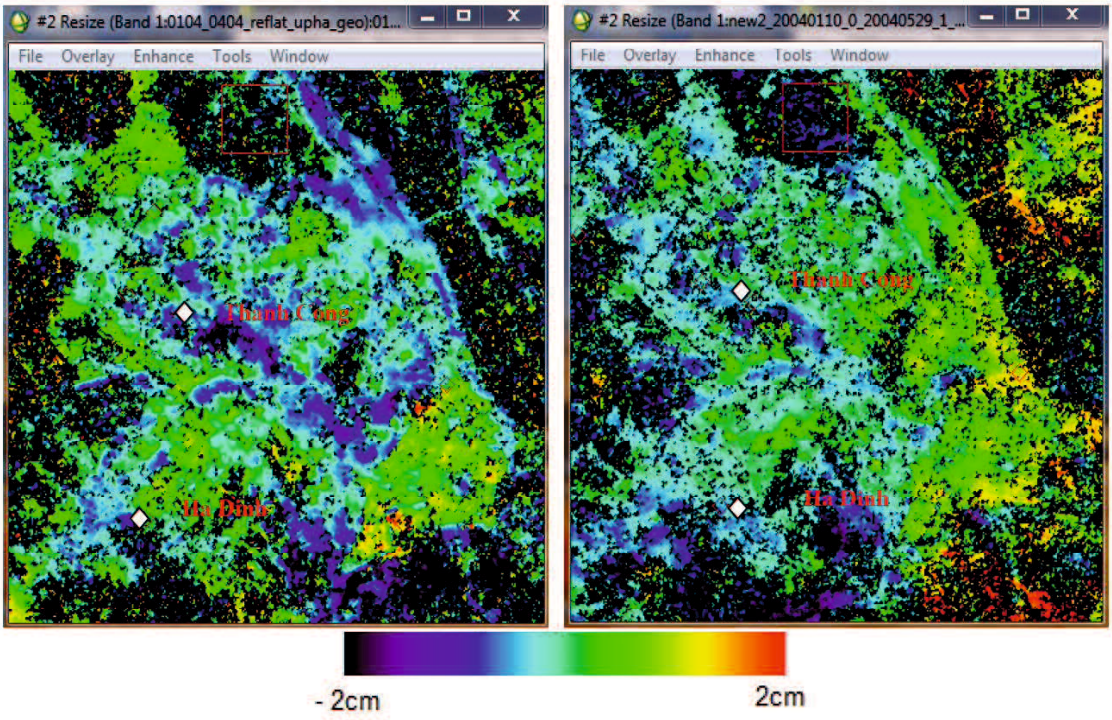

Figure 2.11. Comparison of subsidence obtained by 2-pass DInSAR (left) and 3-pass DInSAR (right) (Anh et al., 2015).

Liu et al. (2016) proposed 4-pass DInSAR to reduce such phase errors due to the DEM inaccuracy. Their target was to estimate the surface displacements of a mountain glacier. The main characteristic of glacier areas is similar to that of open-pit mines, i.e., the changes in elevation are very large over time. Based on their results, the proposed 4-pass DInSAR without an external DEM produced good accuracy in the displacement results. However, it should be noted that 1 SAR pair of images was used to generate a DEM and it was done without an external DEM during the DEM generation. They did not analyze the quality of

their DEM by InSAR. The use of an external DEM during DEM generation is very important, as has already been proven by Chunxia et al. (2005) and Nitti et al. (2011).

Gaber et al. (2017) conducted research on how to minimize errors due to DEM inaccuracies in estimating the land subsidence in Port-Said City, Egypt. They employed SBAS-DInSAR using only 9 ALOS-PALSAR images. To reduce the errors due to DEM errors, they generated a new DEM from ALOS/PRISM optical images acquired on September 9, 2014. The final resolution of ALOS/PRISM was very high, i.e., 2.5 m. They evaluated the DEM from ALOS/PRISM and SRTM using 16 GCPs from ground truth data and found that ALOS/PRISM DEM is much better than the SRTM DEM with RMS by about 2.598 m. For the SBAS-DInSAR analysis, they only used the DEM from ALOS/PRISM; the DEM by SRTM was not employed in the SBAS-DInSAR processing. Thus, it is difficult to compare how much better ALOS/PRISM DEM is than SRTM DEM for improving the final displacement by SBAS-DInSAR. There is no clear, strong evidence.

Tao et al. (2017) conducted research to investigate the effect of an external DEM on the DInSAR results in monitoring subsidence due to mining activities. They processed DInSAR using several DEMs, i.e., 1:5 million DEM (referred to as 25-m DEM), ASTER-GDEM V2, and SRTM 90-meter DEM. There are subsidence results by DInSAR for each DEM. Then, those subsidence results by each DEM are compared with the subsidence obtained by leveling. They found that using the 25-m DEM generates better subsidence results than using the other DEMs. However, they did not present the relationship between the DEM inaccuracy and the subsidence results. They only showed that a DEM with higher resolution produces better subsidence results.

From the above-mentioned circumstances, there is no comprehensive research that explains the effect of an external DEM on the LOS displacements by DInSAR in a relationship with the elevation errors provided by each DEM, the spatial resolution of each DEM itself, the relationship with the perpendicular baseline, etc.

To overcome these issues, research has been done and is presented comprehensively in Chapter 3 of this dissertation. In addition, the quality and accuracy of the DInSAR results are evaluated using precise and real-time GPS monitoring results.

2.2.2 Application of DInSAR for subsidence induced by mining activities

In the last decade, DInSAR has been widely used in several applications, such as monitoring the ground surface displacements induced by natural processes and man-made activities. In this section, a review is done that focuses on the application of DInSAR to

monitor the subsidence induced by mining activities. The main advantages of DInSAR for monitoring subsidence is that no devices need to be installed in the monitoring area. The typical DInSAR results for subsidence induced by underground mining are presented in Figure 2.12.

Chang et al. (2004) utilized DInSAR to measure the subsidence induced by underground coal mining. Then, those subsidence results were used in an Environmental Impact Assessment of the coal mining itself. The DInSAR results, i.e., measured displacements, comprise one of the important parameters for mining companies and for considering future plans. However, this research was conducted at a very early stage of SAR and the number of SAR images was very limited. Thus, the results lack temporal data and time-series displacements.

Jarosz and Zahiri (2007) conducted research using DInSAR for monitoring subsidence induced by block caving mining. They demonstrated that DInSAR is a very useful and cost-effective monitoring tool for monitoring the subsidence induced by mining. The subsidence results they obtained by DInSAR have a good correlation with the subsidence results obtained from leveling data. Similar to Chang et al. (2004), their results lacked temporal resolution because the number of images was very limited at that time. They mentioned that in the near future, DInSAR would become a promising tool and that the amount of available SAR data would increase.

Ng et al. (2015) monitored the land subsidence induced by off-shore oil and natural gas extraction. They employed a SqueeSAR time-series analysis using ALOS-PALSAR data to generate the time evolution of the subsidence. This research is very comprehensive; their subsidence results were validated using ground survey data and it was found that the discrepancy is about 4 mm/year. They presented good spatial coverage (due to using L-band data) and moderated temporal resolution (the shortest temporal baseline is 46 days). However, they used very old DEM data, i.e., SRTM DEM. Even though the SqueeSAR algorithm can reduce such DEM inaccuracies, the use of more up-to-date DEM data is recommended. This is because the ALOS-PALSAR perpendicular baselines are usually very large (a hundred meters to a few kilometers).

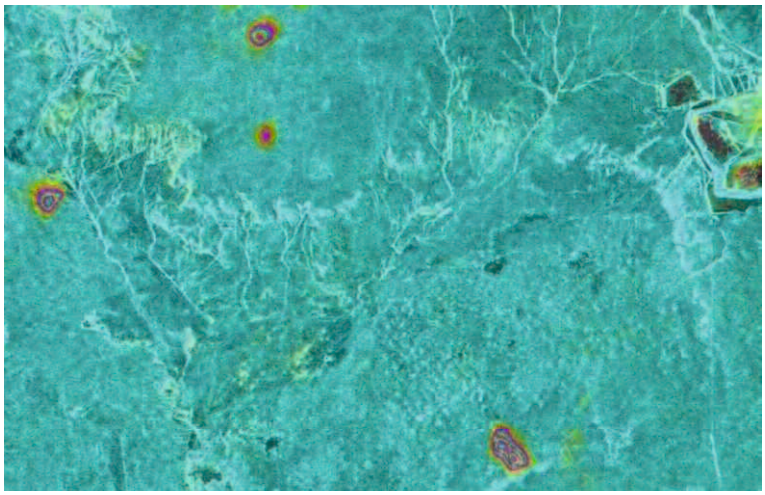

Figure 2.12. Typical DInSAR results of subsidence induced by underground mining (Zhang et al., 2018).

Du et al. (2016) conducted research to monitor the subsidence induced by coal mining using a combination of L-band (ALOS-PALSAR) and C-band (Envisat) data. They utilized a time-series InSAR (TS-InSAR) algorithm to generate the time-series subsidence. The TS-InSAR algorithm is based on the development of SqueeSAR. This research included a comparison of L-band and C-band data, and it was reported that L-band data have better spatial coverage than C-band data. This is because the L-band has a longer wavelength than the C-band. However, the L-band has lower accuracy than the C-band. Such a clear example is very important for SAR users when deciding which wavelength is appropriate for their particular target. They mentioned that the L-band is very useful for monitoring large subsidence, like that induced by mining activities, whereas the C-band is useful for monitoring small subsidence, like that in a city area. Similar to Ng et al. (2015), they employed the old SRTM DEM in their analysis. It should be noted that old DEM data tend to produce larger errors due to changes in elevation in the mining area.

Yuan et al. (2017) utilized new Sentinel-1 SAR data in DInSAR to monitor the subsidence induced by coal mining. They used very short temporal baseline data (12 days). However, they did not present the time-series subsidence; they only presented the subsidence from certain periods. Their main goal is very interesting, i.e., to employ the DInSAR technique to effectively monitor the land subsidence caused by underground mining and as an effective tool for law enforcement of over-mining activities.

From the reviews of the above research works, several issues remain, i.e., conventional DInSAR lacks temporal resolution in monitored areas, several time-series DInSAR analyses

are still using old DEM data (SRTM data), and new Sentinel-1 has a tandem mission (Sentinel-1 A and B) that should be utilized to obtain better temporal coverage.

To solve those problems and to demonstrate the ability of Sentinel-1A and -1B data, research has been done by means of a SBAS-DInSAR analysis. The research utilized a more up-to-date DEM than SRTM DEM, i.e., AW3D30-DEM. The Sentinel-1A and -1B data with a very short temporal baseline (6 days) is employed; it generated very nice time-series subsidence results.

2.2.3 Application of DInSAR for slope stability and landslides

Monitoring slope stability and landslides by DInSAR is still challenging even now. The main problems are: slope steepness, slope directions, the displacement velocity of the slope itself, vegetation coverage, etc. To know the state-of-the-art applications of DInSAR for monitoring slope stability and landslides, several recent research works are reviewed and explained in this section.

Zhu et al. (2014) proposed a method for slope displacement monitoring by combining DInSAR and GPS techniques. The TerraSAR-X data are used in this analysis. They installed several corner reflectors in a monitored slope and referred to this technique as “corner reflector InSAR” or CR-InSAR. The LOS displacements of CR-InSAR are corrected and improved using the displacements obtained by GPS. Then, the corrected LOS displacements are used for generating 3-dimensional displacements. After several corrections, they presented superior displacement accuracy obtained by CR-InSAR (about 1.1 mm). This method is very useful and highly accurate. However, it is very expensive to install corner reflectors and GPS sensors. And they are not suitable for use at unstable slopes because it is very dangerous to install and maintain such devices in unstable slopes and remote areas.

Schlögel et al. (2015) analyzed the ALOS-PALSAR data using the DInSAR method to monitor a landslide area. Their research was focused on interpreting landslides by means of a geomorphological interpretation. The concept of this research is very nice for simulating the type of landslide and interpreting the DInSAR phase changes, as seen by Figure 2.13. Their results mostly coincide with the geomorphological interpretation concept. However, this research lacks the temporal evolution of landslide displacements, because they used only a limited number of SAR images.

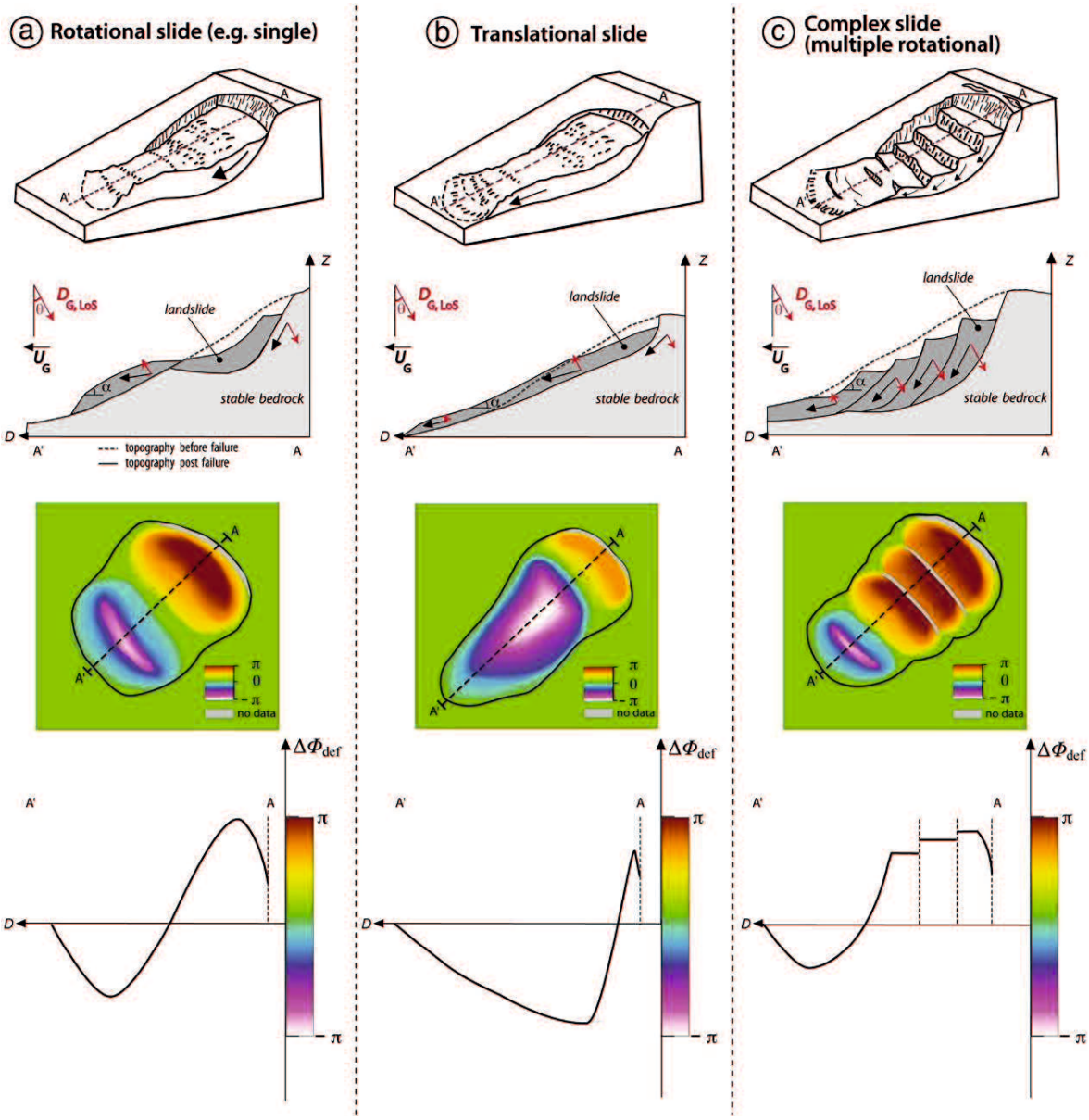

Figure 2.13. Displacement pattern, morpho-structure, and associated interferometric phase for three landslide types: (a) rotational slide with a single circular slip surface, (b) translational slide with a nearly planar slip surface parallel to the slope topography, and (c) complex slide with a series of embedded circular slip surfaces (Schlögel et al., 2015).

Liu et al. (2016a) monitored the slope displacement in a landslide area by DInSAR using TerraSAR-X data. This research developed the SBAS-DInSAR and modified several algorithms in SBAS-DInSAR to improve the displacement results. The displacements of DInSAR were compared to the displacements obtained with in situ GPS, but in different observation periods. Due to it being a highly vegetated area, the displacements could only be obtained at a few points.

Eriksen et al. (2017) monitored an unstable slope by DInSAR using TerraSAR-X data. This research utilized ascending and descending SAR data. They comprehensively visualized and interpreted the slope displacements (Figure 2.14). The target was located in an area near the North Pole which has the high possibility of snow cover. To maintain the coherence, only the SAR data taken during the summer season were used. The missing observation times during the winter were filled in by assuming that the displacement velocity would be constant during the winter season. Their results are very nice and offer a good interpretation. However, it is important to monitor the slope stability during the winter season. Ignoring the displacement during the winter is not good idea. Landslides are sometimes triggered due to snow cover and the melting of snow during this season.

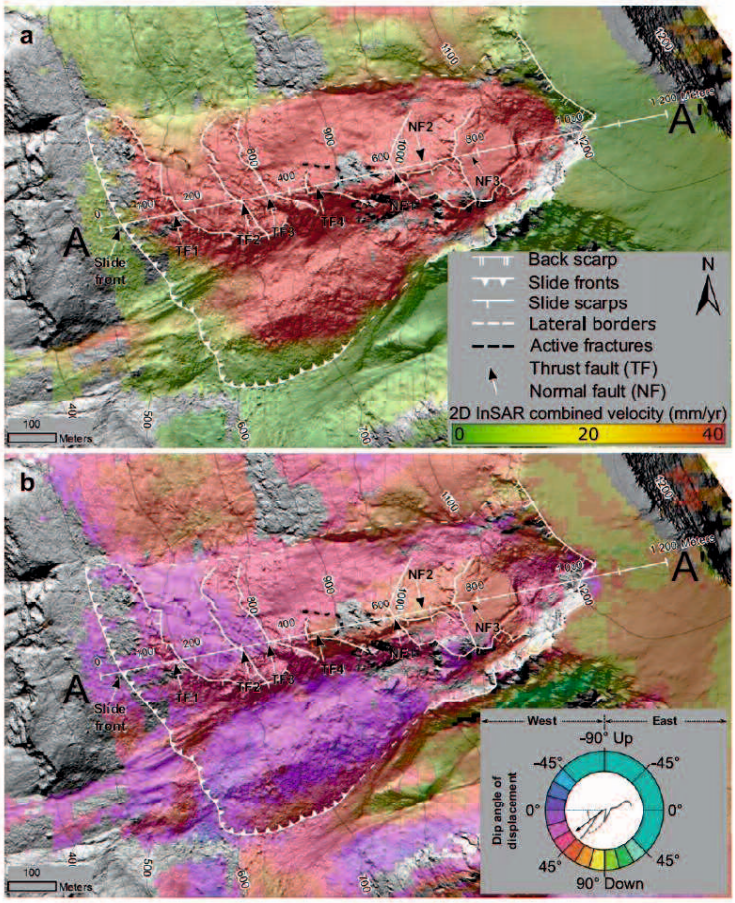

Figure 2.14. Interpretation of rockslide by 2D InSAR data and morphological elements: a) combined velocity and b) dip of displacement (Eriksen et al., 2017).

The slopes of the above-mentioned research works are mostly facing the east-west direction. This is good for DInSAR. The applicability of DInSAR to monitor slopes facing the north-south direction should be investigated. On the other hand, those research works mostly conducted the monitoring after a landslide had occurred. For some of them, the slope was monitored, but the monitoring did not include the landslide event during the observation

period. The applicability of DInSAR to monitor slope displacements that include a landslide should be investigated.

To discuss the above-mentioned problems in detail, research has been done and will be presented in Chapter 5. The main goal is to investigate and evaluate the advantages and limitations of DInSAR for monitoring slope stability and landslides.

Chapter 3. Effect of DEMs on Slope Displacement Monitoring Using DInSAR

3.1 Introduction

Displacement monitoring plays an important role in assessing the stability of slopes. There are many useful instruments for monitoring displacements, for example, extensometers, inclinometers, etc. The advantage of these instruments is that they provide displacements in real-time with high accuracy. On the other hand, these instruments measure the displacements only at certain points on the ground and can be applied only to limited areas of less than about 100 m in length. Therefore, a large number of devices would be required if the displacements over the entire area of a large slope needed to be measured. In practice, this would lead to high costs and inefficiency. Although the Global Positioning System (GPS) is one of the solutions for monitoring displacements over extensive areas (Shimizu et al., 2014), it provides the displacements only at the points where sensors have been installed. In order to monitor the displacement distribution over an extensive area, many GPS sensors would need to be installed. This would be expensive and inefficient.

Synthetic Aperture Radar (SAR) has the potential to overcome the above difficulty, namely, monitoring the distribution of displacements over an extensive area (Ferretti, 2014). Practically, Differential Interferometric SAR (DInSAR) can provide the displacement distribution of the Earth's surface in a large area without installing any devices on the ground surface. Recently, the capability of DInSAR to measure the displacements of the Earth's surface has been studied in various topics in rock and geotechnical engineering, such as land subsidence (Chaussard et al., 2014; Stramondo et al., 2008; Yastika et al., 2019), landslides (Rott and Nagler, 2006; Singhroy and Molch, 2004; Zhu et al., 2014), and other ground movements (Eriksen et al., 2017; Klein et al., 2017; Liu et al., 2011; Wang et al., 2017; Woo et al., 2012). DInSAR has also been applied to open-pit mine slope monitoring (Mura et al., 2016; Paradella et al., 2015).

In the process of DInSAR, the elevation of the ground surface is required in order to obtain the displacements. Usually a public digital elevation model (map) is used for this purpose. However, the topography of mine slopes often changes due to mining activities, and public digital elevation models do not include changes in the topography such as those of the local slopes of open-pit mines. This means that some errors are encountered when applying public digital elevation models for these specific cases. This is one of the fundamental issues in DInSAR (Massonnet and Feigl, 1998; Bürgmann et al., 2000), and

several works related to this issue have been published by Anh et al. (2015), Gaber et al. (2017), and Tao et al. (2017). However, their studies addressed the application of DInSAR for monitoring the subsidence in flat areas, where the surface topography does not change much during monitoring. Therefore, the errors in the digital elevation models are not large and their effect is small. The effects of digital elevation models should be investigated before applying DInSAR to monitor the displacements of excavated slopes. However, they have not been discussed enough in relation to open-pit mines.

This chapter focuses on investigating the influence of the errors in digital elevation models on the DInSAR results in their practical application to an open-pit mine slope. The excavation activities are seen to affect the changes in the topography of the mining area. Six different digital elevation models are used to clarify the effect of errors on the elevation, and an appropriate digital elevation model is recommended. In order to verify the model, the DInSAR results are compared with the results of precise GPS displacement monitoring conducted for a period of three years at the same limestone quarry.

3.2 Study area, data sources, and methodology

3.2.1 Study area

A limestone quarry located in a northern prefecture of Japan was selected as the experimental site for this research, since continuous displacement monitoring by GPS has been conducted there for many years (Nakashima et al., 2014, 2012) and the results of DInSAR can be compared with those of GPS. Figure 3.1 presents an outline and photographs of the site (Nakashima et al., 2014, 2012).

Figures 3.2 a and b show aerial photographs of the quarry taken on September 26, 2002 (GSI, 2002) and on April 5, 2011 (Google Earth, 2011), respectively. As seen in Figure 3.2 b, the main quarry was excavated to the present bottom (-135 m from sea level) before 2006, and the mining area was expanded to the west and northwest areas of the quarry after 2006. In Figure 3.2 a, the south part of the inside of the quarry and the west and the northwest areas of the quarry were not excavated. The shape of the mining area has changed.

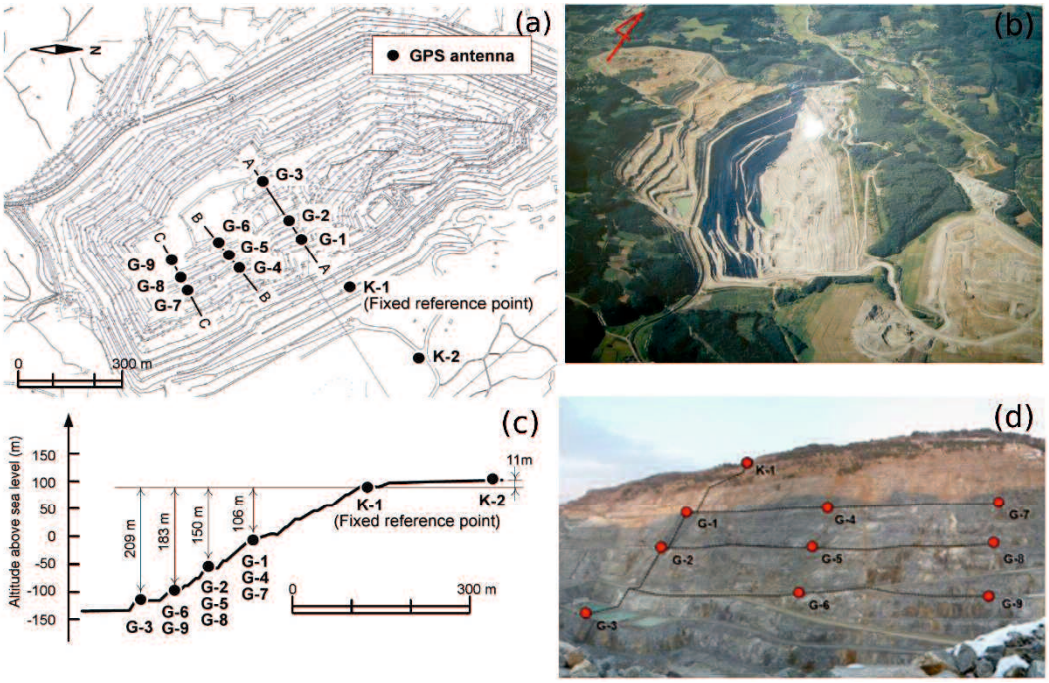

Figure 3.1. Experimental site: (a) plan view, (b) aerial view, (c) vertical cross section, and (d) view of slope monitored by GPS (Nakashima et al., 2014).

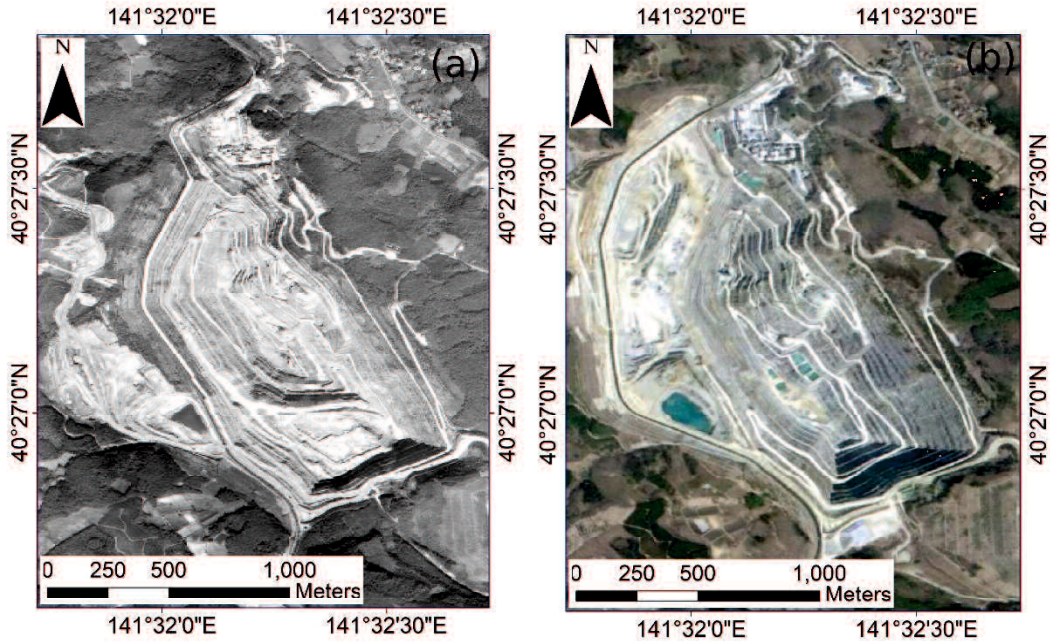

Figure 3.2. Changes in topography at experimental site: (a) photo taken on September 26, 2002 (GSI, 2002) and (b) photo taken on April 5, 2011 (Google Earth, 2011).

3.2.2 Data sources

3.2.2.1 SAR dataset

This research uses the SAR data observed by the ALOS-PALSAR satellite (Advanced Land Observing Satellite using the Phased Array type L-band Synthetic Aperture Radar) in operation from 2006 to 2011 by JAXA (Japan Aerospace Exploration Agency). The ALOS-PALSAR satellite employs the L-band microwave with a frequency of 1270 MHz and a wavelength λ of 23.62 cm (JAXA-EORC, 2008). Table 3.1 presents all the SAR data which were observed for the study area during the operation of ALOS-PALSAR. The data are used in this study.

Table 3.1. List of SAR data.

No.	Acquisition date	Track number	Frame number	Orbit direction
1	July 20, 2007	401	800	Ascending
2	September 4, 2007	401	800	Ascending
3	October 20, 2007	401	800	Ascending
4	December 5, 2007	401	800	Ascending
5	April 21, 2008	401	800	Ascending
6	June 6, 2008	401	800	Ascending
7	January 22, 2009	401	800	Ascending
8	March 9, 2009	401	800	Ascending
9	July 25, 2009	401	800	Ascending
10	September 9, 2009	401	800	Ascending
11	April 27, 2010	401	800	Ascending
12	June 12, 2010	401	800	Ascending
13	July 28, 2010	401	800	Ascending
14	September 12, 2010	401	800	Ascending
15	October 28, 2010	401	800	Ascending

3.2.2.2 Digital elevation model data

3.2.2.2.1 Public digital elevation models

There are several public digital elevation models which can be used in DInSAR processing. This study uses five of them: “SRTM-3 V2” and “SRTM-1 V3” by SRTM (Shuttle Radar Topography Mission), “GSI-DEM” by GSI (Geospatial Information Authority of Japan), “AW3D30-DEM” by ALOS-PRISM (Panchromatic Remote-sensing Instrument for Stereo Mapping), and “ASTER-GDEM V2” by ASTER (Terra satellite using the Advanced Spaceborne Thermal Emission and Reflection Radiometer). The data acquisition date and the ground resolution are different for each digital elevation model (see Table 3.2).

The levels of accuracy for the elevation in the five digital elevation models are as follows: 5.6 – 9.0 m for SRTM-3 V2 and SRTM-1 V3 (Rodriguez et al., 2006), 5 m for GSI-DEM (GSI, 2016), 5 m for AW3D30-DEM (Tadono et al., 2014; Takaku et al., 2014), and 6.1 m in flat areas and 15.1 m in mountainous areas for ASTER-GDEM V2 (Tachikawa et al., 2011).

Table 3.2. List of public digital elevation models for DInSAR processing.

No.	Name of digital elevation model	Sensor name	Space/Airborne/Satellite name	Ground resolution (meters)	Data acquisition date	Publish date
1	SRTM-3 V2	Spaceborne Imaging Radar-C/X-band (SIR-C/X-SAR)	The Shuttle Radar Topography Mission	90x90	February 11, 2000	April 17, 2013
2	SRTM-1 V3	Spaceborne Imaging Radar-C/X-band (SIR-C/X-SAR)	The Shuttle Radar Topography Mission	30x30	February 11, 2000	September 23, 2014
3	GSI-DEM	Optical Sensor (Photogrammetry)	Airborne	10x10	2002	October 1, 2016
4	AW3D30-DEM	The Panchromatic Remote-sensing Instrument for Stereo Mapping (PRISM)	ALOS Satellite	30x30	2006-2011	May 31, 2016
5	ASTER GDEM V2	The Advanced Spaceborne Thermal Emission and Reflection Radiometer	Terra satellite	30x30	October 17, 2011	November 16, 2011

3.2.2.2.2 Digital elevation models by InSAR

The InSAR procedure can provide digital elevation models (Figure 2.5 a). This study employs InSAR to generate updated digital elevation models using pairs of SAR data, as shown in Table 3.3. Three digital elevation models are generated; they are called InSAR-DEM 2007, InSAR-DEM 2009, and InSAR-DEM 2010.

Table 3.3. SAR data pairs for generating digital elevation models by InSAR.

DEM product	SAR data pair		Perpendicular baseline (meters)	Temporal baseline (days)
	Master	Slave		
InSAR-DEM 2007	July 20, 2007	September 4, 2007	161.880	46
InSAR-DEM 2009	July 25, 2009	September 9, 2009	511.037	46
InSAR-DEM 2010	June 12, 2010	July 28, 2010	363.292	46

Envi version 5.4 and SARscape version 5.4 (SARMAP, 2016) were used to conduct the InSAR analysis; details on the parameters are presented in Table 3.4.

Table 3.4. InSAR main steps and parameter setting for DEM generation.

Processing step	Parameter name	Parameter value/setting
(1) Interferogram generation	Range looks	1 look
	Azimuth looks	8 looks
	Co-registration with DEM	True
	External DEM	1. SRTM-3 V1 2. SRTM-1 V3 (in sequential processing)
(2) Adaptive filter and coherence generation	Coherence generation	True
	Adaptive filter	True
	Filtering method	Goldstein
(3) Phase unwrapping	Unwrapping method	Minimum cost flow
	Coherence threshold	0.2
(4) Refinement and re-flattening	Refinement method	Polynomial refinement
	Polynomial degree	3
	Refinement GCP file	Geographic GCPs (Manually generated)
(5) Phase to height conversion and geocoding	Product coherence threshold	0.2
	Geoid type	EGM96
	Elevation type	Ellipsoidal
	Pixel size (resolution)	25 x 25 m

3.2.2.3 Comparison of public and InSAR digital elevation models

Figure 3.3 shows the five public digital elevation models (Table 3.2) corresponding to the study area. SRTM-3 V2, SRTM-1 V3, and GSI-DEM (Figures 3.3 a, b, and c, respectively) were created using data observed around 2000-2002. Comparing them with the photograph taken in 2002, shown in Figure 3.2 a, the three models seem to represent the actual topography in 2002, while SRTM-3 V2 is very low resolution. On the other hand, when they are compared with the photograph taken in 2011, shown in Figure 3.2 b, it is found that the models could not accurately represent the expanded (excavated) areas to the west near the surface, to the northwest or to the south of the inside of the quarry. The digital elevation models contain large errors for the areas excavated from 2006-2011.

AW3D30-DEM (Figure 3.3 d) was developed using the data observed from 2006-2011 and seems to coincide well with the photograph taken in 2011. The ASTER-GDEM V2 (Figure 3.3 e) is not adequate for the topography of the inside of the quarry in 2011, even though this model was developed in 2011.

Figure 3.4 shows the digital elevation models produced by the InSAR procedure in 2007, 2009, and 2010. Comparing Figure 3.4 c with the photograph in Figure 3.2 b, InSAR-DEM 2010 seems to represent the actual topography.

Therefore, some public digital elevation models may not be adequate for representing the present topography of a study area, because they were created on a certain date (during a certain period). The InSAR procedure can update the elevation model of an area.

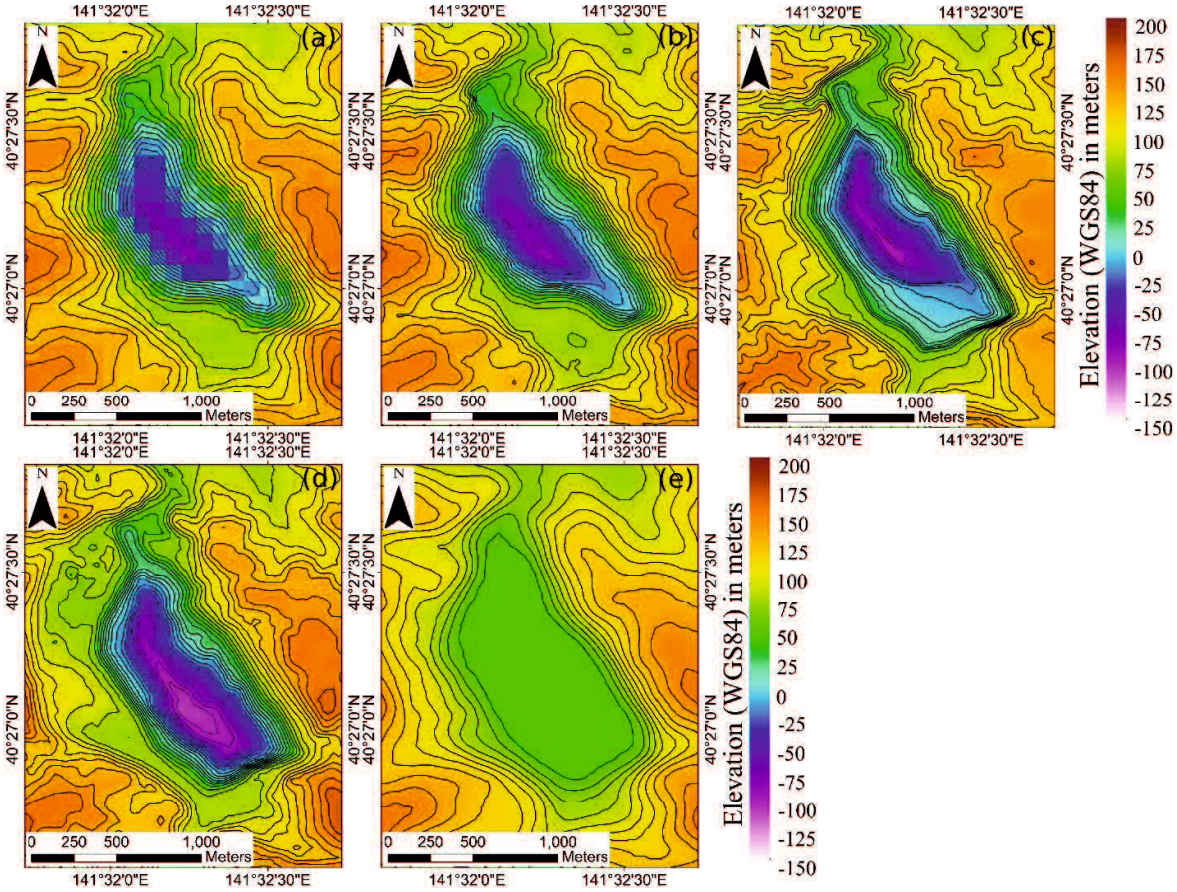

Figure 3.3. Digital elevation models generated by other sources: (a) SRTM-3 V2, (b) SRTM-1 V3, (c) GSI-DEM, (d) AW3D30-DEM, and (e) ASTER GDEM V2. The vertical interval of the contour lines is 10 m.

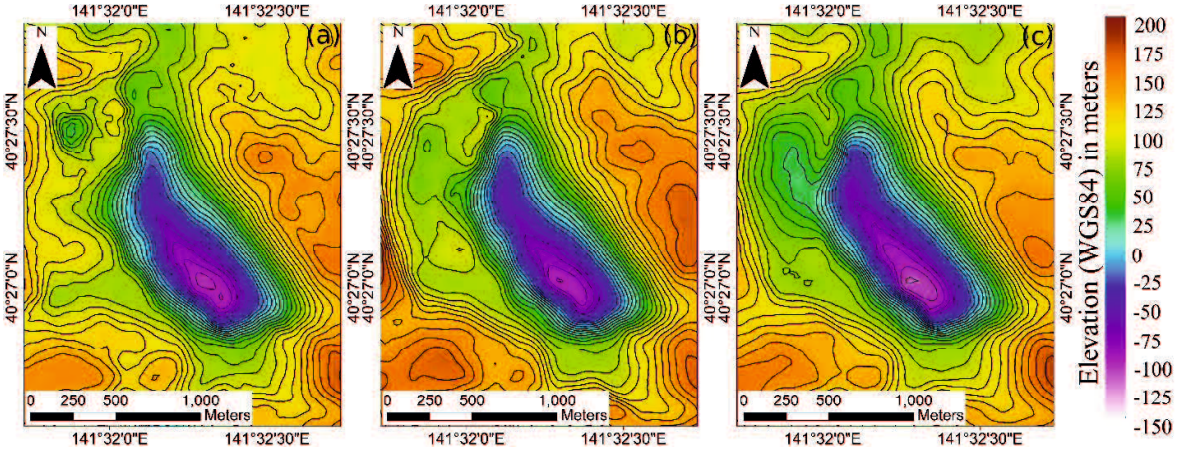

Figure 3.4. Digital elevation models generated by InSAR: (a) InSAR-DEM 2007, (b) InSAR-DEM 2009, and (c) InSAR-DEM 2010. The vertical interval of the contour lines is 10 m.

3.2.2.4 GPS data

Continuous displacement monitoring has been conducted with GPS at this site since November 18, 2006 (Nakashima et al., 2014). After conducting two steps of error corrections,

the accuracy (standard deviation) is within a few mm. The first step was to correct the tropospheric delays by the Modified Hopfield model (Hofmann-Wellenhof et al., 2001) and the second step was to estimate the real displacement by applying the Trend Model method (Shimizu, 1999, 2014). The GPS accuracy was confirmed by an experiment in which the actual given displacement and the GPS measured displacement were compared (Nakashima et al., 2014). The monitoring results of GPS are used for assessing the accuracy of the DInSAR results.

3.2.3 Methodology

The DInSAR procedure is employed to estimate the surface displacements (Figure 2.5 b) using the SAR data pairs shown in Table 3.5. In order to investigate the effect of the digital elevation models on the DInSAR results, the DInSAR procedure is applied using all the public digital elevation models (Table 3.2) and three digital elevation models by InSAR (Table 3.3) in separate processes. Then, several LOS displacements are produced from the same SAR data pairs, but with different digital elevation models.

Table 3.5. List of SAR data for DInSAR processing.

Period	SAR data pair		Perpendicular baseline (meters)	Temporal baseline (days)
	Master	Slave		
1	July 20, 2007	September 4, 2007	161.880	46
2	September 4, 2007	October 20, 2007	270.948	46
3	October 20, 2007	December 5, 2007	131.961	46
4	April 21, 2008	June 6, 2008	-34.481	46
5	January 22, 2009	March 9, 2009	433.270	46
6	July 25, 2009	September 9, 2009	511.037	46
7	April 27, 2010	June 12, 2010	-3.418	46
8	June 12, 2010	July 28, 2010	363.292	46
9	July 28, 2010	September 12, 2010	116.502	46
10	September 12, 2010	October 28, 2010	413.760	46

Envi version 5.4 and SARscape version 5.4 (SARMAP, 2016) were used to conduct the DInSAR analysis. The Goldstein Filter (Goldstein and Werner, 1998) was used in the process to filter the interferograms, and the Minimum Cost Flow (MCF) algorithm (Costantini, 1998) was applied to conduct the phase unwrapping. The detailed parameters for the DInSAR processing are presented in Table 3.6.

Table 3.6. DInSAR main steps and parameter setting for displacement measurements.

Processing step	Parameter name	Parameter value/setting
(1) Interferogram generation	Range looks	1 look
	Azimuth looks	8 looks
	Co-registration with DEM	True
	External DEM	1. SRTM-3 V1 2. SRTM-1 V3 3. GSI-DEM 4. AW3D30-DEM 5. InSAR-DEM 6. ASTER-GDEM (in sequential processing)
(2) Adaptive filter and coherence generation	Coherence generation	True
	Adaptive filter	True
	Filtering method	Goldstein
(3) Phase unwrapping	Unwrapping method	Minimum cost flow
	Coherence threshold	0.2
(4) Refinement and re-flattening	Refinement method	Polynomial refinement
	Polynomial degree	3
	Refinement GCP file	Geographic GCPs (Manually generated)
(5) Phase to displacement conversion and geocoding	Product coherence threshold	0.2
	Pixel size (resolution)	25 x 25 m

3.3 Results and discussion

3.3.1 Results of DInSAR using different digital elevation models

The LOS displacement distributions obtained by DInSAR are shown in Figure 3.5. The contour lines in this figure represent the elevations of the digital elevation models. Figures 3.5 a, b, and c show the LOS displacement results obtained by DInSAR using the public digital elevation models and InSAR-DEM 2007, InSAR-DEM 2009, and InSAR-DEM 2010, respectively. The LOS displacements are represented by a color scale from -50 mm to 50 mm. The red color indicates the areas moving far away from the satellite, the green color

indicates the areas with almost no or only small displacements, and the blue color indicates the areas moving toward the satellite.

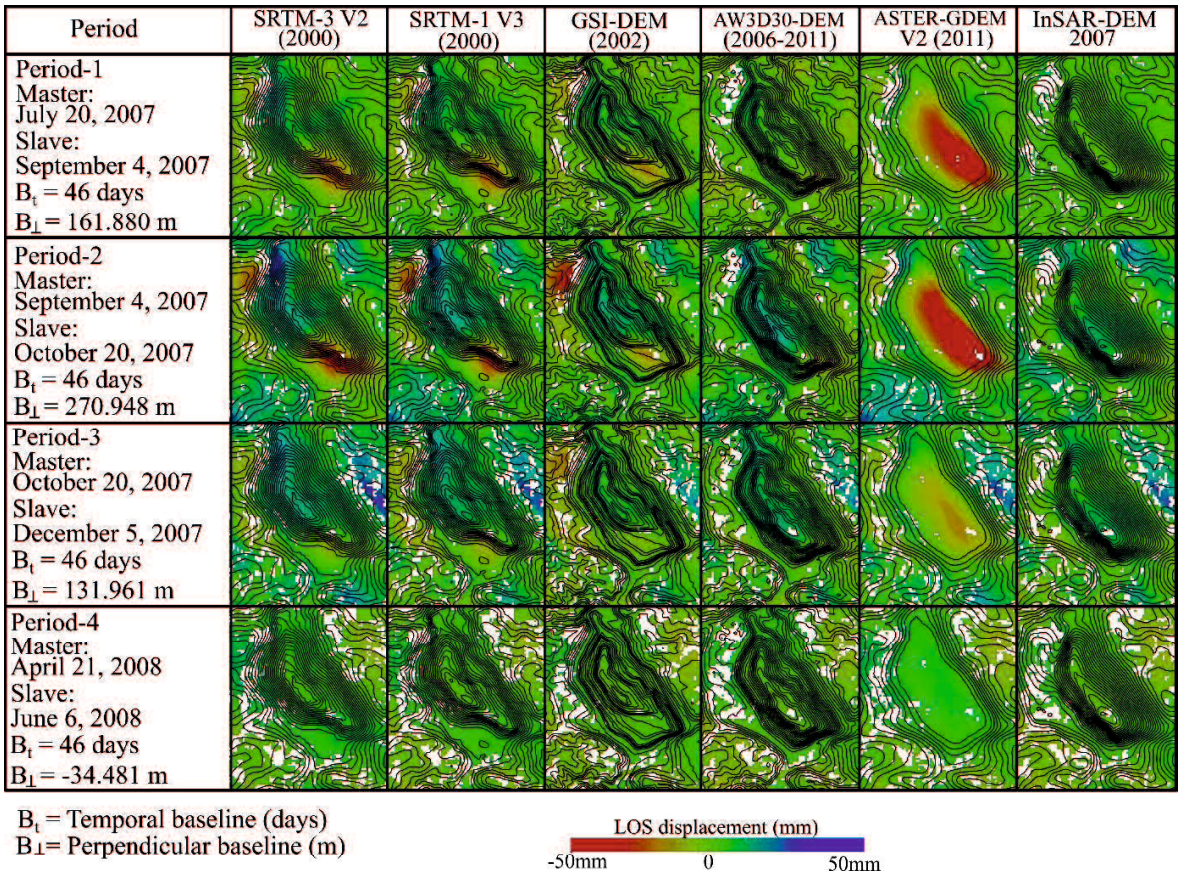

(a)

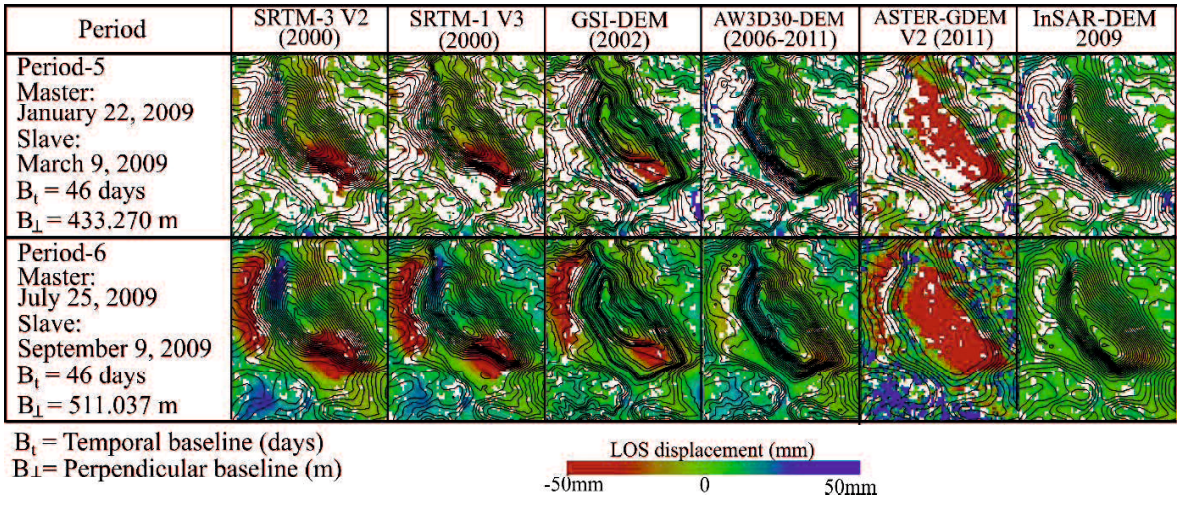

(b)

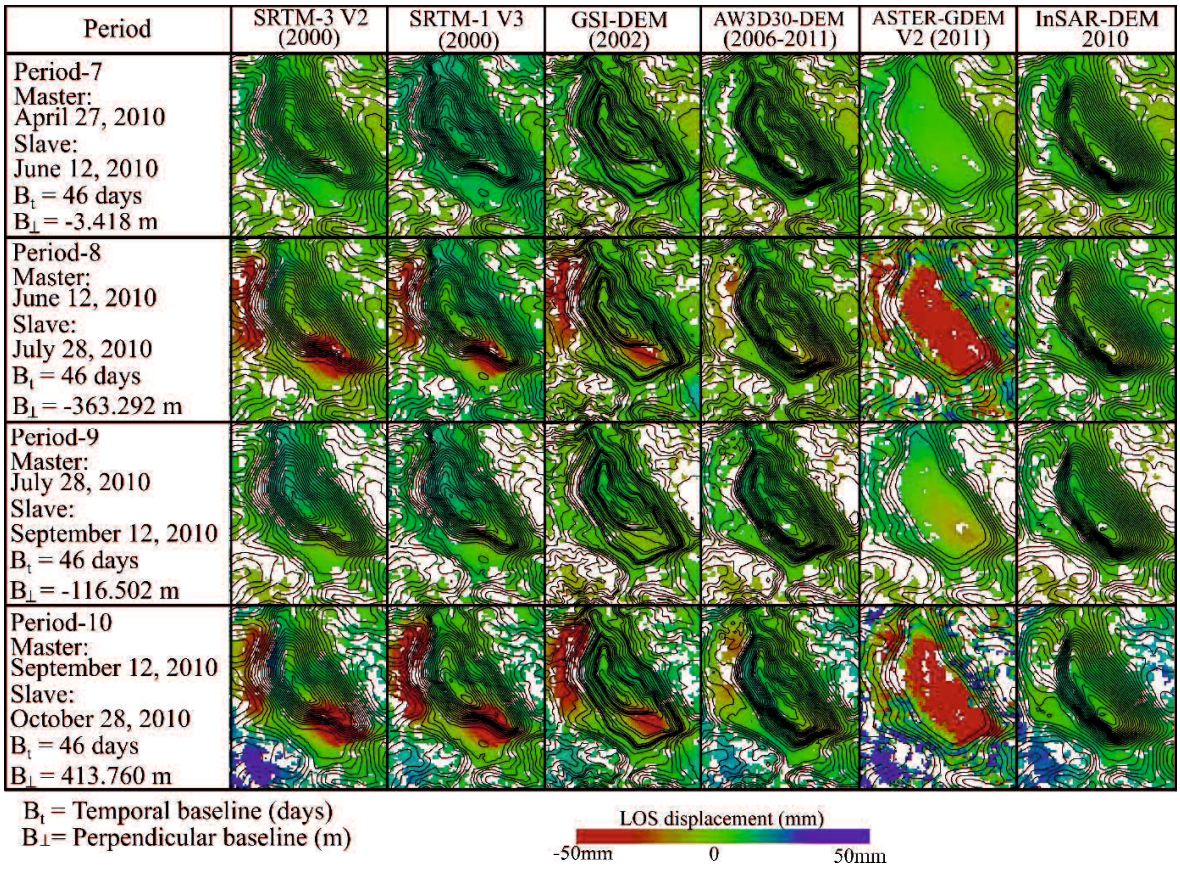

(c)

Figure 3.5. Comparison of LOS displacement results obtained by DInSAR using public and InSAR digital elevation models: (a) public digital elevation models and InSAR-DEM 2007, (b) public digital elevation models and InSAR-DEM 2009, and (c) public digital elevation models and InSAR-DEM 2010.

The excavations of the main quarry were completed before 2006, as previously mentioned, and it has been confirmed that there have been no remarkable displacements at the slopes of the quarry since that time (Hirabayashi et al., 2009; Nakashima et al., 2014). Therefore, the displacement distribution should be green over the whole area, except for the newly expanded area. Any areas with non-green colors indicate different displacement results caused by the use of different digital elevation models.

Figure 3.5 shows that the red color, representing large displacements, is found in the results acquired with the public digital elevation models, except for AW3D30-DEM, especially in Periods-1, -2, -5, -6, -8, and -10. They can be taken as errors in the LOS displacements brought about by the inaccuracy of the digital elevation models. In the case of using ASTER-GDEM V2, a large error is found in the center of the quarry because the topography of the whole quarry is incorrect (see Figure 3.3 e). In the cases of using SRTM-3 V2, SRTM-1 V3, and GSI-DEM, errors are found in the south and west areas of the quarry because the topography in those areas is not correct.

On the other hand, the results acquired with AW3D30-DEM and InSAR-DEMs are mainly green (displacements are within ±10 mm), although there are no results (white area) for some of the northwest area during this period. This is because the excavation area was expanded to the northwest part of the quarry during the DInSAR measurement period, i.e., 2007-2010; and thus, the ground surface conditions changed and no results could be obtained.

In order to discuss the effect of the digital elevation models in detail, the LOS displacement and the perpendicular baseline length for each case using different digital elevation models are presented in Figure 3.6. Four points, namely, G1, G2, G3, and *P*, shown in Figure 3.6 e, are selected as examples for comparison. G1, G2, and G3 are the GPS monitoring points, as shown in Figure 3.1, and point *P* is located at the bottom of the quarry. The LOS displacements are extracted from the DInSAR results during each period (Period-1 to Period-10), and they are plotted as the absolute values. Each error in the public digital elevation mode, $\Delta z'$, is defined by taking the differences in elevation between the public digital elevation models and InSAR-DEM 2010.

Almost all the absolute LOS displacements are within 10 mm at G1 (see Figure 3.6 a), because the value of $\Delta z'$ is small (less than 30 m) for all the digital elevation models. At G2 and G3, the LOS displacement in the case of using ASTER-GDEM V2 increases as the perpendicular baseline length increases, while the LOS displacement in the case of using the other digital elevation models is within about 10 mm. This is because the $\Delta z'$ of ASTER-GDEM V2 is large at both G2 ($\Delta z'$= 63.26 m) and G3 ($\Delta z'$= 125.88 m), as seen in Figures 3.6 b and c, respectively.

At point *P*, since $\Delta z'$ is large in the cases of using ASTER-GDEM V2 ($\Delta z'$ = 154.06 m), SRTM-1 V3 ($\Delta z'$= 59.63 m), SRTM-3 V1 ($\Delta z'$ = 77.06 m), and GSI-DEM ($\Delta z'$= 89.54 m), the absolute LOS displacements increase as the perpendicular baseline length increases. AW3D30-DEM ($\Delta z'$= 5.54 m) and InSAR-DEMs are accurate; and thus, the absolute LOS displacements are within about 10-20 mm.

Finally, it is found that if elevation error $\Delta z'$is large, the error in the LOS displacements increases. In some cases, the error becomes more than 100 mm. Such a tendency increases when the perpendicular baseline length is long. It is a natural relationship from Eq. (2.5). As long as the updated digital elevation model is used, the errors in the displacements will remain within 10-20 mm at this quarry.

The InSAR procedure is one of the effective solutions for updating the digital elevation models at this site. It is very important to check and update the digital elevation models before applying DInSAR to open-pit mine slope monitoring.

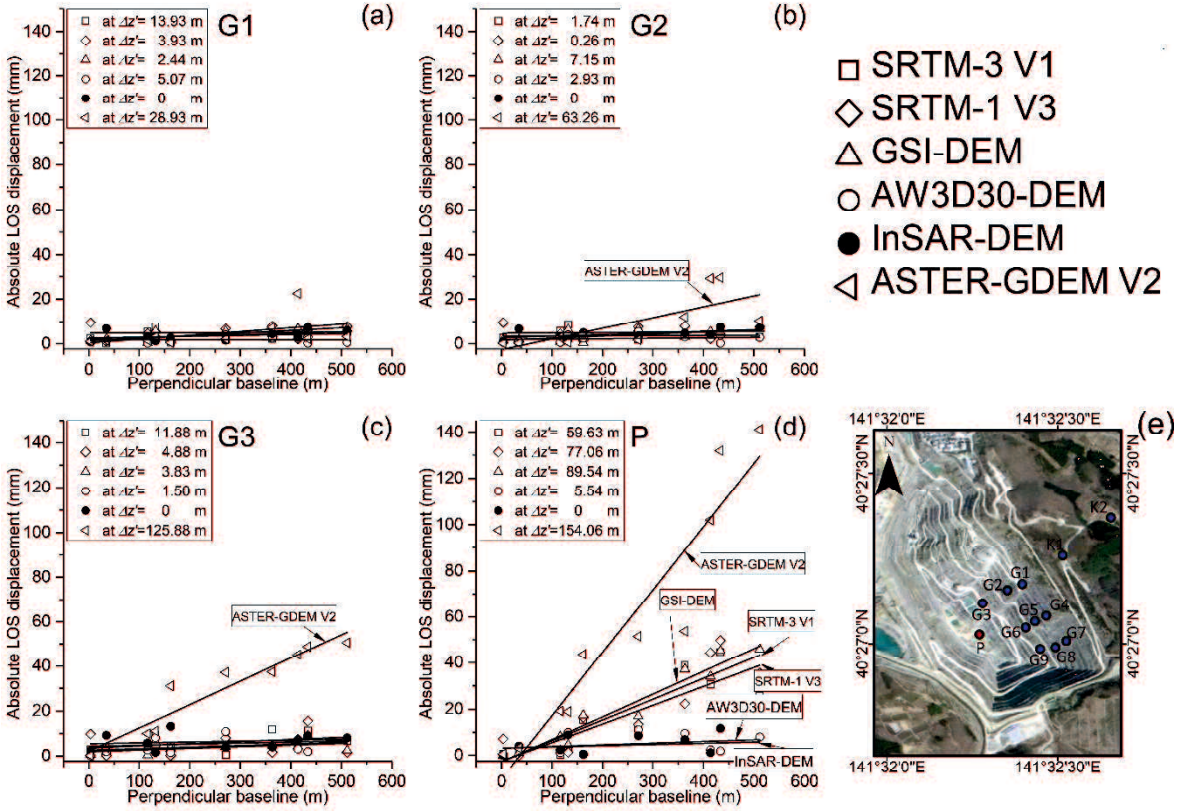

Figure 3.6. Relationship of absolute LOS displacement and perpendicular baseline ($b_{\perp}$) from public and InSAR digital elevation models: (a) at G1, (b) at G2, (c) at G3, (d) at point P, and (e) location of point P. $\Delta z'$ is calculated by subtracting InSAR-DEM 2010 from the public digital elevation models.

3.3.2 Validity of measured displacements by DInSAR using appropriate digital elevation model

In order to investigate the accuracy of the displacements measured by DInSAR, the LOS displacements are compared with the displacements measured by GPS in this section. The results acquired by DInSAR using InSAR-DEMs are used as the LOS displacements. Continuous displacement monitoring has been conducted with GPS at this site since November 18, 2006. The accuracy (standard deviation) of this GPS monitoring system is within a few mm (Nakashima et al., 2014).

To make an appropriate comparison between GPS and DInSAR, the three-dimensional displacement components in the directions of latitude, longitude, and height, obtained by

GPS, should be transformed to the direction of the LOS displacements, as explained in section **2.1.6.**

Figures 3.7 a–d show the three-dimensional displacements at G1 continuously measured by GPS for four years (Nakashima et al., 2014), and the calculated LOS displacements are given in Figure 3.7 d. The GPS monitoring system has been measuring the displacements every hour since November 18, 2006. The monitoring results at the other points are similar to those at G1. Therefore, it is found that there were no remarkable displacements during this period.

In this research, the GPS data from November 18, 2006 to October 28, 2010 are used. In order to compare the displacements obtained by DInSAR and GPS, the displacements measured hourly by GPS were averaged into daily data. Since DInSAR obtains the incremental displacements for each period based on the master and slave data (see Table 3.5), the incremental displacements for the same period were calculated from the results of the GPS monitoring (see Figure 3.7 e).

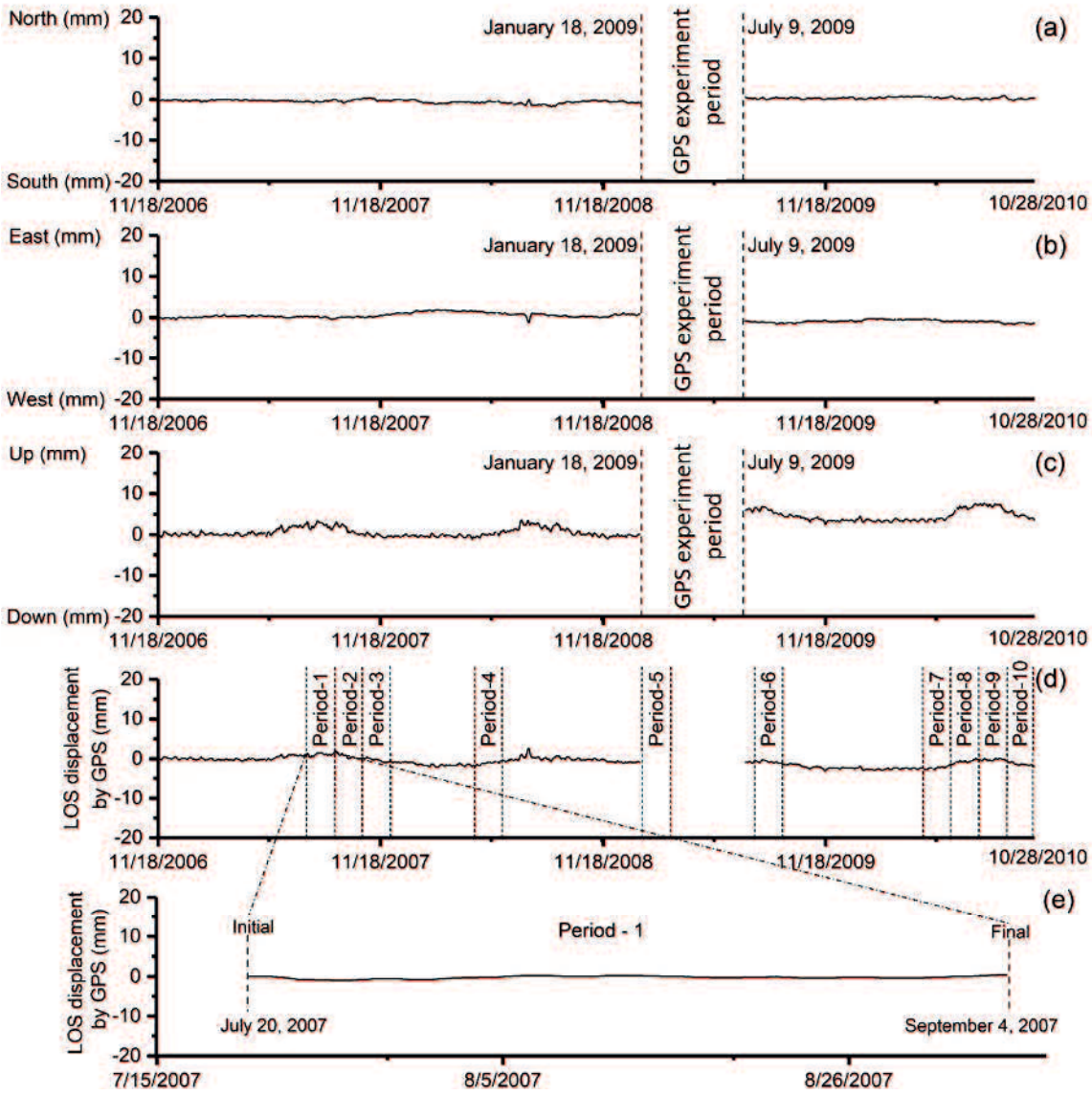

Figure 3.7. Measured displacements at G-1 by GPS and in the direction of LOS: (a) displacement in the direction of latitude, (b) displacement in the direction of longitude, (c) displacement in the direction of height, (d) displacement in the LOS direction, and (e) extracted incremental LOS displacement of GPS in the period of the DInSAR measurement.

Figures 3.8 a–i show comparisons of the LOS displacements obtained by DInSAR and GPS for all the GPS points, G1-G9, respectively. The discrepancy in the displacements by DInSAR and GPS is less than 10 mm, except at certain points and during certain periods. The root mean square errors (RMSEs) in the measurement results for DInSAR and GPS are given in Tables 3.7 and 3.8. Table 3.7 shows the RMSE at each measurement point, while Table 3.8 shows the RSME for each period.

The RMSEs in the LOS displacements by DInSAR and GPS for each point are 3.9-8.8 mm and 1.0-2.2 mm, respectively (Table 3.7). The RMSE in the discrepancy between

DInSAR and GPS is 4.1-8.6 mm. If the measurement accuracy is expressed by the RMSE, it is seen that DInSAR can measure displacements with cm-level accuracy at the slope of this quarry.

Figure 3.9 presents the correlation between the LOS displacements by DInSAR and GPS. It shows that the results of GPS are within ± 3mm, while the DInSAR results are mostly within ± 10 mm.

Table 3.7. RMSEs of DInSAR and GPS for each point.

Point	Elevation(m)	RMSE of DInSAR (mm)	RMSE of GPS (mm)	RMSE DInSAR-GPS (mm)
G1	-11	4.5	1.1	4.7
G2	-58	4.9	1.8	5.3
G3	-115	6.3	2.2	7.2
G4	-11	3.9	1.0	4.1
G5	-56	4.0	1.5	4.4
G6	-89	6.4	1.9	6.5
G7	-11	5.1	1.2	4.7
G8	-54	7.3	1.2	7.0
G9	-89	8.8	1.2	8.6

Table 3.8. RMSEs of DInSAR and GPS for each period.

Period	Perpendicular baseline (m)	RMSE of DInSAR (mm)	RMSE of GPS (mm)	RMSE DInSAR-GPS (mm)
Period-1	161.880	2.5	0.5	2.7
Period-2	270.948	5.9	2.1	7.9
Period-3	131.961	3.1	1.0	4.0
Period-4	-34.481	2.3	1.9	0.8
Period-5	433.270	8.2	NA (maintenance)	NA (maintenance)
Period-6	511.037	9.0	1.5	8.1
Period-7	-3.418	3.6	1.5	2.3
Period-8	363.292	6.4	1.8	7.8
Period-9	116.502	6.6	0.8	7.6
Period-10	413.760	8.9	1.7	7.4

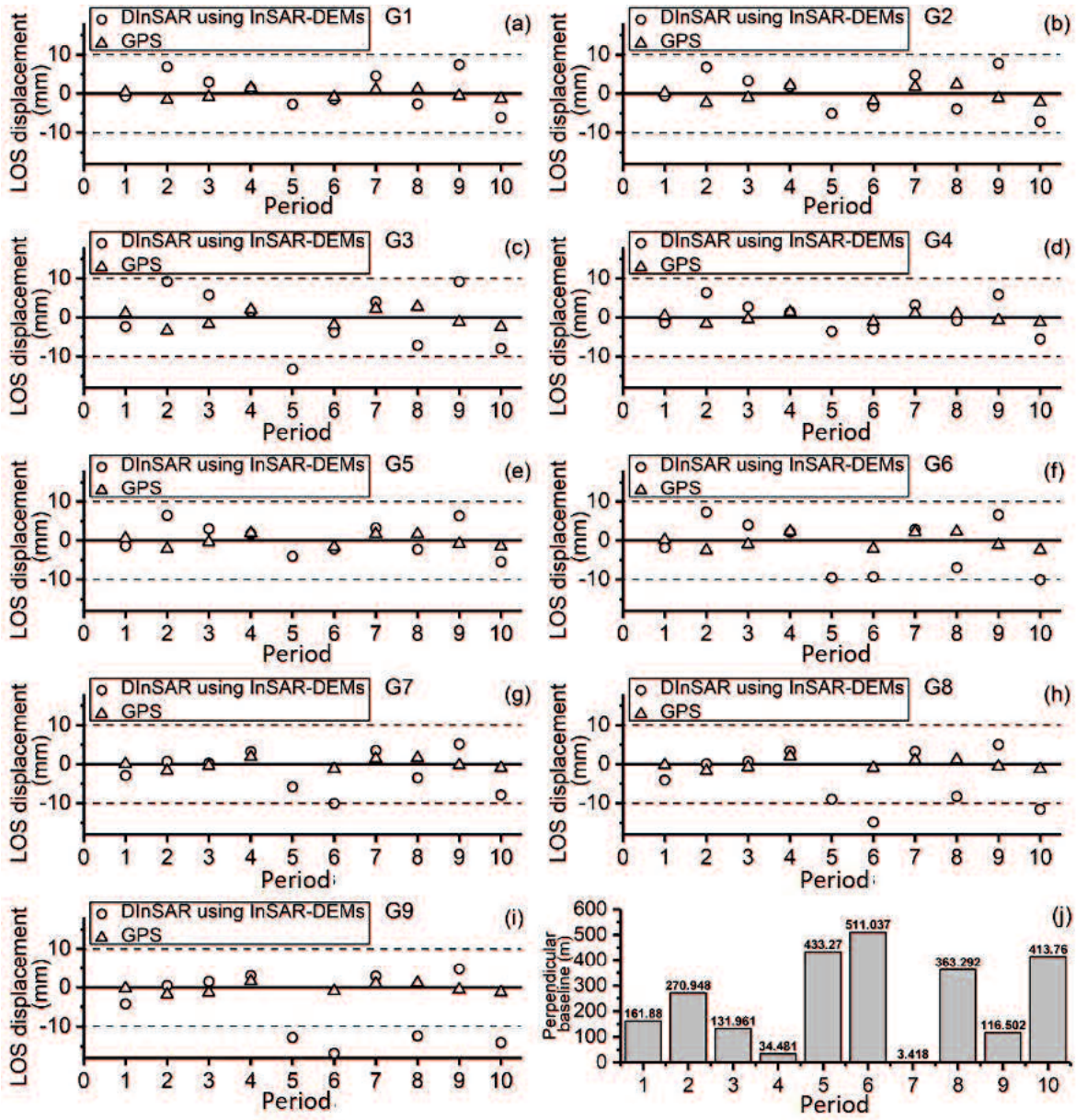

Figure 3.8. Comparison of LOS displacements by DInSAR and GPS: (a) – (i) comparison at G1-G9 and (j) absolute perpendicular baseline length for each period.

Figure 3.10 a shows the relationship between the RMSEs in the DInSAR results and the elevation of the measurement points. It is found that the RMSE increases as the elevation becomes deeper. G3, G6, and G9 are located at deeper elevations than the other points (see Figure 3.1). G8 and G9 are located near the corner of the quarry. The displacements at those points seem to have been influenced not only by the depth, but also by being in the corner. The results at G7 are totally good, because the RMSE is about 5 mm and only the results of Period-6 are scattered. This scatter seems to have been caused by the length of the perpendicular baseline. This issue will be discussed next.

Figure 3.10 b shows the relationship between the RMSEs in the DInSAR results and the length of the perpendicular baseline. As seen in section **2.1.2**, a long perpendicular baseline has a large influence on the results in terms of errors in the digital elevation models. From Figure 3.10 b, the large discrepancies mostly appear during the periods of a long perpendicular baseline length. The RMSEs in Periods-2, -5, -6, -8, -9, and -10 are larger than the others. The perpendicular baseline lengths for those periods are larger than 200 m, except for Period-9. This means that the perpendicular baseline length is also an important parameter for obtaining better results by DInSAR.

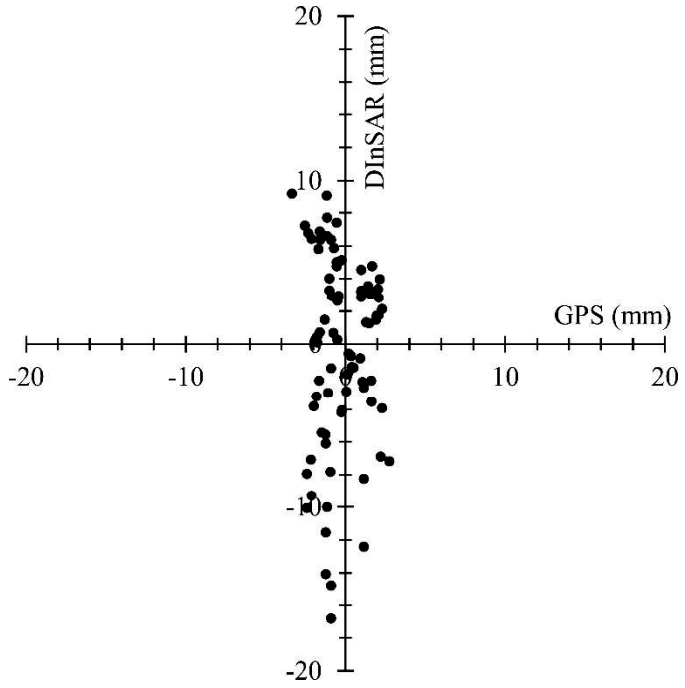

Figure 3.9. Scatter plot of displacements by DInSAR (vertical axis) and GPS (horizontal axis).

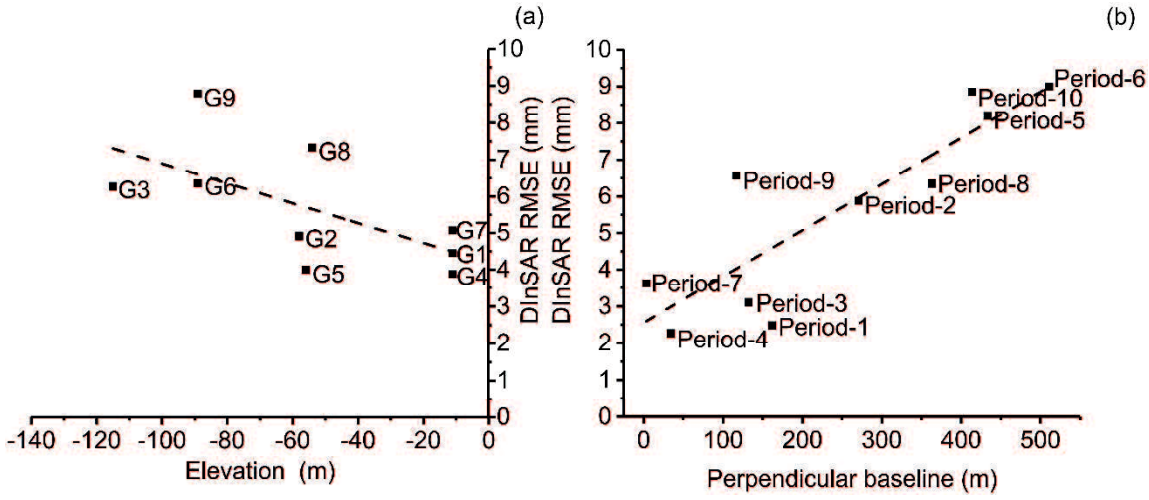

Figure 3.10. DInSAR RMSEs: (a) relationship between RSMEs and elevation of measurement point and (b) relationship between RSMEs and perpendicular baseline length.

It is found that DInSAR, using the updated digital elevation model, can provide good results with RMSEs of less than 10 mm compared to the GPS results. To provide cm-level accuracy in the monitoring results, the selection of SAR data with short perpendicular baselines (less than 200 m in this study) is recommended.

3.4 Summary of Chapter 3

In this chapter, the effects of different digital elevation models on the displacement results by the DInSAR technique have been examined, and the applicability of DInSAR to displacement monitoring at a limestone quarry has been investigated. The following conclusions can be made:

1. Public digital elevation models do not seem to be adequate for representing the topography of the open-pit mine in this study because the digital elevation models are generated on certain dates and not regularly updated. On the other hand, the InSAR procedure can overcome such a problem by updating the digital elevation model at the site.
2. Errors in public digital elevation models affect the measurement results of DInSAR. In some cases, the error becomes more than several 100 mm. Such a tendency increases when the perpendicular baseline length is long. As long as an updated digital elevation model is used, errors in the displacement will remain within 10-20 mm at this quarry.
3. DInSAR, using the updated digital elevation model by InSAR, can provide good results with RMSEs of less than 10 mm compared to the GPS results. If the monitoring requires cm-level accuracy, the selection of SAR data with short perpendicular baselines (less than 200 m in this study) is recommended.
4. InSAR is one of the effective solutions for updating digital elevation models for open-pit mine slopes. It is very important to check and update the digital elevation models before applying DInSAR to open-pit mine slope monitoring.

Chapter 4. Application of SBAS-DInSAR for Monitoring the Subsidence Induced by Underground Mining

4.1 Introduction

The subsidence in Tuzla has been creating a large hazard for a long period of time, mainly since 1950. It has been reported that the major factor in this subsidence is the salt mining activities (Mancini et al., 2009a, 2009b; Stecchi, 2008; Stecchi et al., 2009). Subsidence of up to 12 m was reported to have been measured by traditional topographic surveys from 1956 to 2003 (Mancini et al., 2009b). The next series of studies on the subsidence in Tuzla was conducted four times by means of static GPS surveys in 2004, 2005, 2006, and 2007 (Mancini et al., 2009a; Stecchi, 2008). These GPS surveys produced subsidence information for three periods, namely, 2004-2005, 2005-2006, and 2006-2007, and it was found that the subsidence was generally decreasing, except in the area near Pannonica Lake (Mancini et al., 2009a; Stecchi, 2008).

The present subsidence is being monitored by means of classical geodetic measurement and the real-time kinematic GNSS monitoring system. Three GNSS stations have been installed: one is for the reference point and the other two are for measurement points (Čeliković and Imamović, 2016). Since this monitoring system provides temporal subsidence information only at certain points and annual information at a few benchmarks, the results show a lack of spatial coverage.

The problems of subsidence monitoring in Tuzla can be summarized as follows: (1) there is a lack of information on the spatial distribution of the present subsidence, (2) conducting conventional, annual or periodical GPS surveys is costly, requires much labor and time, and involves difficulties in terms of obtaining the continuous temporal transition of the subsidence, and (3) the installation of a number of real-time kinematic GNSS sensors is one solution for improving the spatial and temporal coverage of the monitoring results; however, it is costly.

Therefore, an efficient, effective, and economic method is required to overcome the above problems. Differential Interferometric Synthetic Aperture Radar (DInSAR) is employed in the present study for this purpose. With DInSAR, it is possible to measure ground surface displacements with accuracy of a few centimeters from the satellite data which were taken more than 500-700 km away from the Earth's surface (Ferretti, 2014). This accuracy can be improved by applying several error corrections and using a large amount of satellite data

(Berardino et al., 2002; Ferretti et al., 2000). The other advantages of DInSAR are that it can monitor extensive areas (i.e., over thousands of square kilometers) without any sensors or targets on the ground surface.

DInSAR has been applied to various projects related to rock mechanics and geotechnical engineering, such as land subsidence (Vervoort and Declercq, 2018; Wempen and McCarter, 2017), landslides (Barla, 2018; Delle Piane et al., 2016), and other ground displacements (Ciantia et al., 2018; Janna et al., 2012; Rutqvist et al., 2016). Several examples of the application of DInSAR related to ground movement induced by mining activities have been given by Guido et al. (2015), Herrera et al. (2010), Vervoort and Declercq (2018), Wempen and McCarter (2017), and Woo et al. (2012). Those researches demonstrated the applicability and effectiveness of DInSAR; however, the results were seen to depend on the ground surface conditions, topography, and other conditions. Therefore, the availability of its application must be investigated in detail and the computing process should be tuned appropriately for each applied case.

The main objectives of this part of the study are: (1) to evaluate the validity and applicability of DInSAR for monitoring the subsidence in target areas from the viewpoints of spatial distribution and temporal transition and (2) to enhance the former subsidence information and to provide the present situation of the subsidence in Tuzla. In this study, the Synthetic Aperture Radar (SAR) data from the Sentinel-1A and -1B satellites, operated by the European Space Agency (ESA), are used. The Small Baseline Subset algorithm (Berardino et al., 2002) is employed to obtain the time-series subsidence.

4.2 Study area, data sources, and methodology

4.2.1 Study area

The study area is located in Tuzla City, in the northeast part of Bosnia and Herzegovina (Figure 4.1). Tuzla is the third largest city in Bosnia and Herzegovina. It has a population of about 110,000. Tuzla is famous for salt mining, and massive salt exploitation was conducted during the years of 1956 to 1988 (Mancini et al., 2009b).

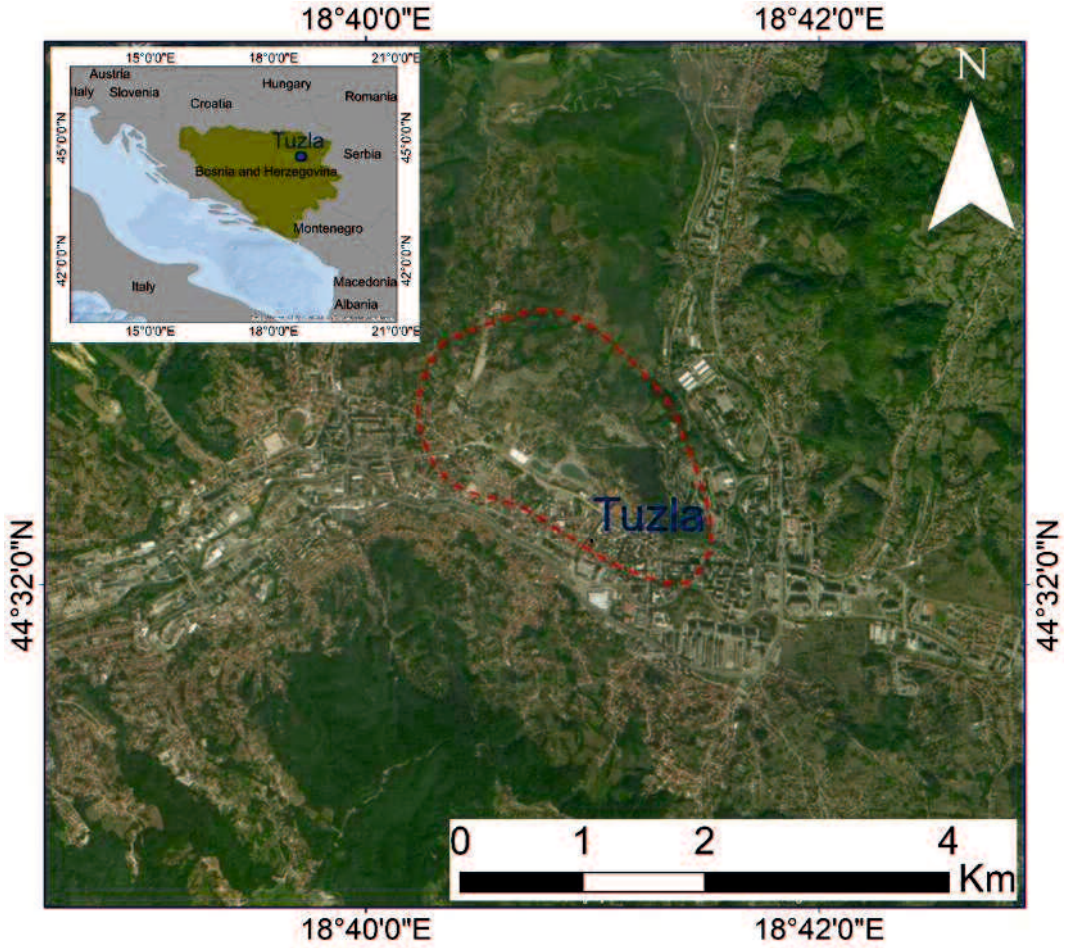

Figure 4.1. Map of Tuzla City and subsidence boundary (red dashed line).

4.2.1.1 Geological setting and salt mining history

The Tuzla salt deposit geology has been investigated by several authors (Cicić, 2002; Hrvatović, 2006; Jovanović, 1980; Katzer, 1903; Soklić, 1982, 1964, 1959; Stevanović, 1977; Tari and Pamić, 1998; Vrabac, 1999). The Tuzla salt deposit region is located beneath Tuzla City and is approximately 2 km^2 in size (Figure 4.2 a). It consists of five separated series, or ground layers, which contain salt deposits embedded in syncline with one of the wings close to the surface of the city center (Figure 4.2 c). The maximum thickness of the salt formation is 600 meters. It is composed of marl with clay sandstones, band marl, weak rock, salt, anhydrate, and peripheral leaching products, as shown by the vertical section of X-X' in Figure 4.2 c.

The origin of this salt deposit region is related to the paleo-geological Pannonian Basin and the Paratethys Sea. It was a large shelf sea, stretching from Germany to China, during the beginning of the Oligocene epoch (about 34 million years ago). After paleomorphological changes, the Black Sea, Caspian Lake, and Aral Lake are today's

remnants of the Paratethys Sea. The Tuzla Basin was one of the most important basins at the southern edge of the Central Paratethys (Pannonian Basin) during the Miocene epoch (from the Badenian stage to the Pontian stage). The conditions of the lagoon sedimentation and the arid climate contributed to the formation of salt deposits in the Tuzla Basin in the period of the Early Badenian stage. For a relatively short geological period, the Central Paratethys was isolated, but for most of the time it was connected to the Eastern Paratethys (Vrabac, 2005). The rock salt deposit is located inside the "striped series" of marls. It consists of five series, marked as I, II, IIIA, IIIB, and IV, and is shown in Figure 4.2 c (Ferhatbegovic, 2004).

The primitive salt exploitation was done by natural brine and shallow salt water wells in the Neolithic period 6000 years ago. This was confirmed by the discovery of the ceramic fragments of holders from 3500 BC, used to boil saltwater above hot charcoal (Bakalović, 2005; Stecchi, 2008). During the Ottoman-Turkish Empire, salt water exploitation was done by shallow wells, at depths of about 60 m, and the production of salt in that period amounted to 2500 kg/day (Jokanovic, 1952).

The salt deposit region in Tuzla consists of three main areas, i.e., underground salt mining in the Tusanj area, borehole salt mining in Hukalo and Trnovac, and the safety pillar area, as shown in Figure 4.2 c (Ferhatbegovic, 2004).

Underground mining was conducted in Tusanj from 1967 to 2002 by means of the classical room-pillar method and crude-dry salt was extracted during this period. In the same mine in Tusanj, from 1983 to 1992, so called “controlled leaching” was conducted in lower mining rooms to extract dissolved salt, which was pumped out of the underground mine through pipelines. The Tusanj mine was flooded by dissolved salt and had to be closed from 2002 to 2004 (Tomić et al., 2005). Salt water extraction was conducted in the Hukalo and Trnovac areas, from 1906-2006, using a borehole method (Čeliković et al., 2014). This method is known as the “uncontrolled leaching method” because it is impossible to control which part of the deposit is leached. The location of boreholes (salt wells) are indicated by bullets in Figure 4.2 b. Borehole salt mining was initially carried out by the injection of fresh water to speed up the dissolution process. The fresh water injection process was conducted for only 6 months; it was stopped due to the appearance of a 50-m-diameter sinkhole in a suburban area in 1987 (Mancini et al., 2009a; Stecchi et al., 2009). The area between the underground mining in Tusanj and the borehole mining in Hukalo and Trnovac was unexcavated and left as a safety pillar. A safety pillar is a type of natural protection; it does not require any additional construction work or reinforcements (Ferhatbegovic, 2004).

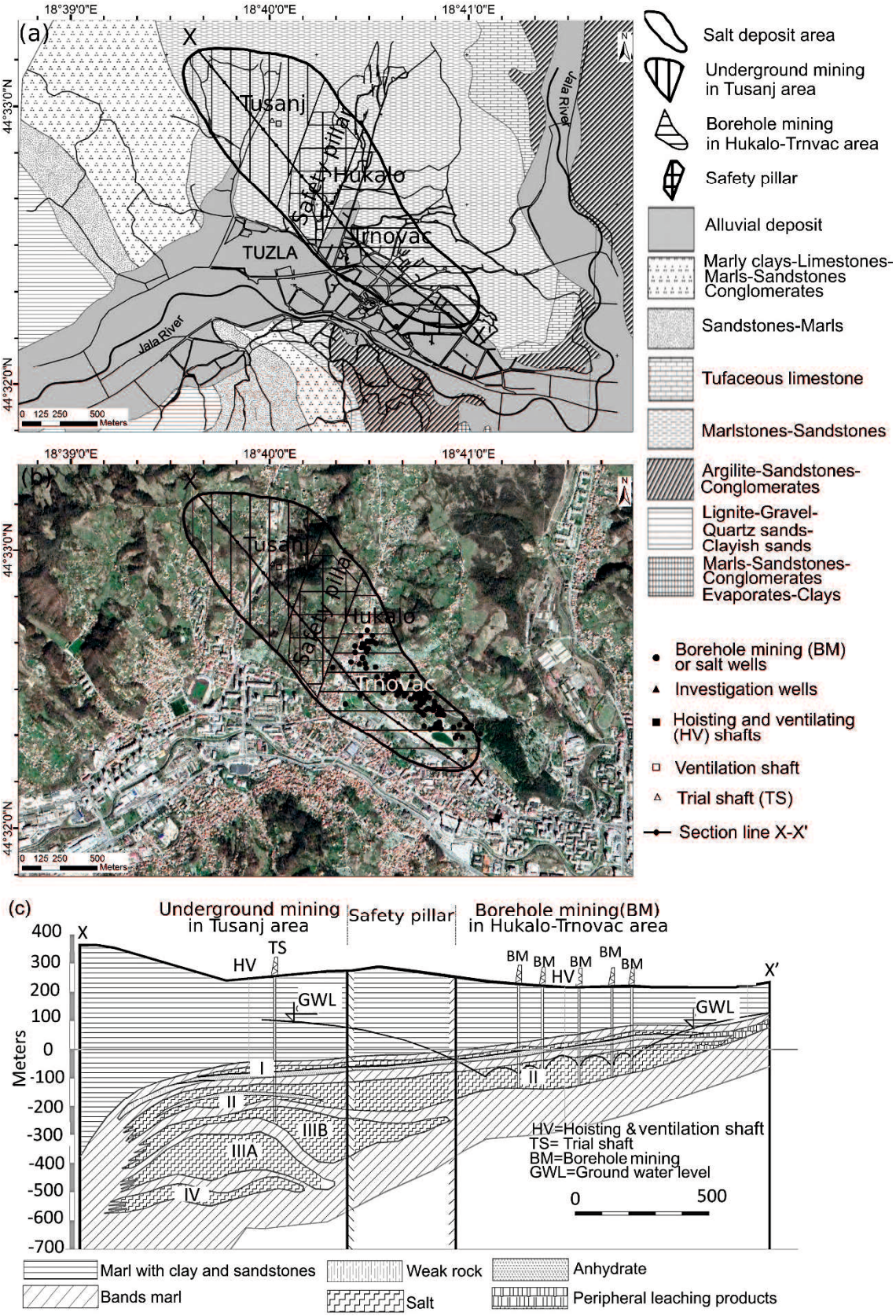

Figure 4.2. Geological conditions of Tuzla: (a) plan view (modified from Mancini et al. (2009a)), (b) plan view using background aerial photo from Google Earth Pro and location of salt wells, and (c) vertical X-X' cross section (Ferhatbegovic, 2004).

The intensive production of salt water (by the uncontrolled leaching method) caused extensive subsidence of up to -12 m of the terrain in the urban area of Tuzla. It induced serious damage to buildings and the infrastructure, such as water supply systems, sewage networks, and electric powerlines (Stecchi et al., 2009). For this reason, more than 2000 buildings collapsed or needed to be demolished and about 15,000 people had to evacuate the most affected area (Stecchi et al., 2009). Another report (Ibreljić et al., 2007) mentioned that 2300 apartment buildings were destroyed between 1965 and 1990 due to the subsidence phenomenon. The decision to stop the exploitation of salt was made in order to reduce the subsidence. In the period from March 2006 to May 2007, a gradual suspension of the salt well exploitation was carried out. The official date of termination of the Tuzla salt deposit exploitation is May 29, 2007 (Čeliković and Imamović, 2016).

4.2.2 Former monitoring results of subsidence

Several investigations and geodetic surveys have been conducted to monitor the subsidence in different periods, i.e., traditional topographic surveys (1950-2003) (Mancini et al., 2009b), static GPS surveys (2004-2007) (Stecchi, 2008), and real-time kinematic GNSS monitoring (2010-present day) (Čeliković and Imamović, 2016).

4.2.2.1 Traditional topographic surveys until 2003

The first geodetic survey was conducted in Tuzla in 1914 (Mancini, 2009b). Then, an annual geodetic survey to measure the subsidence due to salt mining was started in 1956. It was continued until 1992 when it was temporarily suspended due to the Balkan War. These long-term surveys produced a large amount of topographical data. From 1992-2003, the results of the geodetic surveys were not as reliable as in the previous period due to the loss of data from several measurement points that were destroyed during the war. One analysis of the topographical data was conducted by Mancini et al. (2009a, 2009b) and revealed that the ground surface had sunk up to -12 m. These results are presented in Figure 4.3 a by contour lines (Mancini et al., 2009a). It was found that large subsidence extended to the north part of the city, including the residential area, and was shaped like a bowl.

Figure 4.3 b presents the relationship between the annual average subsidence in cm/year (solid line) and the annual amount of brine water pumped in m^3 (dashed line). The annual volume of extracted salt water was estimated from the mining database, and the annual average subsidence was calculated by the representative subsidence for the whole area and

during the period of 1956-1992 (Mancini et al., 2009a). A remarkable correlation is shown around 1982 when the salt water extractions were reduced and the subsidence rate decreased (Figure 4.3 b). It is seen that halving the salt water extraction from the year 1982 induced a reduction in the annual subsidence rate to approximately one half of that of the previous value (Mancini et al., 2009a).

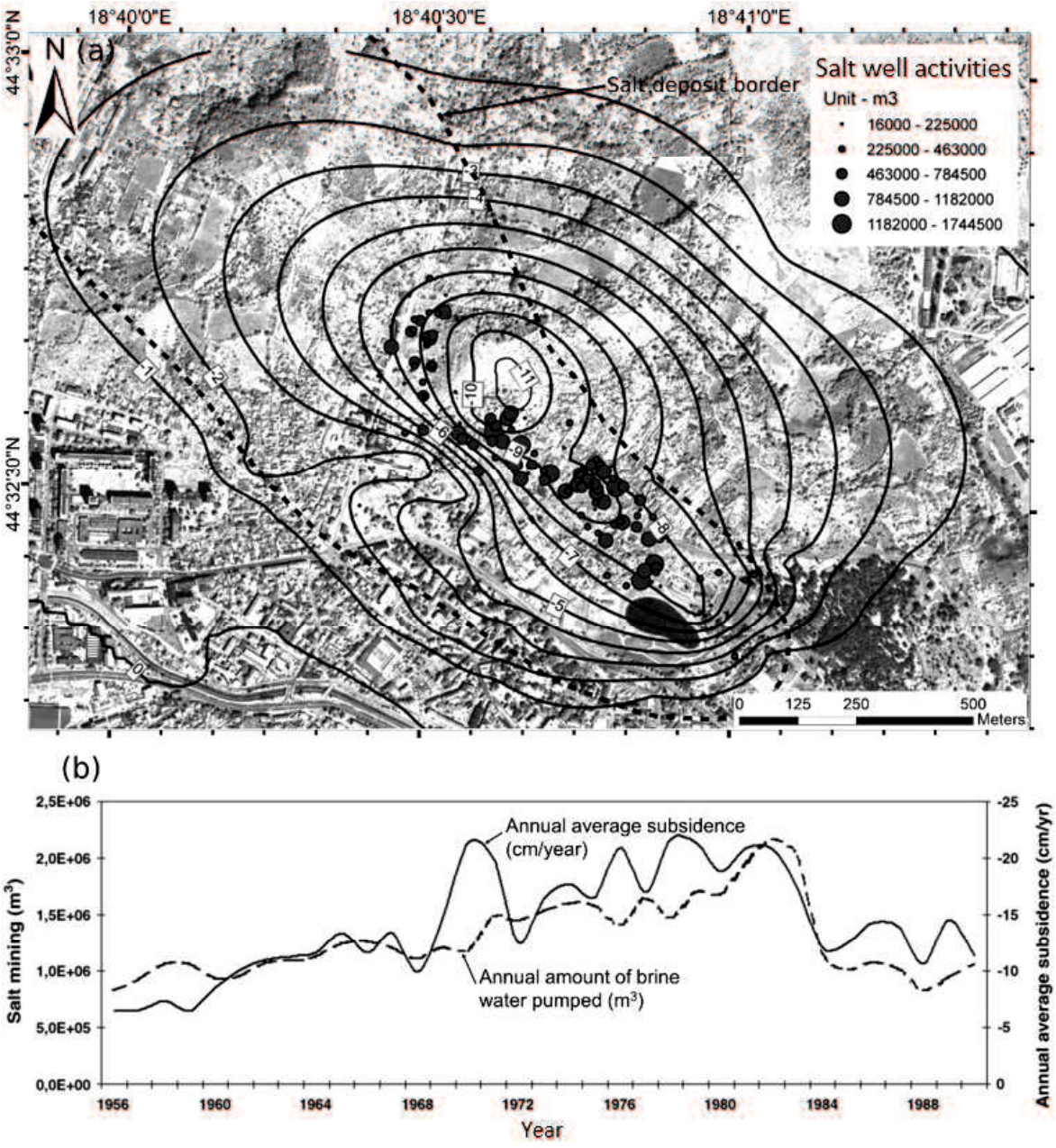

Figure 4.3. Cumulative subsidence and its relationship to annual amount of brine water pumped: (a) cumulative subsidence obtained by traditional topographic surveys from 1956-2003 presented by contour lines (dashed line indicates salt deposit border added by the authors) and (b) comparison between annual average subsidence in cm/year (solid line) and annual amount of brine water pumped in m^3 (dashed line). It is limited to the period of 1956-1992 (modified from Mancini et al. (2009a)).

4.2.2.2 Static GPS surveys

Static GPS surveys were conducted four times, namely, in 2004, 2005, 2006, and 2007 (Mancini et al., 2009a; Stecchi, 2008). The survey network was composed of six reference points and 60 densification measurement points (Mancini et al., 2009a). The results of the GPS surveys are presented in Figure 4.4. Figures 4.4 a, b, and c show the subsidence distributions, while Figure 4.4 d shows the location of the densification and reference points of the GPS surveys.

The GPS results for 2004-2005 show that the subsidence continued at a rate of -10 ~ -20 cm/year in the north part of Pannonica Lake (Figure 4.4 a), although the subsidence rate had decreased a great deal compared with that of the previous period (1956-2003). A considerable part of the northeast part of the city was subjected to subsidence rates of -2 ~ -5 cm/year. In the period of 2005-2006, the subsidence rate totally decreased to -10 ~ -20 cm/year around Pannonica Lake (Figure 4.4 b). Mancini et al. (2009a) and Stecchi (2008) stated that the last GPS results from 2006-2007 showed that the subsidence was approaching the end almost everywhere, except for in the area near Pannonica Lake where the subsidence rate was still about 10 cm/year (Mancini et al., 2009a; Stecchi, 2008).

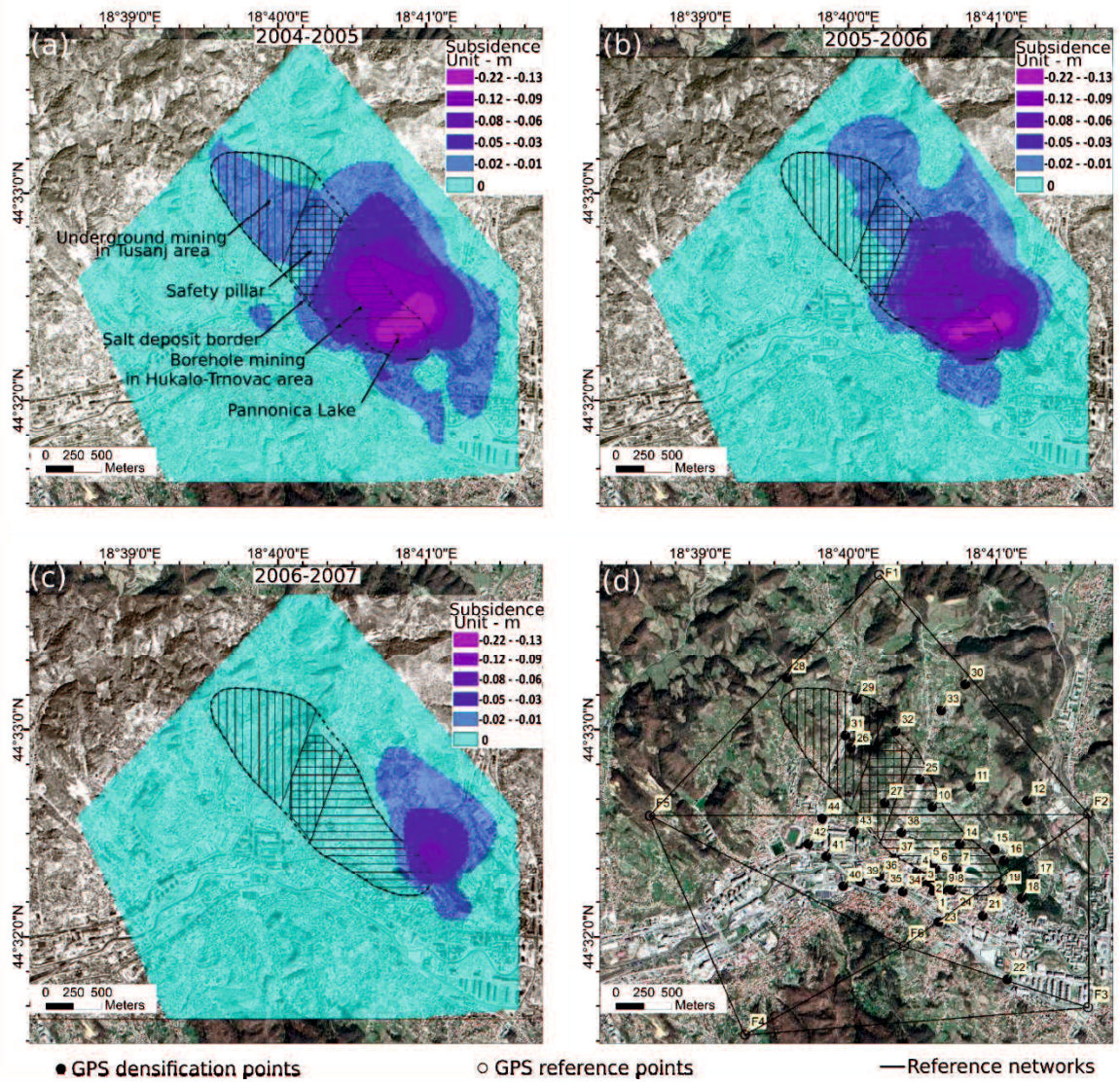

Figure 4.4. Subsidence in Tuzla obtained by GPS surveys: (a) subsidence from 2004 to 2005, (b) subsidence from 2005 to 2006, (c) subsidence from 2006 to 2007 (modified from Stecchi (2008)) (salt deposit border, safety pillar, and mining region were added by the authors), and (d) map of GPS densification and reference points (re-drawn from Stecchi (2008) and Mancini et al. (2009a)).

4.2.2.3 Real-time kinematic GNSS monitoring

The real-time kinematic GNSS monitoring system was installed to monitor the subsidence in Tuzla. Three GNSS sensors were installed in the city (Čeliković and Imamović 2016). The results will be shown in **section 4.3.2.**

4.2.3 Data sources

The SAR data acquired with TOPSAR (Zan and Guarnieri, 2006) by means of the Sentinel-1A and -1B satellites, operated by the ESA, are used in this study. Since the data from Sentinel-1A and -1B is available free of charge, economical monitoring can be realized.

The total amount of data used in this study comprises 199 sets of SAR data (Table 4.1), which were taken from October 9, 2014 to May 28, 2019 in the descending orbit direction. The path and the frame numbers of the SAR data are 51 and 442-446, respectively. Details of the Sentinel-1 dataset are presented in the Appendix (Table. A - 1). Since Sentinel-1A and -1B are in active operation, the SAR data can be updated every 6-12 days.

In addition, the SAR data from the Advanced Land Observing Satellite-2 (ALOS-2) is used to complement the Sentinel-1 data. Only a single pair of SAR data is used. The master data were obtained on May 24, 2016 and the slave data were obtained on May 23, 2017. The time span is almost one year.

Table 4.1. SAR data sources used in SBAS-DInSAR analysis for monitoring subsidence induced by salt mining activities in Tuzla, Bosnia and Herzegovina.

Satellite name	Number of SAR data	Period		Orbit direction	Observation mode
		from	to		
Sentinel 1 A and B	199 scenes	October 9, 2014	May 28, 2019	Descending	Right-looking
ALOS-2 PALSAR-2	2 scenes	May 24, 2016	May 23, 2017	Ascending	Right-looking

4.2.4 Methodology (SBAS-DInSAR processing steps and parameter setting)

In this study, the Envi SARscape version 5.5.2 (SARMAP 2019) is used as the SAR processor for conducting the SBAS-DInSAR analysis. The first step is the selection of the SAR data pair combinations done by assigning threshold values to the temporal and spatial baselines. The maximum temporal baseline and the maximum spatial baseline are set at 48 days and 150 meters, respectively. This produces the possible combinations from the 199 sets of SAR data (Table 4.1), as shown in Figure 4.5. These threshold values result in a total of 544 combinations (interferograms) to be analyzed. Then, all the possible pairs are processed using the conventional DInSAR method. The digital elevation model (DEM) provided by JAXA (Japan Aerospace Exploration Agency), ALOS World 3D - 30m (AW3D30) (Takaku and Tadono, 2017), is used to remove the topographic phase effects.

The interferograms and the coherence, which are indices representing the reliability of the results of the interferograms, were produced in this step and are checked. The eight sets of SAR data with low coherence (presented by the red diamonds in Figure 4.5) are removed from the SBAS analysis in order to reduce the errors in the analysis.

After the SBAS process, the time-series spatial distribution of the LOS displacements is obtained for all the dates on which the SAR data were observed. The spatial resolution of the displacement is 25 m x 25 m in this study. Details on the data processing parameters are presented in Table 4.2.

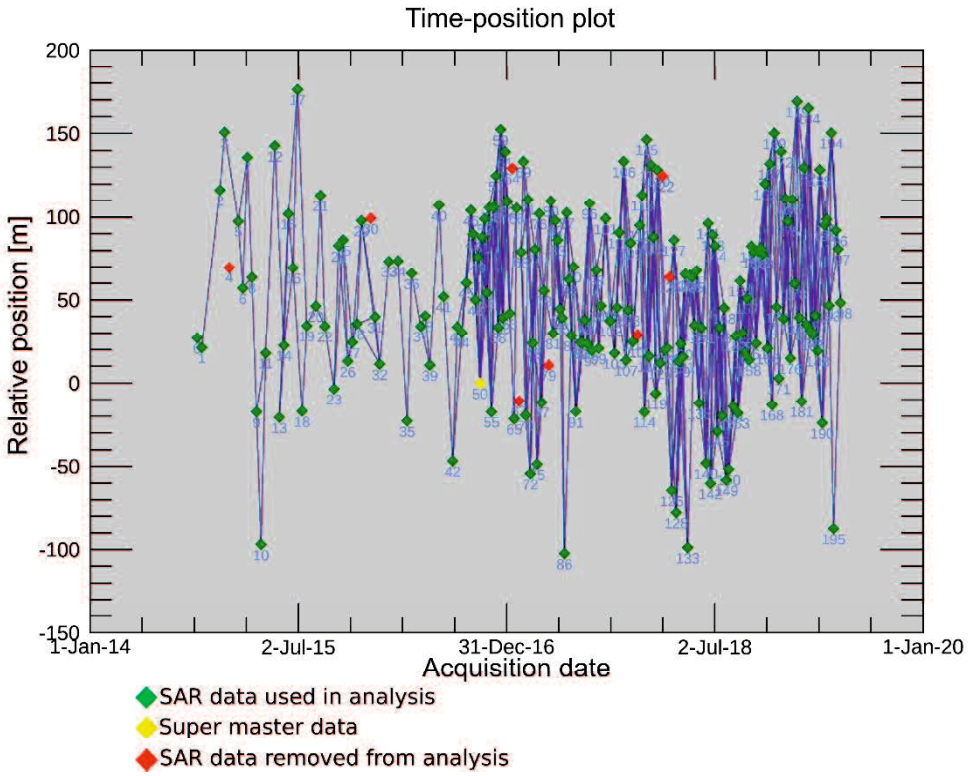

Figure 4.5. Combinations of SAR pairs used in SBAS-DInSAR analysis. The green diamonds indicate the number of SAR images used in the SBAS-DInSAR analysis, the red diamonds indicate that the SAR images were either not used or removed from the SBAS-DInSAR analysis, and the yellow diamond indicates the super master data.

Table 4.2. SBAS-DInSAR processing steps and parameters setting for monitoring the ground subsidence induced by salt mining activities in Tuzla, Bosnia and Herzegovina.

Processing step	Parameter name	Parameter value/setting
(1) Connection graph	Maximal perpendicular baseline ($b_\perp$)	150 m
	Maximal temporal baseline (b_t)	24 days
(2) Interferometric process	External DEM	AW3D30-DEM
	Range looks	6 looks
	Azimuth looks	1 looks

	Co-registration with external DEM	True
	Unwrapping method	Minimum cost flow
	Unwrapping threshold	0.2
	Filtering method	Goldstein
(3) Refinement and re-flattening	GCPs file	Geographic GCPs
	Refinement method	Residual phase
	Refinement polynomial degree	3
(4) Inversion: First step	Product coherence threshold	0.4
	Displacement model	Linear model
(5) Inversion: Second step	Product coherence threshold	0.4
	Atmospheric low pass filter window size	1200 m
	Atmospheric high pass filter window size	365 days
(6) Geocoding	Coordinate system projection	Geographic WGS84
	Final pixel size (resolution)	25 m x 25 m

4.3 Results and discussion

4.3.1 Spatial distribution of subsidence

The results of the distribution maps of the subsidence were obtained by SBAS-DInSAR, as described in section 4.2.4. The total number of maps is 198. Figure 4.6 shows some of them as examples; they indicate the time transition of the subsidence distribution.

It is clearly found that the larger subsidence area, represented by yellow and red colors, is located in the northeast part of Pannonica Lake (Figure 4.6 f). The accumulated subsidence from October 2014 to May 2019 is around 100-200 mm in this area, while it is less than 100 mm in the area above the salt mine deposit. Around the safety pillar, which is an unexcavated area, as well as the area outside of the salt deposit around the downtown section of the city, almost no subsidence has occurred over the last four and a half years.

On the other hand, there are no results for some parts of the maps especially in the area with high vegetation coverage. This is due to the weak or the lack of microwave reflections and to the changes in the growing situation in high vegetation areas that cause the low coherence of the interferograms, which means SBAS-DInSAR cannot provide reliable solutions (Ferretti, 2014).

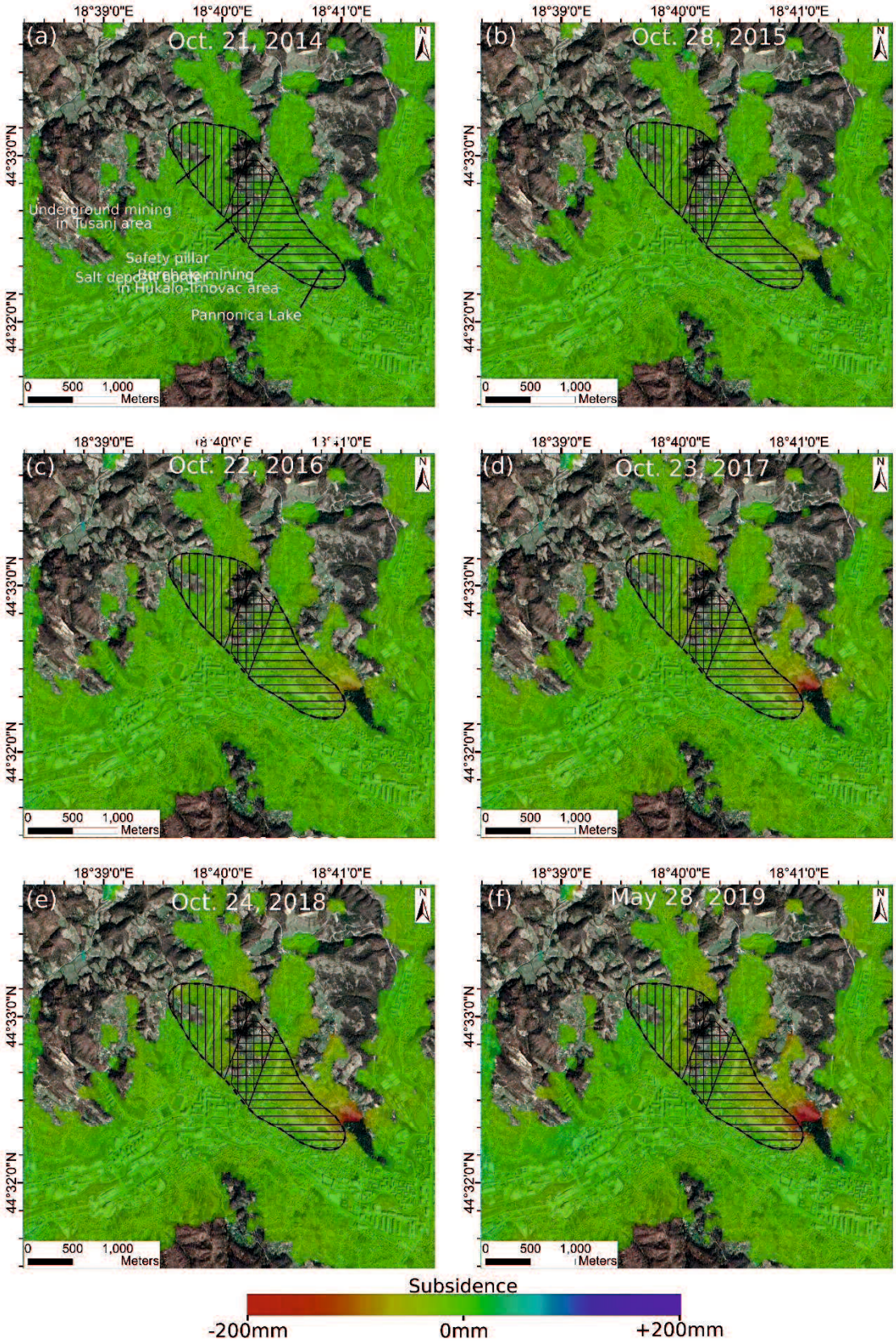

Figure 4.6. Subsidence distribution obtained by SBAS-DInSAR on several dates: (a) October 21, 2014, (b) October 28, 2015, (c) October 22, 2016, (d) October 23, 2017, (e) October 24, 2018, and (f) May 28, 2019.

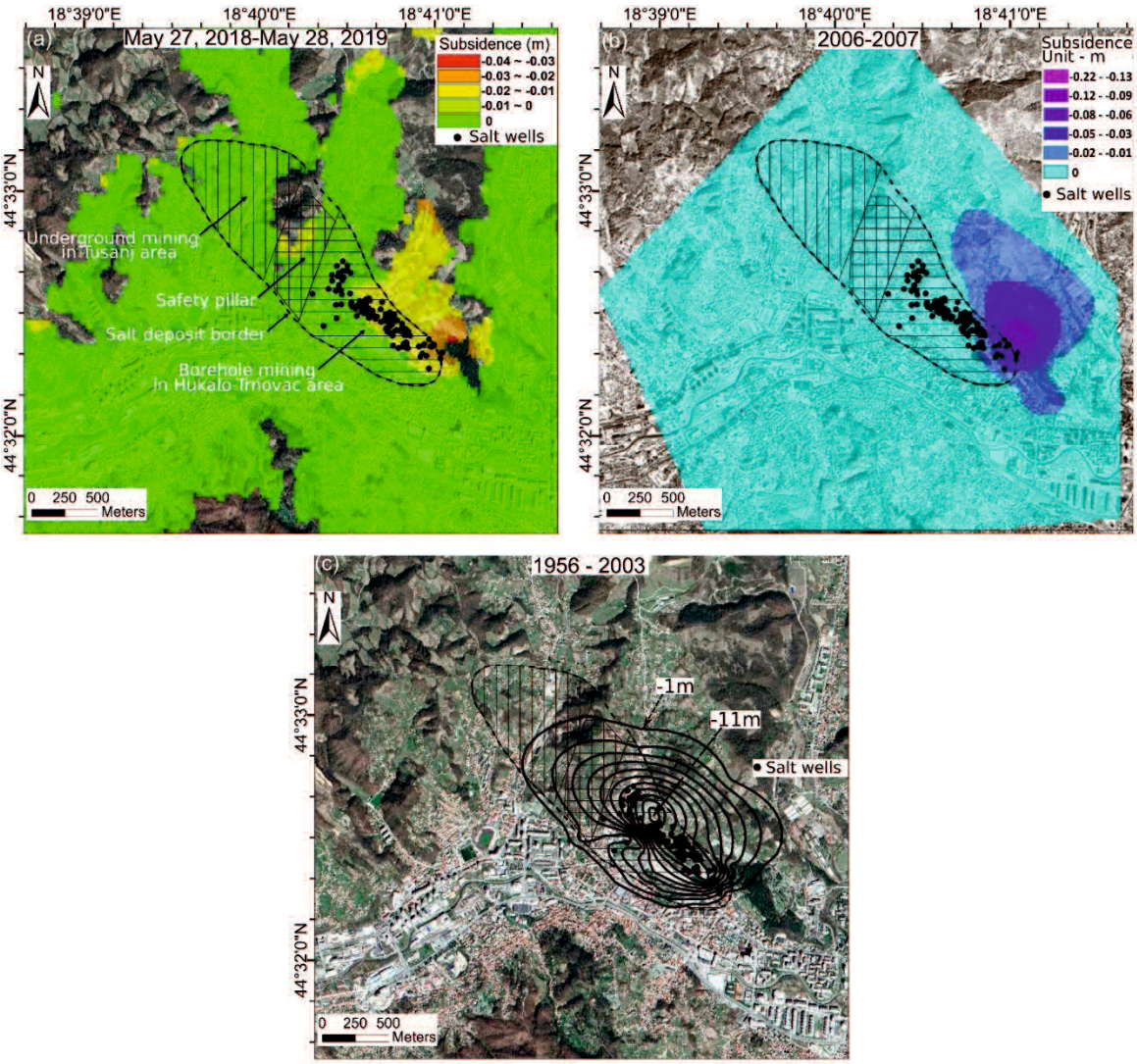

Figure 4.7. Comparison of subsidence distributions obtained by different methods and in different periods: (a) subsidence distribution obtained by SBAS-DInSAR from May 27, 2018 to May 28, 2019, (b) subsidence distribution obtained by GPS surveys from 2006-2007 (modified from Stecchi (2008)), and (c) subsidence distribution obtained by traditional topographical surveys from 1956 to 2003 (re-drawn from Mancini et al. (2009b)).

The spatial distribution of the subsidence obtained by SBAS-DInSAR for a year (from May 2018 to May 2019) is compared with distributions by GPS surveys (from 2006 to 2007) and traditional topographical surveys (from 1956 to 2003) in Figure 4.7. It is found that the subsidence distribution by SBAS-DInSAR is similar to those by the GPS surveys, while it is different from those by the traditional topographical surveys. The location of the large subsidence area is seen to have moved to the southeast border of the salt mine deposit (northeast of Pannonica Lake), while it was located in the center of the salt mine region in the previous period (1956-2003). This means that the subsidence has continued in the same place since the last GPS survey even after the termination of the salt water extraction in 2007.

A comparison of the subsidence shapes and values, obtained by the traditional topographical surveys and by SBAS-DInSAR, is illustrated in Figure 4.8 in section lines A-A' and B-B'.

Figure 4.8 c shows the subsidence along section line A-A'. A large subsidence of more than 1 m (up to -12 m) appeared from a distance of around 400 m to 1400 m from point "A", and its peak was found at a distance of around 910 m from point "A" during the period of 1956-2003 (Mancini et al., 2009a). According to the SBAS-DInSAR results, the magnitude of subsidence decreased greatly and subsidence of up to -115 mm occurred at a distance of 1650 m from point "A" during the period of 2014-2019.

The subsidence by SBAS-DInSAR and the traditional topographic surveys along section line B-B' are shown in Figure 4.8 d (Mancini et al., 2009a). The figure shows that a larger subsidence than -40 mm occurred at a distance of 1000 to 1800 m from point "B". The subsidence between this distance of 1250 and 1570 m from point "B" could not be computed because of the low coherence of the interferograms due to the vegetation conditions.

Section lines A-A' and B-B' were set by Mancini et al. (2009a) to show the shapes and the maximum subsidence obtained by the traditional topographical surveys in the vertical section. In a similar way, to investigate the SBAS-DInSAR results, two section lines, C-C' and D-D', were newly set to present the distributions of subsidence obtained by SBAS-DInSAR, including the maximum subsidence. Figures 4.8 e and f show subsidence of more than -40 mm (up to -160 mm) along lines C-C' and D-D' from a distance of about 700 m to 1900 m from point "C", and from a distance of about 600 m to 1200 m from point "D", respectively. It is found that the area of the maximum subsidence is located outside of the salt deposit around the northeast part of Pannonica Lake. The extent of the subsidence area has been reduced, and its amount has also greatly decreased.

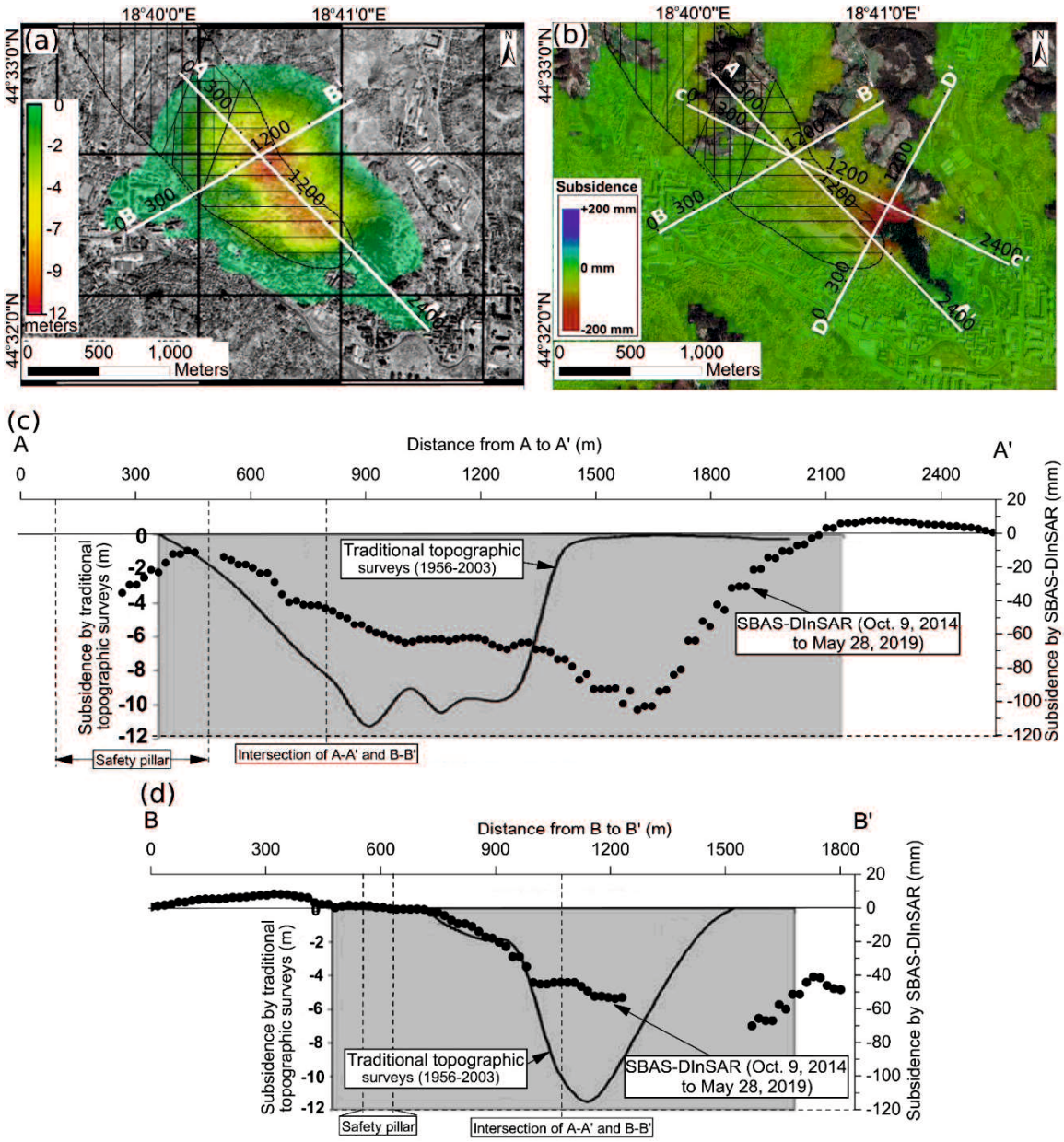
(a)
18°40'0"E
18°41'0"E
44°33'0"N
44°32'0"N
0
-2
-4
-7
-9
-12
meters
0 500 1,000
Meters
(b)
Subsidence
+200 mm
0 mm
-200 mm
(c)
A
A'
Distance from A to A' (m)
Subsidence by traditional topographic surveys (m)
Subsidence by SBAS-DInSAR (mm)
Traditional topographic surveys (1956-2003)
SBAS-DInSAR (Oct. 9, 2014 to May 28, 2019)
Safety pillar
Intersection of A-A' and B-B'
(d)
B
B'
Distance from B to B' (m)

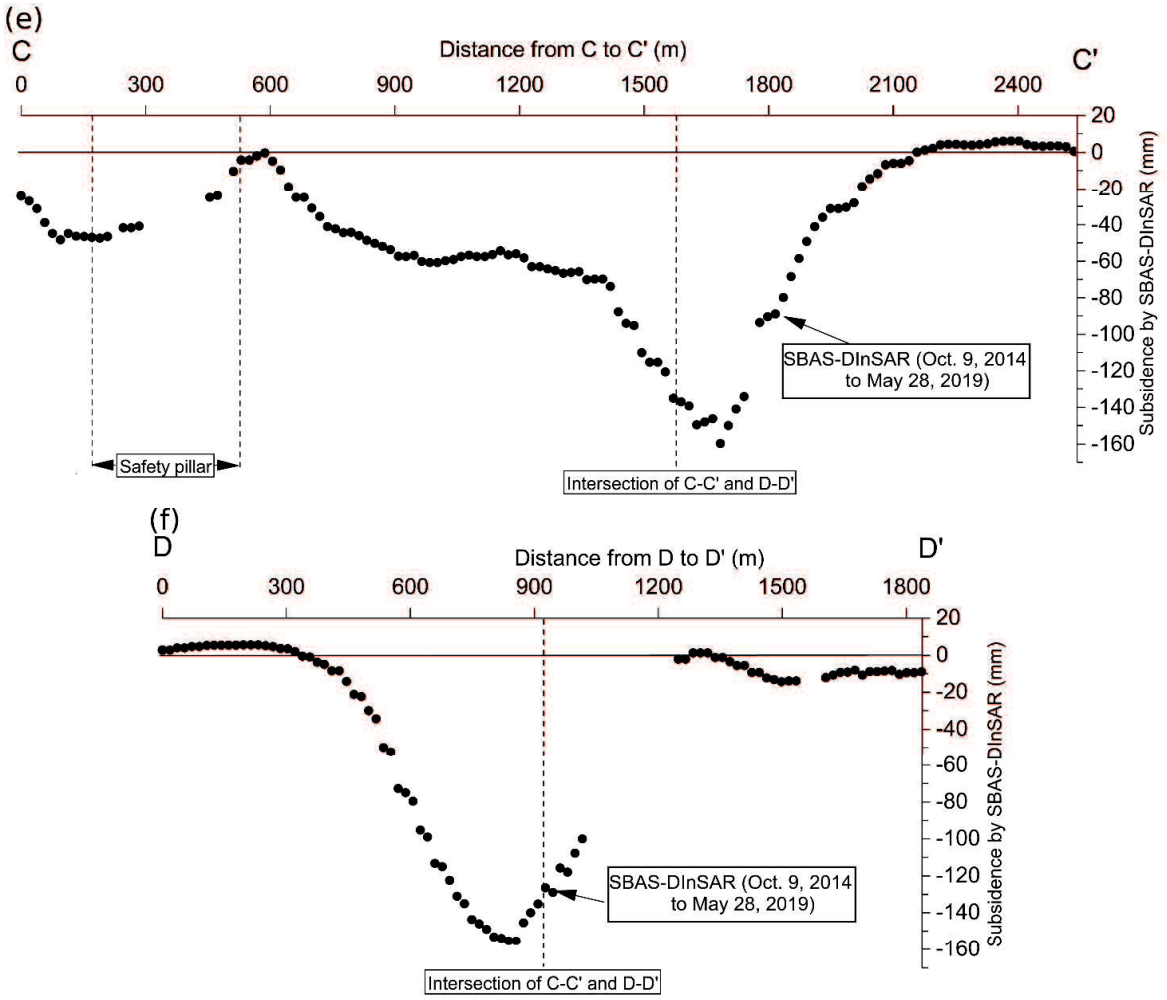

Figure 4.8. Subsidence obtained by SBAS-DInSAR and traditional topographic surveys (Mancini et al. 2009b): (a) subsidence obtained by traditional topographical surveys 1956-2003 (modified from Mancini et al. (2009b)), (b) subsidence obtained by SBAS-DInSAR October 9, 2014 to May 28, 2019, (c) section A-A', (d) section B-B', (e) section C-C', and (f) section D-D'.

4.3.2 Temporal transition of subsidence

The subsidence obtained by the GNSS monitoring system is used to validate the subsidence obtained by SBAS-DInSAR. The GNSS stations have been installed at three points, namely, Tusanj, Pannonica, and Tuzula, and those stations are monitoring displacements by the real-time kinematic method (Čeliković and Imamović, 2016). Tusanj and Pannonica stations are the monitoring points and Tuzula station is the reference point.

To make an appropriate comparison, the 3-dimensional displacements obtained by GNSS are projected into LOS displacements, as explained in section **2.1.6.**

Comparisons of the LOS displacements by GNSS and SBAS-DInSAR at Tusanj and Pannonica stations are shown in Figure 4.9. Since the GNSS results were greatly scattered, very few of them could be used. Figure 4.10 illustrates the relationship between the SBAS-DInSAR and GNSS results at Pannonica and Tusanj stations. It is seen that the SBAS-DInSAR results coincide with the GNSS results and that the discrepancy between the results is less than 10 mm. Figure 4.9 c is the LOS displacement at Tuzla station, which is located in a stable place. The displacement is within a few mm for the monitoring period, and it shows that there is almost no displacement.

From the above results, it is found that the SBAS-DInSAR results in this study are acceptable.

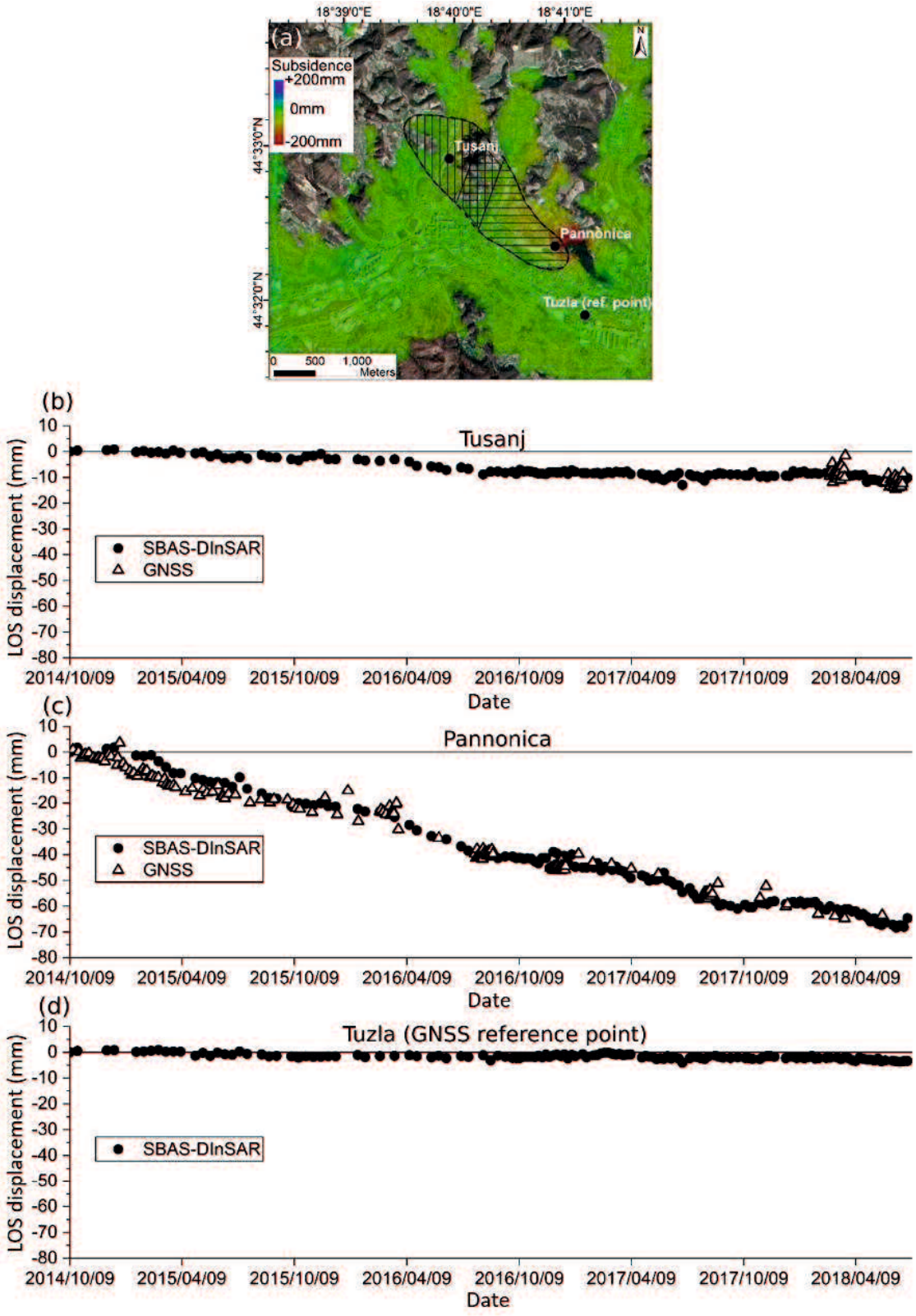

Figure 4.9. LOS displacements obtained by SBAS-DInSAR and GNSS at GNSS stations: (a) locations of GNSS stations, (b) Pannonica station, (c) Tusanj station, and (d) Tuzla station (reference point).

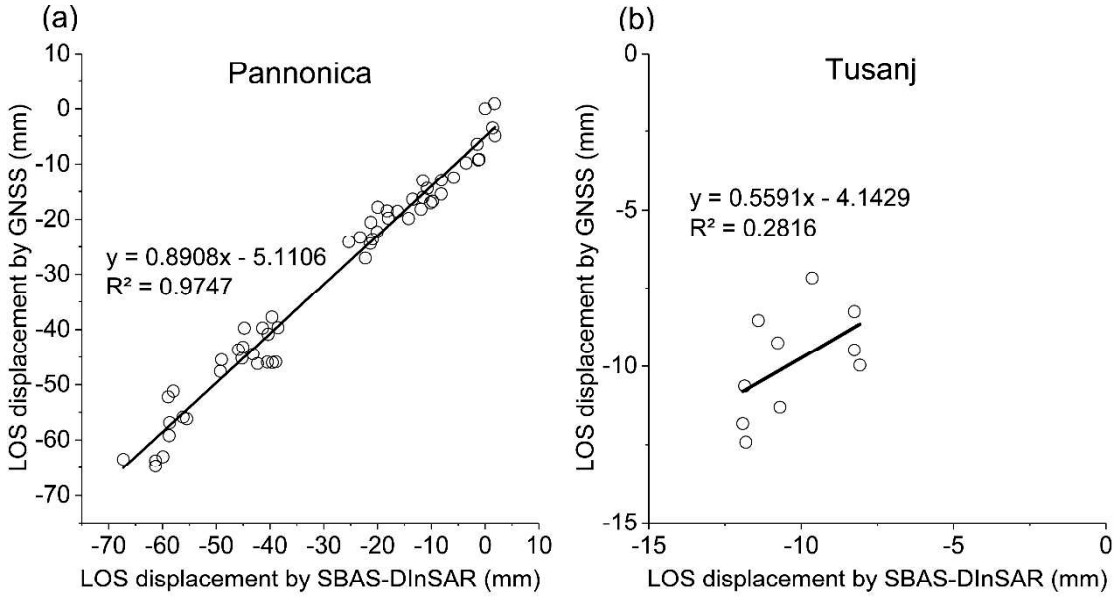

Figure 4.10. Scatter plot of LOS displacements obtained by SBAS-DInSAR and GNSS at Pannonica and Tusanj stations.

In order to assess the present trend of the subsidence, the time transitions from 2014 to 2019 obtained by SBAS-DInSAR are compared with the subsidence measured by GPS from 2004 to 2007 (Mancini et al., 2009a; Stecchi, 2008) at the GPS measurement points, as shown in Figure 4.11. Both time transitions of the subsidence by GPS and SBAS-DInSAR are presented at the selected points in Figure 4.12. The average subsidence rates per year were calculated for the GPS and SBAS-DInSAR results, as shown in Table 4.3.

The subsidence rates at points 10, 11, and 14-16 are still not small in both periods, 2004-2007 and 2014-2019 (Table 4.3). The average rates during 2014-2019 are -10 ~ -40 mm/year. Points 10 and 14 are located in areas where the subsidence reached more than 10 m during the period of 1956-2003 (Figure 4.13). This means that the subsidence in the areas near these two points has continued from 1956 until the present. Points 15 and 16 are located in the northeast part of Pannonica Lake where the maximum subsidence has been occurring since at least 2004 (see Figure 4.7). The points with the present subsidence rate of -10 ~ -40 mm/year are denoted by the bullet symbols in Figure 4.11 and Table 4.3.

The subsidence rates at points 5-7, 17-19, 25, 26, and 29-31 have been reduced to -3 ~ -10 mm/year. Those points are denoted by solid triangles in Figure 4.11. Figures 4.12 d-h show the results at points 6, 7, 19, 25, and 26, respectively.

At the other points, the subsidence rates have become very small, namely, within -3 mm/year, as shown in Table 4.3. Those points are located outside of the salt deposit area and

are denoted by circles in Figure 4.11. Figures 4.12 i-n show the results at points 20, 24, 36-38, and 41, respectively.

There are two points denoted by "X" in Figure 4.11 where no results were obtained due to the low coherence (less that the threshold value of 0.3) caused by the highly vegetated area.

As shown in section **4.2.2.2**, the subsidence rate in the area near Pannonica Lake was about -10 ~ -20 cm/year from 2006-2007. SBAS-DInSAR detected that the subsidence rate decreased to -10 to -40 mm/year in the same area and in the area where the large subsidence occurred from 1956-2003. The GPS results also showed that the subsidence seemed to approaching the end everywhere except for the area of Pannonica Lake from 2004-2007. However, SBAS-DInSAR detected that some small subsidence is still continuing to occur in the area above the salt mine deposit, which is presented by the yellow color in Figure 4.6 f and by the bullets and solid triangles in Figure 4.11. Therefore, it is important to continue to monitor the subsidence in this area.

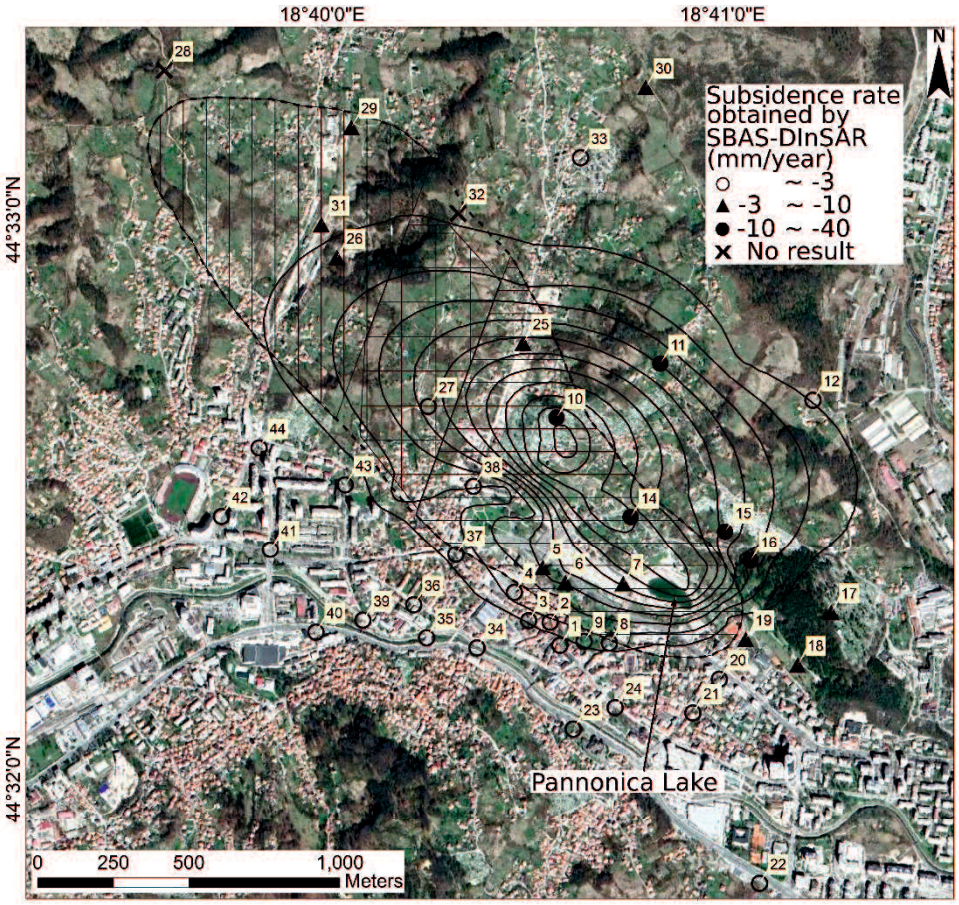

Figure 4.11. Locations of GPS survey points (2004-2007) superimposed with subsidence by traditional topographical surveys (contour lines, 1956-2003). The symbols of the points indicate the subsidence rate (mm/year) obtained by SBAS-DInSAR (2014-2019).

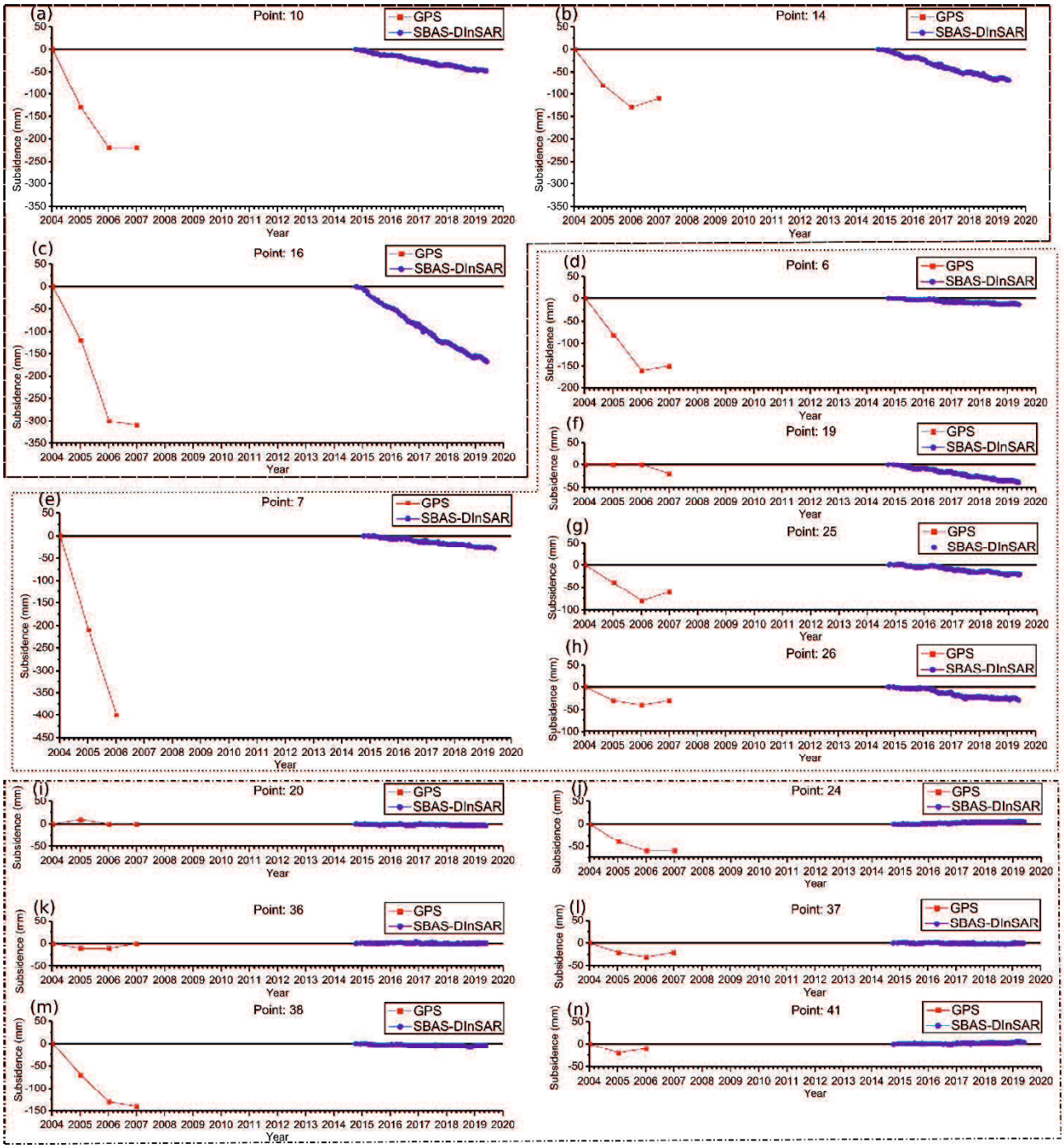

Figure 4.12. Time transition of subsidence obtained by GPS surveys (2004-2007) and SBAS-DInSAR (October 9, 2014 to May 28, 2019) at selected points.

Table 4.3. Subsidence trend between two measurements periods, 2004-2007 (by GPS survey) and 2014-2019 (by SBAS-DInSAR).

Station	Subsidence velocity (mm/year)		Symbol in Fig. 14
	2004-2007 (GPS)	2014-2019 (SBAS-DInSAR)	
1	3.33	0.89	O
2	-6.67	0.73	O
3	0.00	0.42	O
4	-10.00	-0.33	O
5	-53.33	-3.42	▲
6	-50.00	-3.05	▲
7	-200.00	-6.21	▲
8	6.67	0.48	O
9	-6.67	0.77	O
10	-73.33	-10.26	●
11	-46.67	-12.17	●
12	5.00	-0.75	O
14	-36.67	-14.71	●
15	-210.00	-25.98	●
16	-133.33	-36.28	●
17	0.00	-3.44	▲
18	-6.67	-3.33	▲
19	-6.67	-8.38	▲
20	0.00	-0.77	O
21	0.00	1.04	O
22	-10.00	0.25	O
23	-6.67	0.56	O
24	-20.00	1.09	O
25	-20.00	-4.41	▲
26	-10.00	-6.32	▲
27	-3.33	-1.71	O
28	0.00	No results	X
29	13.33	-5.78	▲
30	-6.67	-5.51	▲
31	-3.33	-4.13	▲
32	-10.00	No results	X
33	-5.00	-1.60	O
34	0.00	0.05	O
35	-6.67	-0.37	O
36	0.00	0.16	O
37	-6.67	-0.10	O
38	-46.67	-1.26	O
39	6.67	0.20	O
40	6.67	-0.09	O
41	-5.00	0.88	O
42	6.67	-0.31	O
43	6.67	0.90	O
44	6.67	0.39	O

4.3.3 Results of Sentinel-1 and ALOS-2 data

The ALOS-2 data were analyzed in this study as complementary results to the Sentinel-1 results. A single SAR data pair was used. The master and slave dates are May 24, 2016 and May 23, 2017, respectively. Due to limited number of SAR images, the conventional DInSAR method was used to obtain the subsidence. A comparison of the Sentinel-1 and ALOS-2 results for similar periods are shown in Figure 4.13.

Figure 4.13 shows that ALOS-2 presents better spatial coverage than Sentinel-1. This is because ALOS-2 uses a longer wavelength than Sentinel-1, namely, the L-band (λ=23.6 cm).

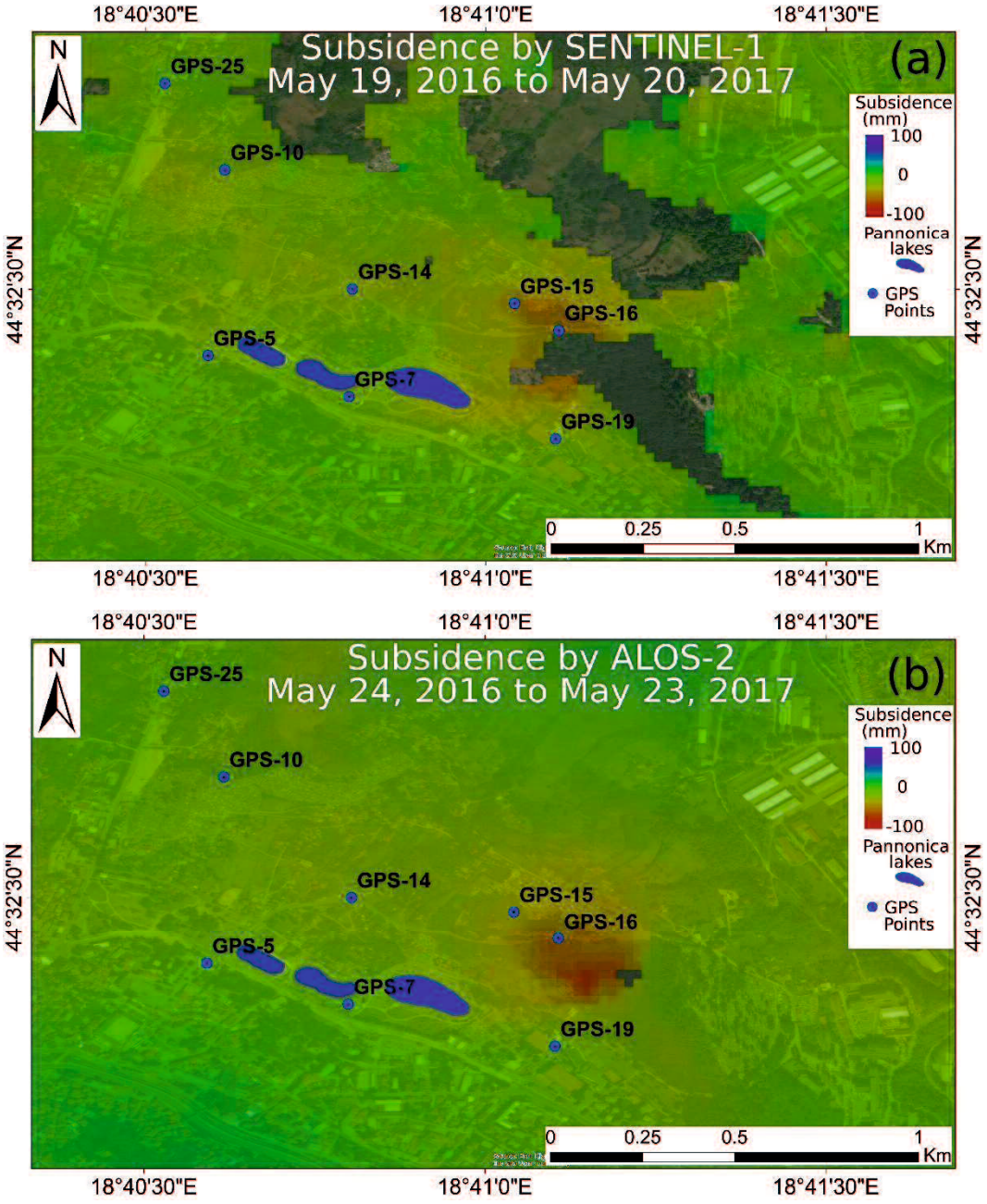

Figure 4.13. Subsidence distribution by Sentinel-1 (from May 19, 2016 to May 20, 2017) and ALOS-2 (May 24, 2016 to May 23, 2017).

A detailed comparison of the subsidence obtained by Sentinel-1 and ALOS-2 at several points is shown by Figure 4.14. In general, the results of Sentinel-1 and ALOS-2 coincide with each other. Only a few points show a large discrepancy (about 10 mm), i.e., GPS-5, GPS-7, and GPS-10.

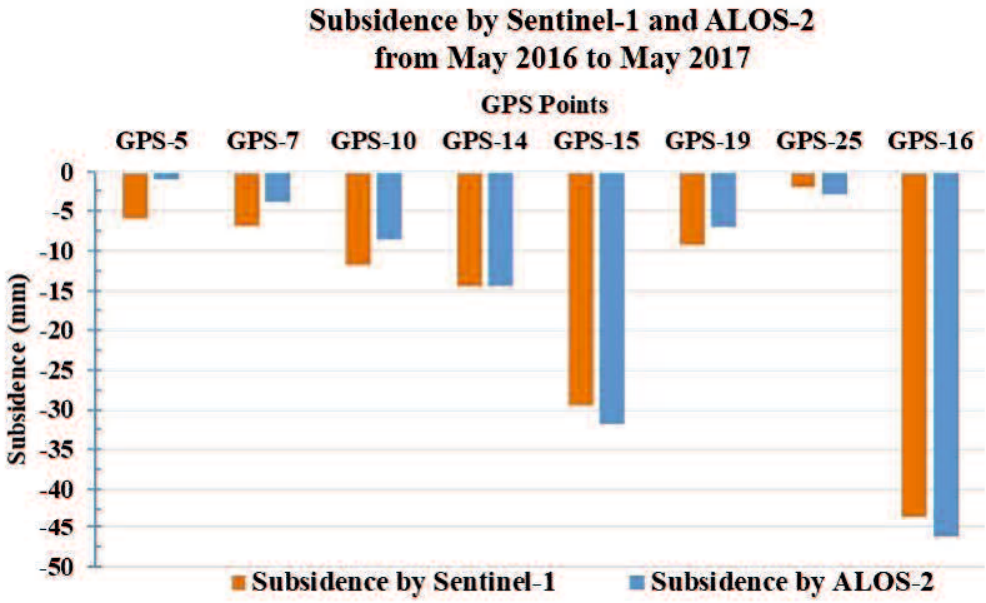

Figure 4.14. Subsidence by Sentinel-1 and ALOS-2 at several points.

4.4 Summary of Chapter 4

This chapter has focused on monitoring the subsidence induced by salt mining activities in Tuzla, Bosnia and Herzegovina by means of SBAS-DInSAR. The conclusions can be given as follows:

1. The validity and applicability of SBAS-DInSAR to monitor the subsidence induced by salt mining activities were evaluated using the former subsidence results (traditional topographic and GPS surveys) and the present real-time kinematic GNSS monitoring system. It was found that SBAS-DInSAR was able to provide reasonable results with good accuracy (the discrepancy between SBAS-DInSAR and GNSS was within 10 mm) and spatial coverage.
2. SBAS-DInSAR detected that the subsidence is still on-going in some areas of Tuzla, especially the northeast part of Pannonica Lake. It was found that the maximum subsidence reached up to -40 mm/year during the period of 2014 to 2019 and that some small subsidence, with a rate of up to -10 mm/year, is continuing to occur in the subsidence area above the salt mine deposit. Thus, it is important to keep monitoring the subsidence in this area.
3. This study has proved that SBAS-DInSAR can be employed as a useful and effective subsidence monitoring tool for Tuzla on into the future.

4. The combination of Sentinel-1 and ALOS-2 data was seen to provide useful results. ALOS-2 provides better spatial coverage than Sentinel-1. However, Sentinel-1 provides better temporal coverage than ALOS-2.

Chapter 5. Discussion on Applicability of DInSAR to Landslide in Small Area

5.1 Introduction

This chapter is focused on a discussion of the advantages and limitations of DInSAR in terms of its practical uses. Two cases are selected for the study, namely, a slope located in a residential area and a slope failure located in a residential area. Each case is explained and discussed in a sequence. The main objective of this chapter is to investigate and evaluate the advantages and limitations of DInSAR in measuring the slope stability and displacements due to a landslide.

The two cases have different characteristics, for example, the slope located in the residential area is unstable and has a very slow displacement velocity, while the slope failure has generated very fast and large displacements. DInSAR is expected to be able to measure and interpret such slope displacement behavior.

5.2 Slope located in residential area (Kostanjek in Zagreb, Croatia)

It is very important that this slope be monitored because it is located very close to a residential area. Many devices have been installed to monitor the displacements in this area, namely, the static GNSS monitoring system, inclinometers, and extensometers (Bečirević et al., 2013; Krkač et al., 2015, 2014). Those measurement devices can be used to investigate and evaluate the DInSAR results. However, in the next chapter, only the GNSS monitoring results will be used to assess the DInSAR results.

5.2.1 Study area, data sources, and methodology

5.2.1.1 Study area

The slope is located in Kostanjek in Zagreb, Croatia (Figure 5.1). On the upper side of the slope, there is a residential area, while on the lower side of the slope, there is an abandoned cement factory. The Kostanjek landslide is an example of a reactivated deep-seated large translational landslide formed in soft rock and hard soil, for example, marls. The displacement velocity of the slope has been changing over the last 50 years, from the landslide activation until today. Recently, the displacement velocity is becoming very slow (Arbanas and Krkac, 2013).

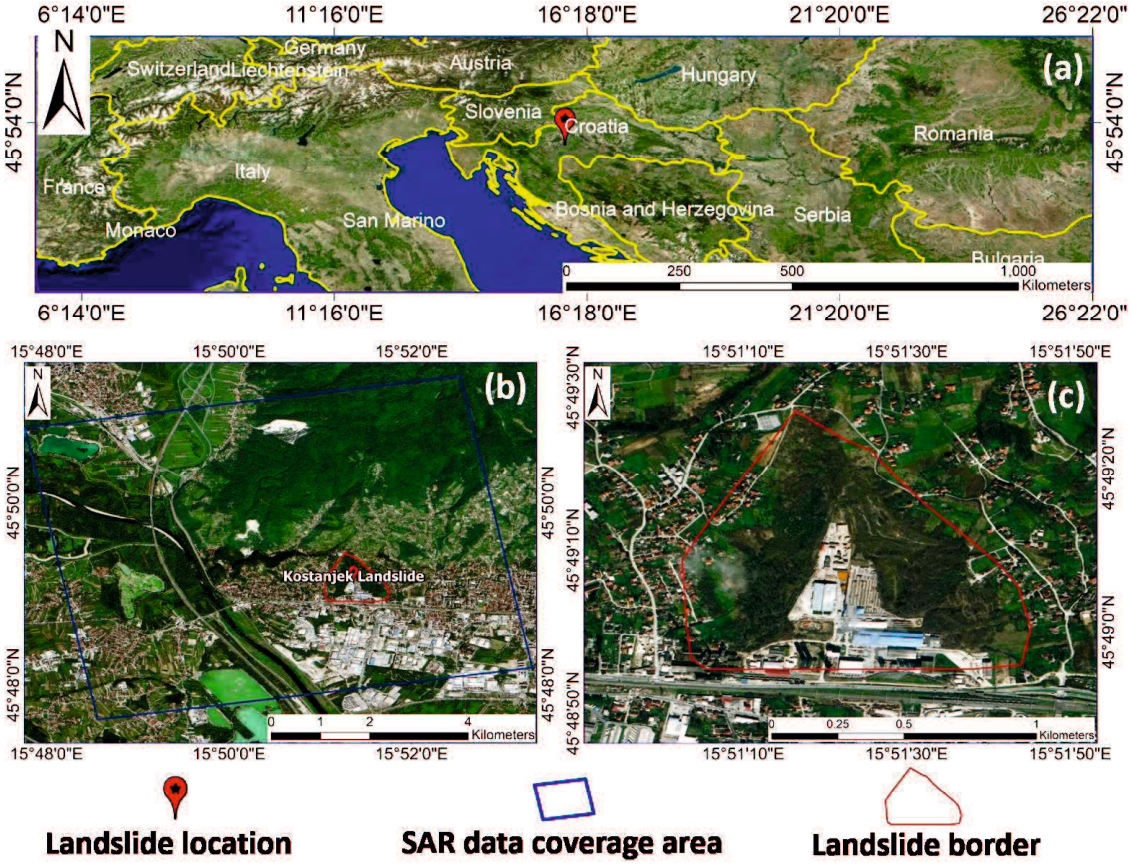

Figure 5.1. Study area: (a) border of Croatia with surrounding countries, (b) sub-area covered by SAR data, and (c) landslide area. The base map and country borders were provided by Google Earth Pro images (November 27, 2018) and GADM Version 3.6, respectively.

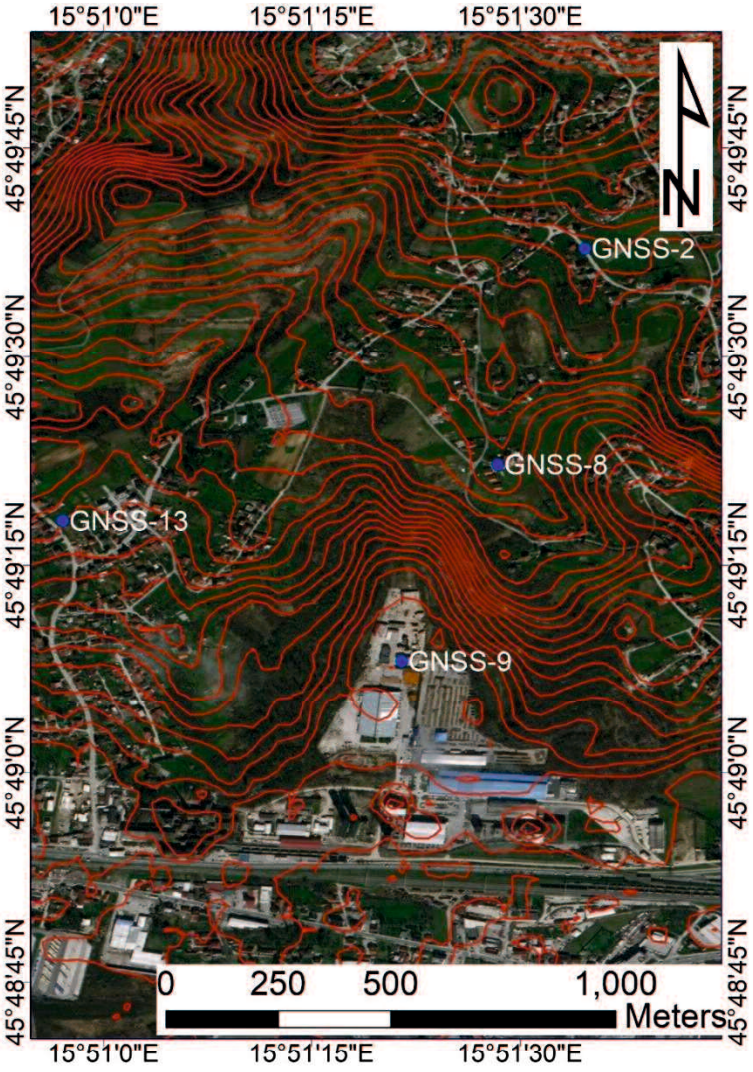

Figure 5.2. Topography of study area represented by contour lines. Vertical interval of contour lines is 5 meters. The base photo and contour lines were provided by Google Earth Pro images (November 27, 2018) and ALOS World 3D 30 meters DEM (AW3D30-DEM 2006-2011), respectively.

The topography of the slope is presented in Figure 5.2 by contour lines. The vertical interval of the contour lines is 5 m. It was generated from ALOS World 3D 30 meters DEM (AW3D30-DEM).

5.2.1.2 Data sources

Table 5.1 shows the information on the SAR data used in this study. SAR data from the Sentinel-1A and -1B satellites, spanning from October 3, 2014 to February 20, 2018, were employed. A detailed list of the SAR data from those years is presented in the Appendix (Table. A - 2).

Table 5.1. SAR data sources used in SBAS-DInSAR analysis for slope stability monitoring near residential area in Kostanjek, Croatia.

Satellite name	Number of SAR images	Period		Orbit direction	Observation mode
		from	to		
Sentinel 1 A and B	145 scenes	October 3, 2014	February 20, 2018	Ascending	Right-looking

5.2.1.3 Methodology (SBAS-DInSAR processing steps and parameter setting)

This study employed the SBAS-DInSAR method explained in sections 2.1.4 and 2.1.5. The processing steps and parameter setting are based on the Envi-SARscape software Version 5.4 (SARMAP, 2016) (see Table 5.2).

Table 5.2. SBAS-DInSAR processing steps and parameter setting for slope stability monitoring near residential area in Kostanjek, Croatia.

Processing step	Parameter name	Parameter value/setting
(1) Connection graph	Maximal perpendicular baseline ($b_\perp$)	150 m
	Maximal temporal baseline (b_t)	24 days
(2) Interferometric process	External DEM	AW3D30-DEM
	Range looks	6 looks
	Azimuth looks	1 looks
	Co-registration with external DEM	True
	Unwrapping method	Minimum cost flow
	Unwrapping threshold	0.2
	Filtering method	Goldstein
(3) Refinement and re-flattening	GCPs file	Geographic GCPs
	Refinement method	Residual phase
	Refinement polynomial degree	3
(4) Inversion: First step	Product coherence threshold	0.4
	Displacement model	Linear model
(5) Inversion: Second step	Product coherence threshold	0.4
	Atmospheric low pass filter window size	1200 m
	Atmospheric high pass filter window size	365 days
(6) Geocoding	Coordinate system projection	Geographic WGS84
	Final pixel size (resolution)	25 x 25 m

By setting the maximum temporal and perpendicular baselines, as shown by Table 5.2, the possible SAR pair combinations in this analysis are presented in Figure 5.3. Several SAR images were removed from the SBAS-DInSAR analysis due to low coherence.

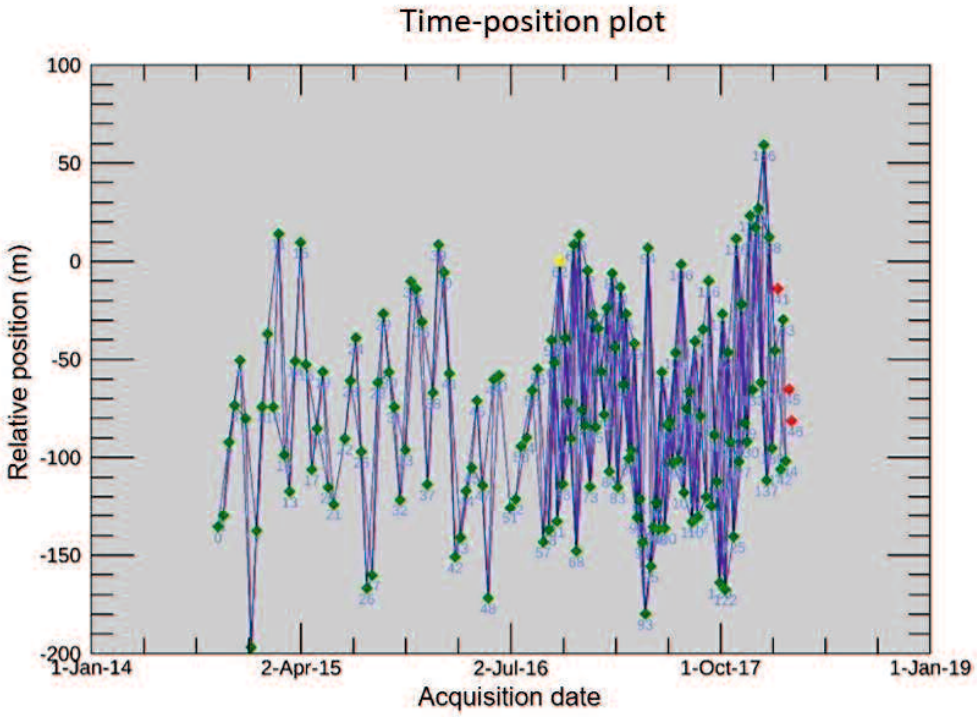

Figure 5.3. SAR pair combinations for SBAS-DInSAR analysis at unstable slope in Kostanjek, Croatia. The green diamonds and red diamonds indicate the SAR pairs used in and removed from this analysis, respectively.

5.2.2 Results and discussion

The LOS displacements of the SBAS-DInSAR analysis are presented in Figure 5.4. The LOS displacement maps were generated every year from the beginning of the SAR data acquisition. They are presented in blue-green-red colors and scaled from 100 mm to – 100 mm. A positive value means that the ground surface moves toward the satellite, whereas a negative value means that the ground surface moves far away from the satellite.

Figure 5.4 shows that the top of the slope is subsiding, while the bottom is moving upward. This indicates that this landslide is a translational slide type. Details on how DInSAR presents the type of landslide was presented well by Schlögel et al. (2015).

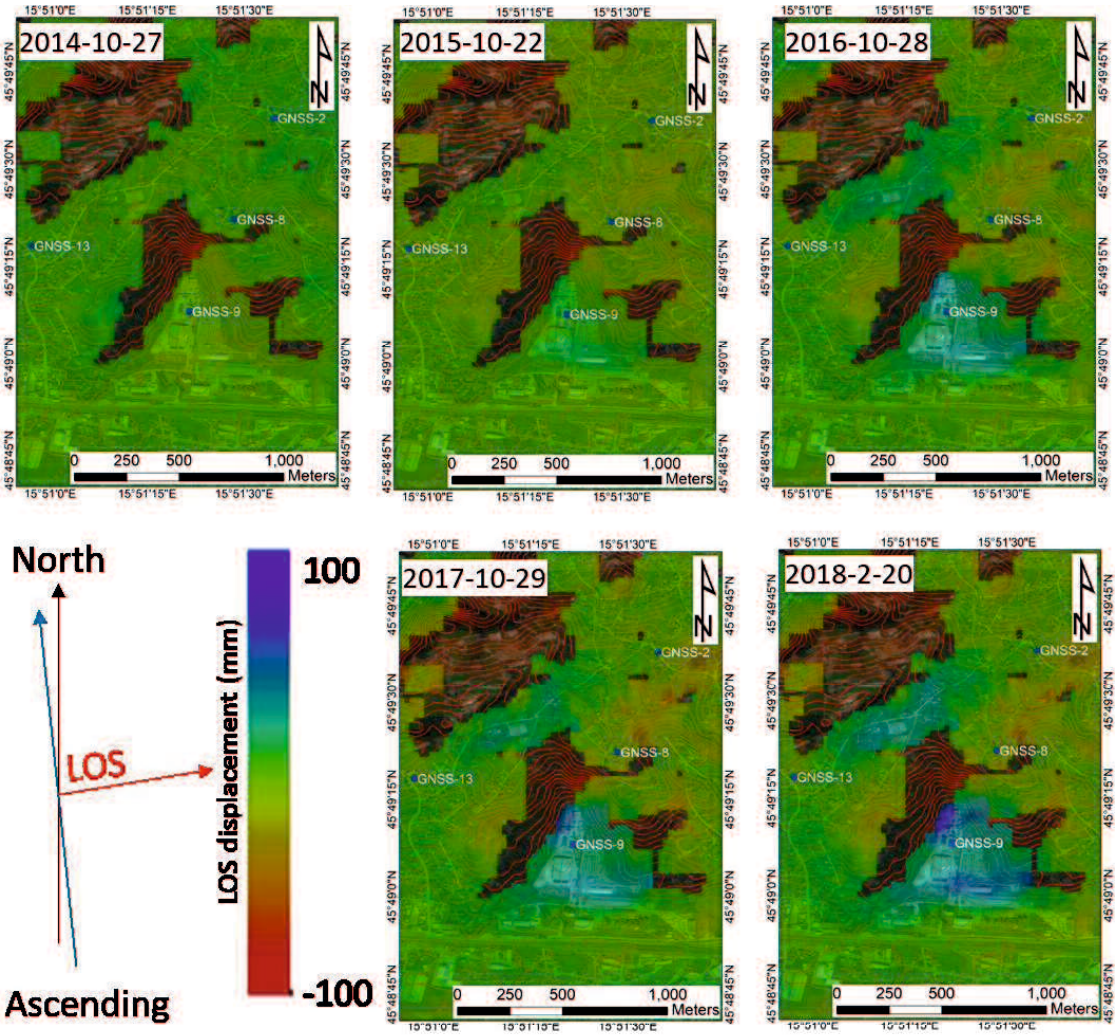

Figure 5.4. Spatial distribution of LOS displacements (every year from October 27, 2014 to February 20, 2018). The base photo and contour line were provided by Google Earth Pro images (November 27, 2018) and ALOS World 3D 30 meters DEM (AW3D30-DEM 20060-2011), respectively.

The temporal evolution of the LOS displacements at several selected points is presented in Figure 5.5. The points were selected based on the locations of the GNSS stations, as shown in Figure 5.6. Those points will be used in a comparison of the displacements between the DInSAR and the GNSS results and will be discussed in the next section.

Figure 5.5 shows that the area at point GNSS 9 is rising, while the areas at the other points are subsiding.

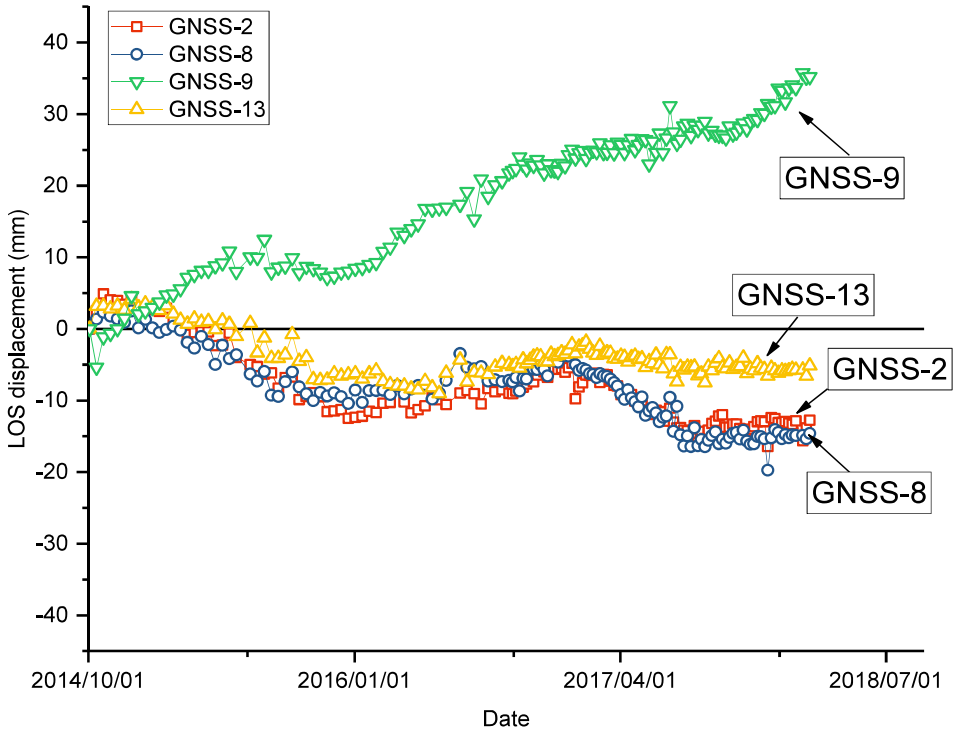

Figure 5.5. Temporal evolution of LOS displacements at several points

The horizontal displacements obtained by the GNSS stations are presented in Figure 5.6. The results were provided by Krkač (2015). It is seen that the displacement vectors are mostly moving in a southern direction. The time-series vertical displacements were also provided by Krkač (2015), as presented in Figure 5.7. Both sets of results show similar displacement directions. DInSAR and GNSS show that the area at GNSS 9 moved upwards. The other three points, GNSS 02, 08, and 13, show subsidence behavior.

The displacements obtained by GNSS seem to be much larger than those obtained by DInSAR. To look at this matter more closely, a comparison of the displacement vectors measured by GNSS and DInSAR is conducted; the results are presented in Figure 5.8. From the results, it can be seen that DInSAR has very low sensitivity in measuring the displacement in the north-south direction. This is one of geometrical limitations of DInSAR.

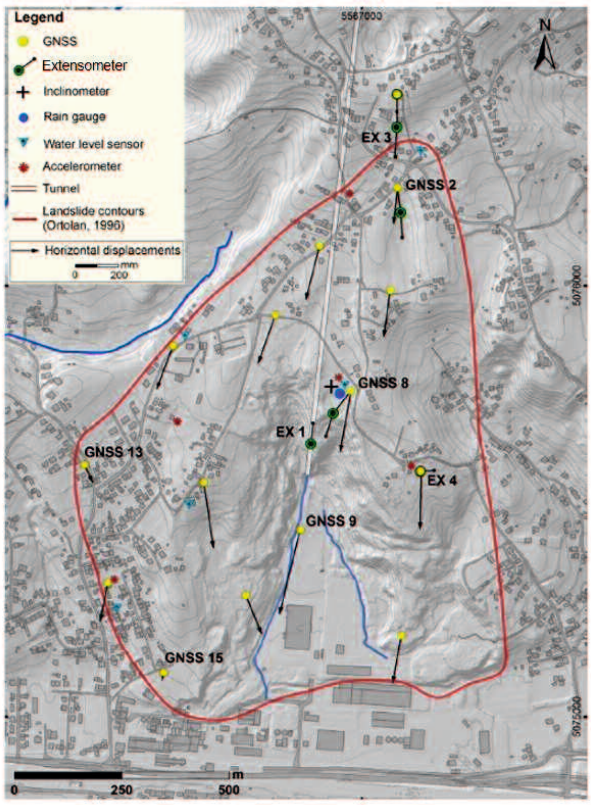

Figure 5.6. Horizontal displacement vector obtained by GPS and extensometers in the period from December 2012 to October 2013 (Krkač et al., 2015).

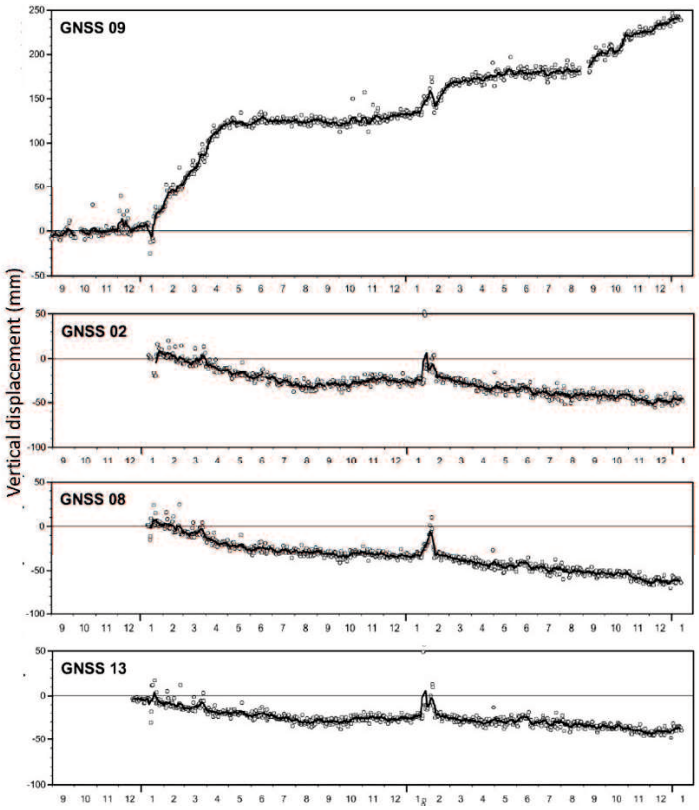

Figure 5.7. Cumulative vertical displacements at GNSS 9, GNSS 2, GNSS 8, and GNSS 13 (Krkač et al., 2015).

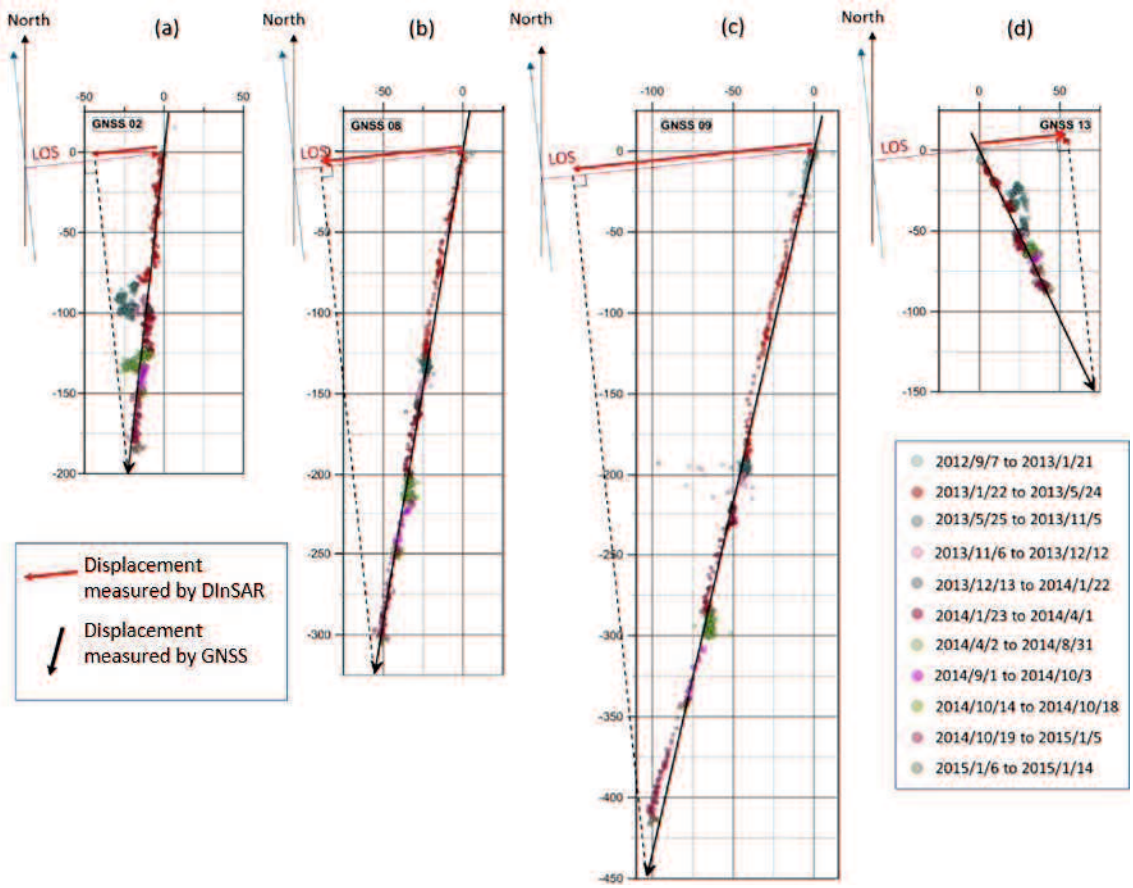

Figure 5.8. Displacement vectors obtained by DInSAR and GNSS: (a) at GNSS 2, (b) at GNSS 8, (c) at GNSS 9 and (d) at GNSS 13. The GNSS results were provided by Krkač (2015).

To prove and validate the DInSAR results, a field survey was conducted in the landslide area. Several photos were taken and are presented in Figure 5.9. Figure 5.9 a shows the location at GNSS 13 and Figures 5.9 b and c present the conditions at GNSS 9.

GNSS 13 is located near a residential area and GNSS 9 is located at the bottom of a slope. It can be clearly seen that the area at GNSS 9 is wavy and some of the ground surface has been uplifted. This coincides well with the DInSAR results.

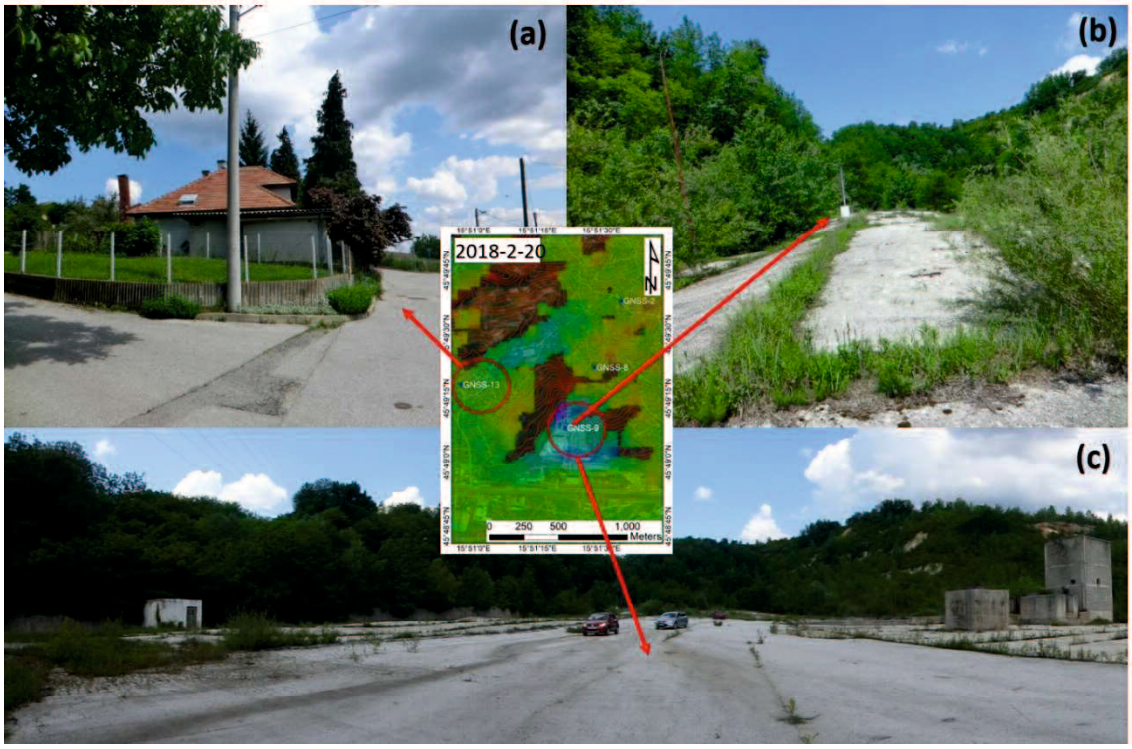

Figure 5.9. Field surveys at GPS-9 and GPS-13.

5.3 Slope failure in residential area (Hrvatska Kostajnica, Croatia)

This slope failure is located in Croatia. The slope collapsed on March 13, 2018. The main factor in this failure was the heavy rainfall and massive amount of snow that melted. SBAS-DInSAR was applied after this landslide event to evaluate whether the method could detect displacements before and after the landslide. If DInSAR can detect such remarkable displacements before a landslide occurs, it will become very important and useful information for developing an early warning system for urban safety.

Unfortunately, no ground measurement data exist for this landslide area. Thus, it is difficult to compare the DInSAR results with other results. However, many photos and videos are available on the conditions after the landslide. Those photos and videos are very useful for seeing the size of the displacements occurring before and after the landslide.

5.3.1 Study area, data sources, and methodology

5.3.1.1 Study area

The location of the landslide area is shown in Figure 5.10. The total landslide and affected area is about 300 m x 300 m. The landslide destroyed several houses and a road. Figure 5.11 presents a photo of the landslide taken on March 14, 2018.

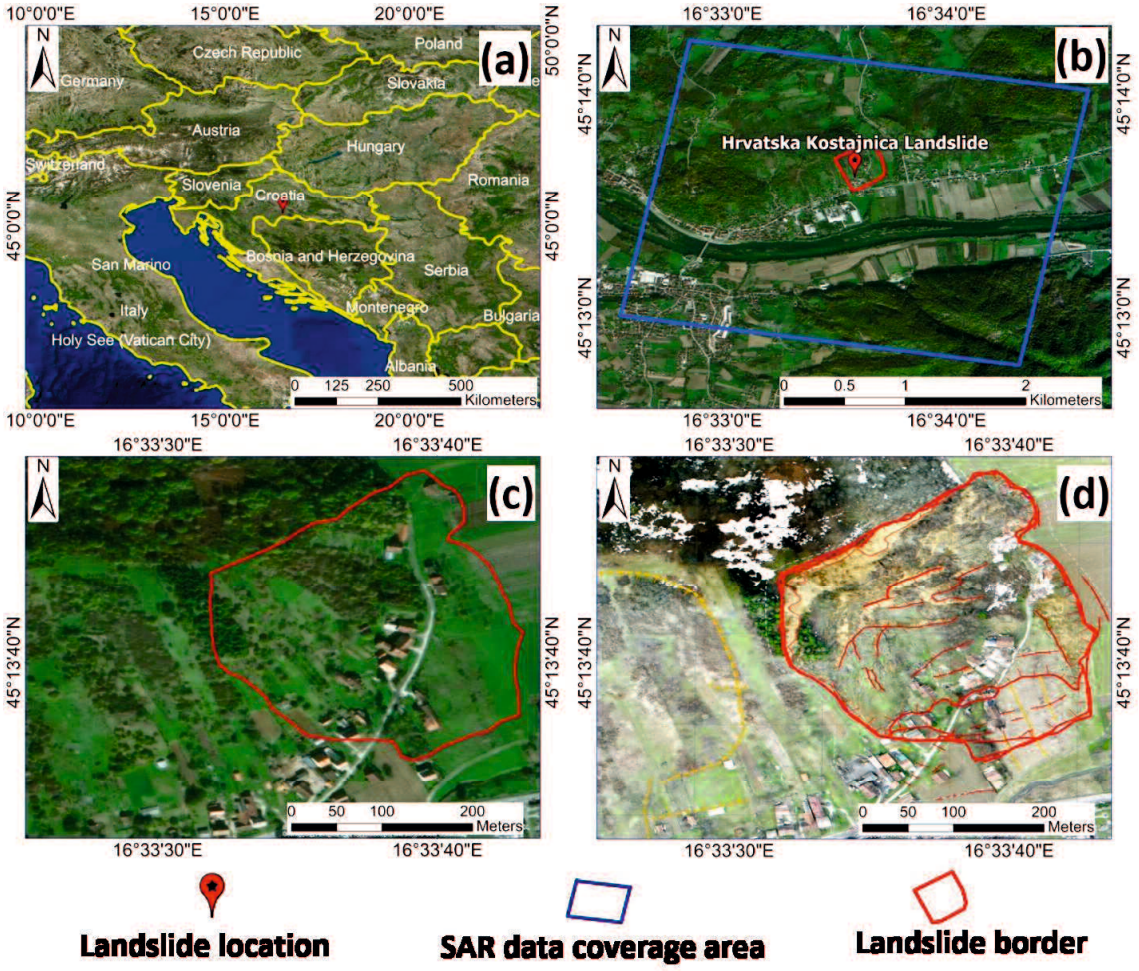

Figure 5.10. Study area: (a) Croatia border with surrounding countries, (b) area covered by SAR data, (c) landslide border - before landslide, and (d) landslide area - after landslide. The base map and country borders were provided by Google Earth Pro images (November 27, 2018) and GADM Version 3.6, respectively. The areal photo after the landslide was provided by László Podolszki (private email, June 13, 2018).

Figure 5.11. Photo of landslide taken on March 13, 2018 at 1:24 PM (local time). Photo source: *https://www.usnews.com/dims4/USNEWS/b3a4b31/2147483647/thumbnail/970x647/quality/85/?url=http%3A%2F%2Fmedia.beam.usnews.com%2F0e%2F2bae74defcc068e9962ad5162d777c%2Fresizes%2F1500%2Fmedia%3Aefd129aaf3f44f22bf961cdc40e52391Croatia_Landslide_54908.jpg*

5.3.1.2 Data sources

The SAR data used in this study are shown in Table 5.3. 150 SAR images from Sentinel-1A and -1B are used in this analysis. The data span from December 1, 2014 to June 13, 2018. The orbit direction and observation mode of those images are in the descending direction and in a right-looking observation mode, respectively.

Table 5.3. SAR data sources used in SBAS-DInSAR analysis for slope failure (landslide) monitoring near residential area in Kotajnica, Croatia.

Satellite name	Number of SAR images	Period		Orbit direction	Observation mode
		from	to		
Sentinel 1 A and B	150 scenes	December 1, 2014	June 13, 2018	Descending	Right-looking

5.3.1.3 Methodology (SBAS-DInSAR processing steps and parameter setting)

This study employed the SBAS-DInSAR method explained in sections 2.1.4 and 2.1.5. The processing steps and parameter setting were based on the Envi-SARscape software

(SARMAP, 2016) (see Table 5.4). The maximum perpendicular baseline and temporal baseline allowed are 150 m and 24 days, respectively. Those thresholds result in the possible SAR data pair combinations given in Figure 5.12. The red diamonds in Figure 5.12 indicate the SAR data removed due to low coherence.

An external DEM (AW3D30-DEM) provided by JAXA was used for the topographic phase removal, the residual phase removal, geographic GCP generation, and the geocoding process.

Table 5.4 . SBAS-DInSAR processing steps and parameter setting for slope failure (landslide) monitoring near residential area in Kotajnica, Croatia.

Processing step	Parameter name	Parameter value/setting
(1) Connection graph	Maximal perpendicular baseline ($b_\perp$)	150 m
	Maximal temporal baseline (b_t)	24 days
(2) Interferometric process	External DEM	AW3D30-DEM
	Range looks	6 looks
	Azimuth looks	1 looks
	Co-registration with external DEM	True
	Unwrapping method	Minimum cost flow
	Unwrapping threshold	0.2
	Filtering method	Goldstein
(3) Refinement and re-flattening	GCPs file	Geographic GCPs
	Refinement method	Residual phase
	Refinement polynomial degree	3
(4) Inversion: First step	Product coherence threshold	0.4
	Displacement model	Linear model
(5) Inversion: Second step	Product coherence threshold	0.4
	Atmospheric low pass filter window size	1200 m
	Atmospheric high pass filter window size	365 days
(6) Geocoding	Coordinate system projection	Geographic WGS84
	Final pixel size (resolution)	25 x 25 m

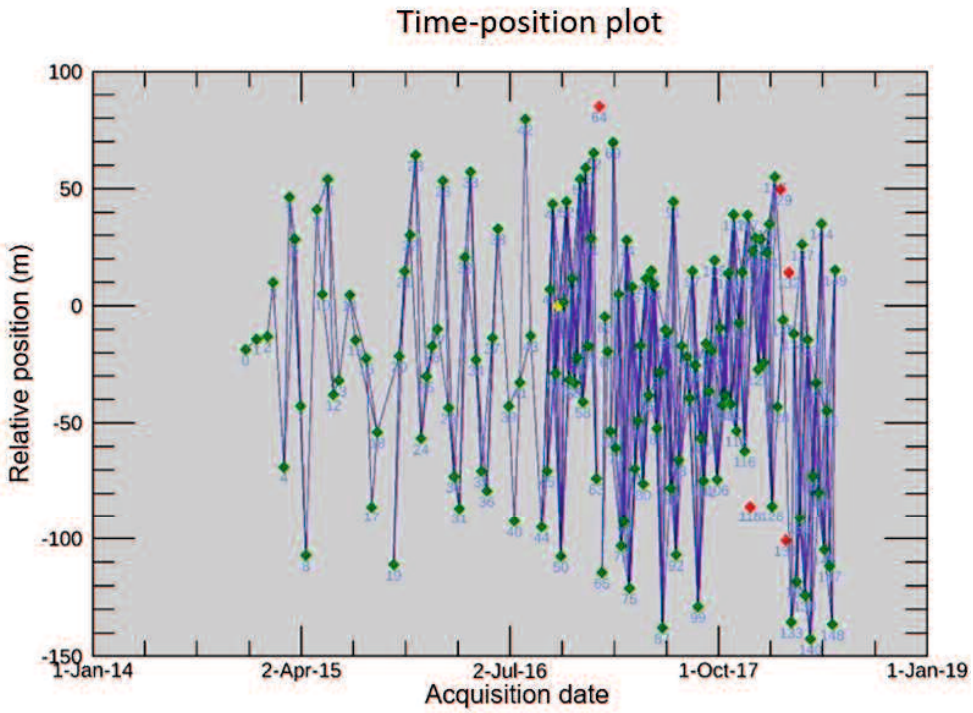

Figure 5.12. SAR pair combinations for SBAS-DInSAR analysis in Kostajnica landslide, Croatia. The green diamonds indicate the SAR pairs used for the analysis, while the red diamonds indicate the SAR pairs removed from the analysis.

5.3.2 Results and discussion

5.3.2.1 Spatial distribution of LOS displacements

Figure 5.13 shows the LOS displacements over the whole area. It should be noted that the LOS displacement map is scaled from -100 mm to 100 mm. The red and yellow polygons indicate the landslide area and the possible unstable area, respectively. The blue polygons indicate the cropping/farming areas.

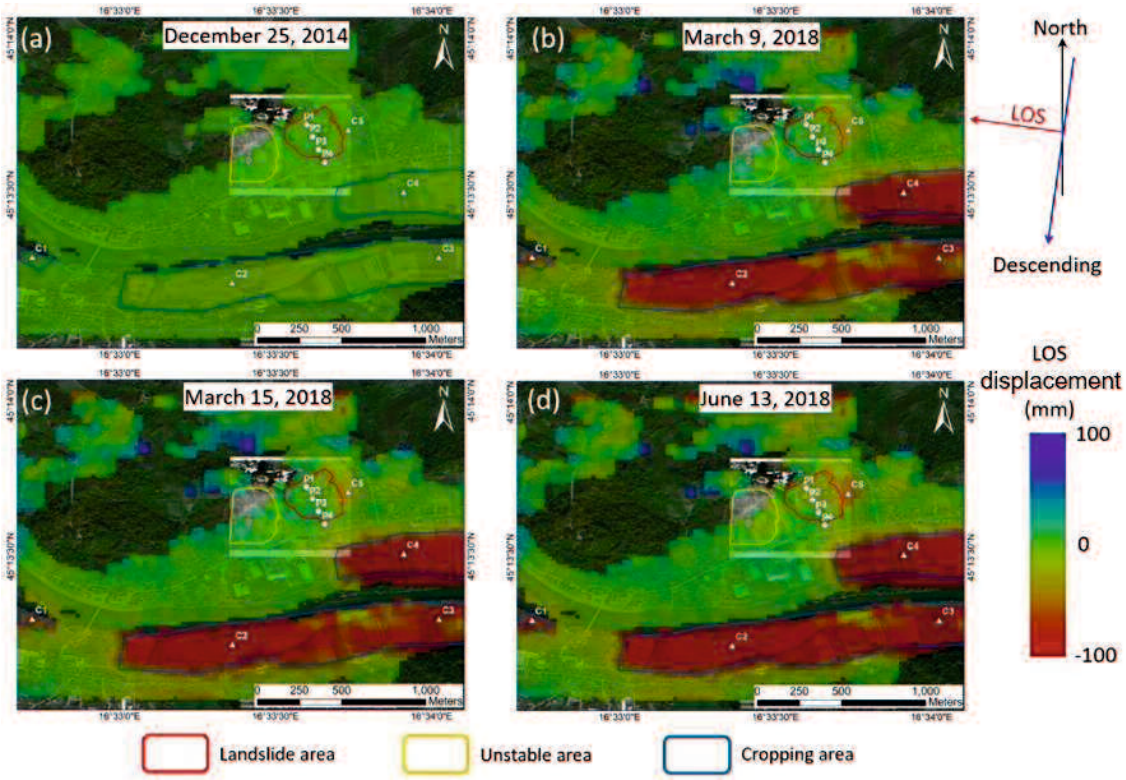

Figure 5.13. LOS displacements at Kostajnica landslide and surrounding area: (a) and (b) before landslide, and (c) and (d) after landslide.

The distribution of LOS displacements focused in the landslide area are shown by Figure 5.14. It is seen that DInSAR could not detect the large displacement induced by the landslide. A displacement, about 2 cm in length, was detected in the center of the landslide area. However, the real displacement was a few meters in length.

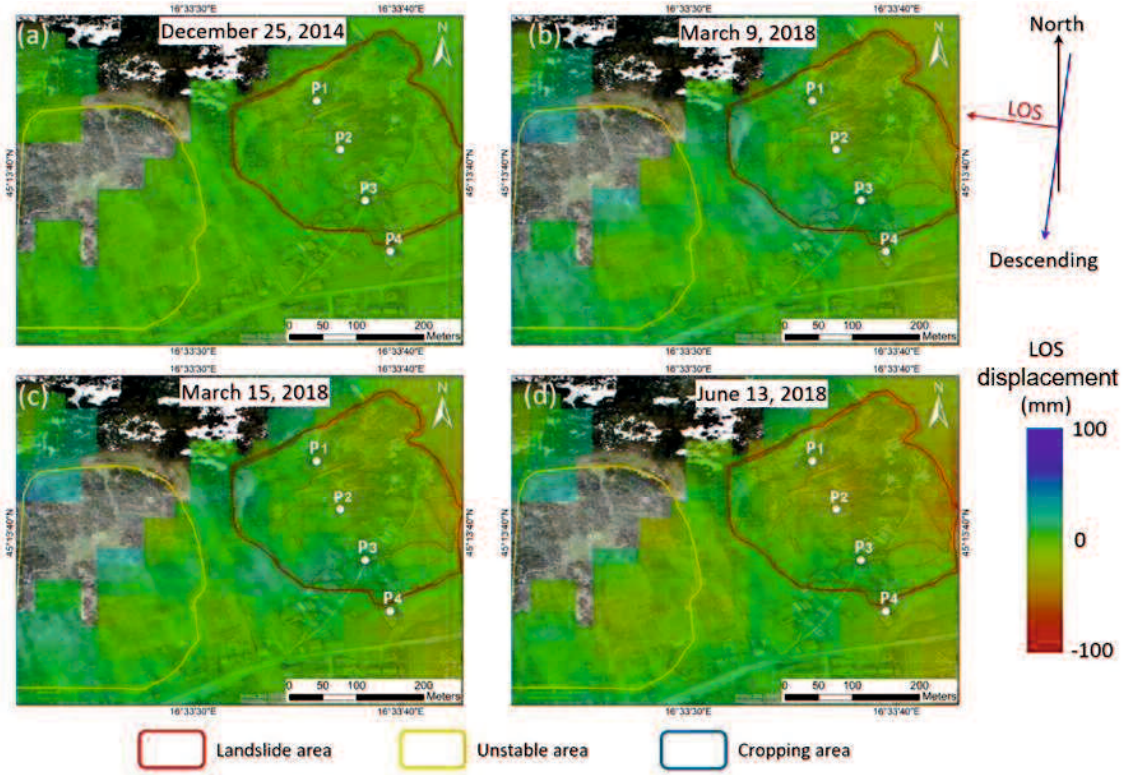

Figure 5.14. LOS displacements at Kostajnica landslide: (a) and (b) before landslide, and (c) and (d) after landslide.

5.3.2.2 Temporal evolution of LOS displacements

To know the temporal evolution of the LOS displacements, several points are selected to extract the LOS displacement values. The points are located inside of the landslide area, as shown in Figure 5.14, i.e., P1-P5. The temporal evolution of the LOS displacements at P1-P5 are shown in Figure 5.15.

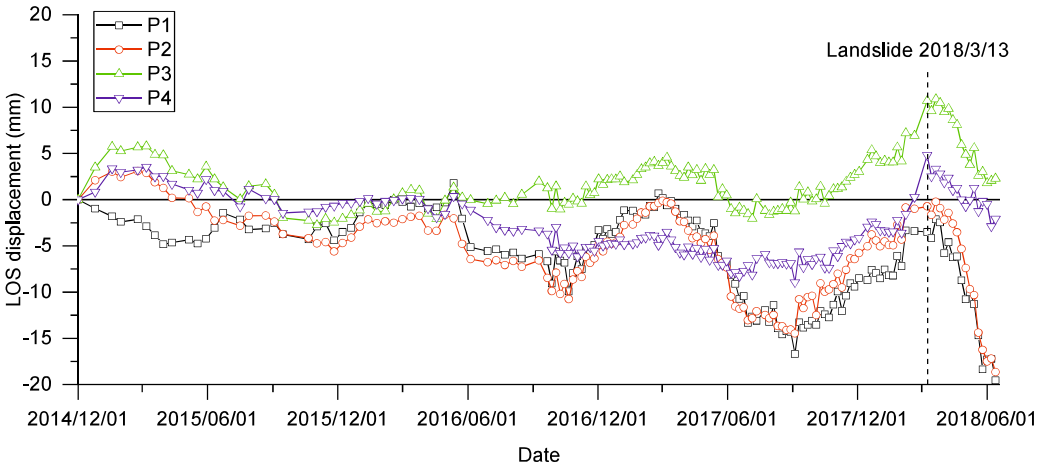

Figure 5.15. Temporal evolution of LOS displacements at P1-P5.

It is seen that no remarkable displacements were detected before the landslide. Even after the landslide, the displacement detected by DInSAR was only a few centimeters in length.

5.3.2.3 Temporal evolution of LOS displacements in cropping/farming area

Large LOS displacements appeared in the cropping/farming areas, as shown in Figure 5.13. To understand the temporal evolution of the LOS displacements in this area, several points are selected, as shown in Figure 5.13, namely, C1-C5.

The results of the temporal evolution at points C1-C5 are shown in Figure 5.16. It seems that all points show LOS displacements with linear behavior. A further investigation will be required to find the reason for these results.

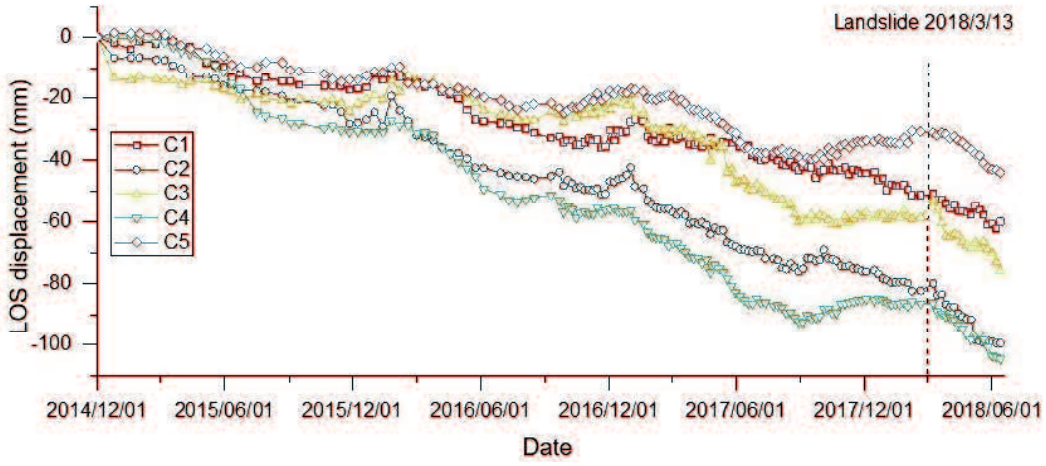

Figure 5.16. Time series of LOS displacements at points C1-C5.

5.4 Summary of Chapter 5

This chapter focused on investigating the advantages and limitations of applying DInSAR for monitoring slope stability and a landslide area. Based on the results and a discussion of this chapter, several conclusions can be made, as follows:

1. DInSAR is applicable for measuring slope displacements with a low displacement velocity and can recognize the different types of slope failures.
2. DInSAR has low sensitivity in measuring slope displacements in the north-south direction. This is due to the geometrical limitations of DInSAR.
3. DInSAR cannot measure large displacements due to landslides. This is because the large displacements exceed the maximum detectable phase change by DInSAR in a single acquisition.

Chapter 6. Discussion on New Concept and Equation for Topographic Mapping by InSAR

6.1 Introduction

As mentioned in section 1.1, the first application of InSAR was for measuring the topography of the Earth's surface. A detailed explanation of the concept and equation for InSAR to measure the topography of the Earth's surface was presented in section 2.1.2. A discussion of the new concept and equation for topographic mapping using SAR data was presented by the author and his colleagues (Tanaka et al., 2020). This approach uses a new mathematical formulation of the geometrical relationship between two satellite positions and two measured points on the ground surface. In this chapter, the new InSAR approach is tested using real satellite data to verify its applicability from a fundamental viewpoint.

6.2 New InSAR approach for topographic mapping

The difference between the conventional approach and the new approach of InSAR is presented by Figure 6.1. The figure shows the conventional and new approaches of InSAR. The conventional InSAR approach uses two SAR satellite positions (*M* and *S*) and observes a point *P* on the ground (Figure 6.1 a). A reference ellipsoid is required in the calculation to estimate the elevation of the ground surface.

On the other hand, the new approach uses two SAR satellite positions (*M* and *S*) and observes two points on the ground, P_1 and P_2 (Figure 6.1 b). It utilizes additional components $\Delta l_{||}$ and $\Delta l_{\perp}$ (see Figure 6.1 b) to estimate the height of P_1 and P_2. The parallel component, $\Delta l_{||}$, can be obtained by $\Delta l_{||} = \frac{c}{2Sr}$, where c is the speed of light and S_r is the SAR sampling rate. *Sr* is given or defined by the SAR satellite operator.

A comparison of the conventional and the new InSAR approaches is presented in Table 6.1.

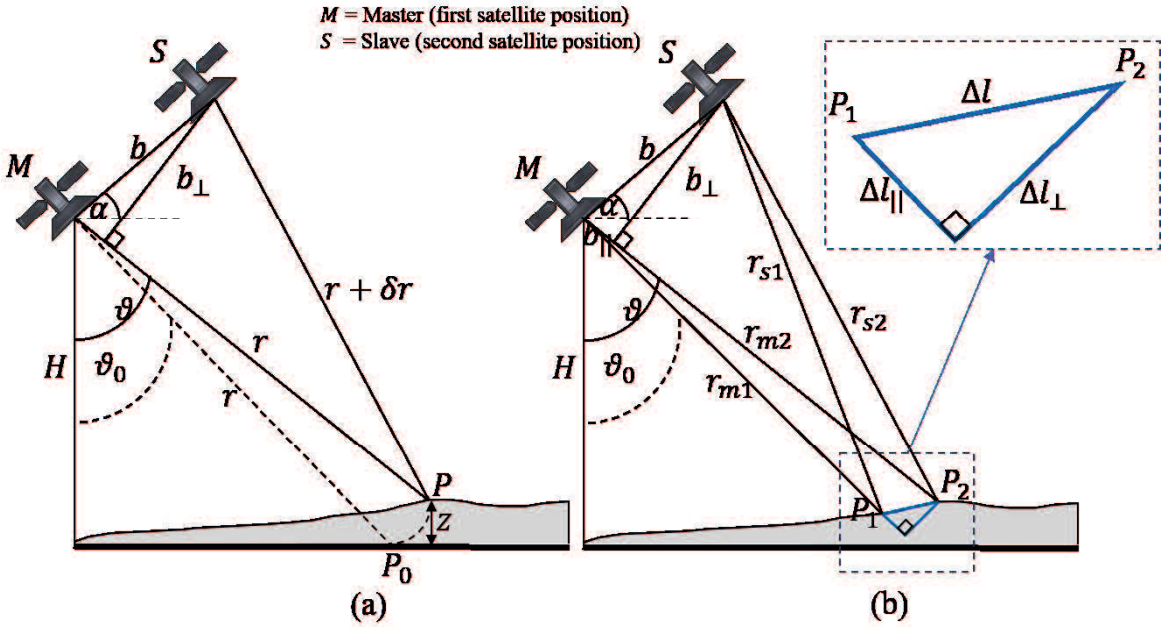

Figure 6.1. Geometrical view of InSAR measurements: (a) conventional InSAR approach and (b) new InSAR approach

Table 6.1. Comparison of conventional InSAR and new InSAR approaches.

Conventional InSAR approach	**New InSAR approach**
Phase difference at point P $\varphi_P = \varphi_{sP} - \varphi_{mP}$ $\varphi_P \simeq -\frac{4\pi}{\lambda} b \sin(\vartheta_0 - \alpha) - \frac{4\pi}{\lambda} \frac{b_\perp}{r \sin\vartheta} z$	Phase difference at P1 $\varphi_{P1} = \varphi_{s1} - \varphi_{m1}$ Phase difference at P2 $\varphi_{P2} = \varphi_{s2} - \varphi_{m2}$
$\varphi_P = \varphi_{flat\ at\ P} + \varphi_{topo\ at\ P}$ $\varphi_{flat\ at\ P} = -\frac{4\pi}{\lambda} b \sin(\vartheta_0 - \alpha)$ $\varphi_{topo\ at\ P} = -\frac{4\pi}{\lambda} \frac{b_\perp}{r \sin\vartheta} z$	Phase difference between P1and P2 $d\Delta\varphi = (\varphi_{s2} - \varphi_{m2}) - (\varphi_{s1} - \varphi_{m1})$
Height estimation at P $Z_P = -\frac{\lambda}{4\pi} \frac{r \sin\vartheta}{b_\perp} (\varphi_P - \varphi_{flat\ at\ P})$	Height estimation at P1 and P2 $\Delta l_{||} = \frac{c}{2Sr}$ $\Delta l_\perp = -\frac{\lambda}{4\pi} \frac{r_{m1}}{b_\perp} d\Delta\varphi - \frac{b_{||}}{b_\perp} \Delta l_{||}$ where Sr is SAR sampling rate. It is determined by the space agency or the operator of the satellite.

6.3 Implementation of new InSAR approach to real SAR satellite data

The new approach is tested using real SAR satellite data provided by the ALOS-PALSAR satellite. The master (primary) data were taken on July 20, 2007 and the slave data (secondary) were taken on September 4, 2007 (Figure 6.2). The master and slave data were cropped from their original sizes and became 1000 pixels in azimuth and 1000 pixels in range.

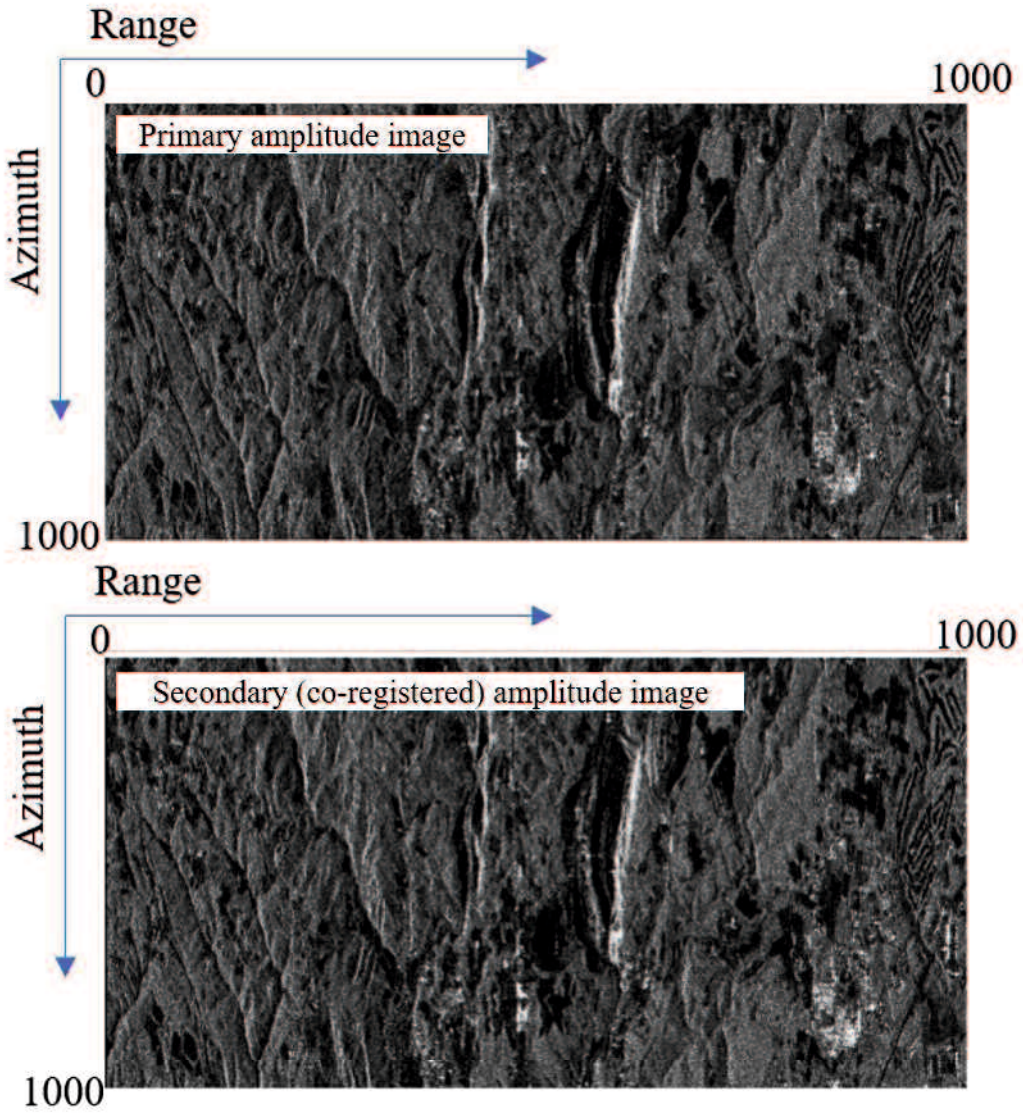

Figure 6.2. Master and slave data provided by ALOS-PALSAR satellite.

The phase difference (interferogram) was calculated from the master and slave data using the Envi-SARscape version 5.3 (https://www.harrisgeospatial.com/Software-Technology/ENVI-SARscape) application software; the results are shown in Figure 6.3. The

multi-look process is applied by 1:4 (1 in range, 4 in azimuth). Then, the interferogram size become 250 pixels in azimuth and 1000 pixels in range (Figure 6.3).

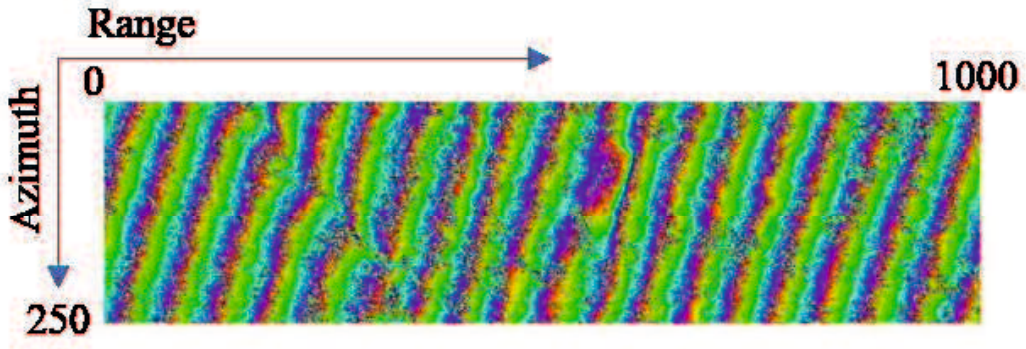

Figure 6.3. Phase difference or interferogram obtained by SAR data in Figure 6.2.

The pixel value (phase difference) in the first line of the interferogram is extracted at pixel numbers 600-900; it is presented in Figure 6.4. The value of the phase difference is in the 2π cycle, between $-\pi$ and $+\pi$.

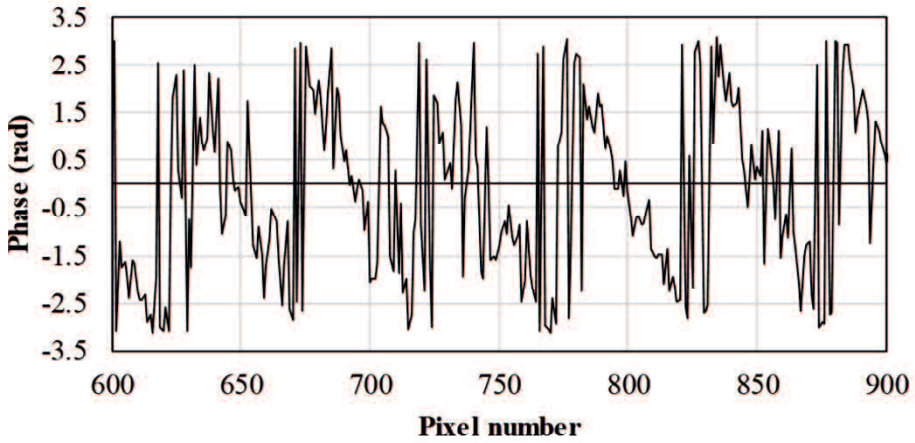

Figure 6.4. Plot of phase differences in Figure 6.3 at first line and at pixel numbers 600-900.

For a manual calculation, several pixel values are selected from Figure 6.4, i.e., pixel numbers 782 to 820, as shown in Figure 6.5. Figure 6.5 shows that there are significant phase differences at some points. Then, a manual calculation is conducted to estimate $\Delta l_{||}$ and $\Delta l_{\perp}$.

The ALOS-PALSAR parameters are given as follows:

Sr = 16 MHz

r_{m1} = 848.3 km

$b_{\perp}$ = 161.9 m

$b_{||}$ = 424.0 m

From those parameters, the parallel component, $\Delta l_{||}$, is equal to 9.36 m and it is constant for all points. The perpendicular component, $\Delta l_{\perp}$, is calculated by $\Delta l_{\perp} = -\frac{\lambda}{4\pi}\frac{r_{m1}}{b_{\perp}} d\Delta\varphi - \frac{b_{||}}{b_{\perp}}\Delta l_{||}$ and the results for all points are presented in Table 6.2.

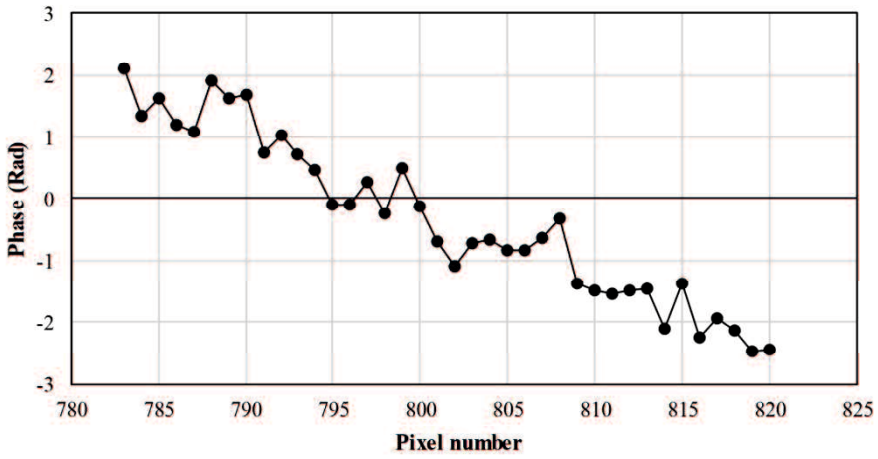

Figure 6.5. Phase differences as shown in Figure 6.4 at pixel numbers 782 to 820.

Table 6.2 shows that the calculated $\Delta l_{\perp}$ from the real SAR data is scattered between one point and the other points. For example, at pixel number 791, the calculated $\Delta l_{\perp}$ is 68.3460 m and just at the next point (at pixel number 792), the calculated $\Delta l_{\perp}$ is -53.0865. Those results are not reasonable, and they are due to the noisy data. However, if the data are observed to have just small noises, the results should be reasonable.

Table 6.2. Plot of ground surface calculated from phase differences in Figure 6.5 at pixel numbers 790-810

Pixel number	$d\psi\ (rad)$	$\Delta d\psi\ (rad)$	$\Delta l_{\perp}$ (m)
790	1.6812		
791	0.7365	-0.9447	68.3460
792	1.0258	0.2893	-53.0865
793	0.7069	-0.3190	6.7687
794	0.4605	-0.2463	-0.3795
795	-0.0990	-0.5595	30.4404
796	-0.1144	-0.0154	-23.1006
797	0.2714	0.3859	-62.5880
798	-0.2525	-0.5239	26.9396
799	0.4938	0.7463	-98.0541
800	-0.1453	-0.6390	38.2648
801	-0.6958	-0.5505	29.5577
802	-1.0845	-0.3887	13.6282
803	-0.7182	0.3663	-60.6661
804	-0.6725	0.0457	-29.1137
805	-0.8496	-0.1771	-7.1873
806	-0.8348	0.0148	-26.0726
807	-0.6525	0.1824	-42.5640
808	-0.3277	0.3248	-56.5811
809	-1.3633	-1.0357	77.2955
810	-1.4988	-0.1355	-11.2844

6.4 Discussions and summary

As shown in Table 6.2, the calculated $\Delta l_{\perp}$ is scattered. However, if the value for $\Delta l_{\perp}$is not scattered or the difference between one point and the next point is relatively small, the ground surface height can be constructed as shown in Figure 6.6. As mentioned before, $\Delta l_{||}$ is constant and $\Delta l_{\perp}$depends on the phase difference between one point and the next point.

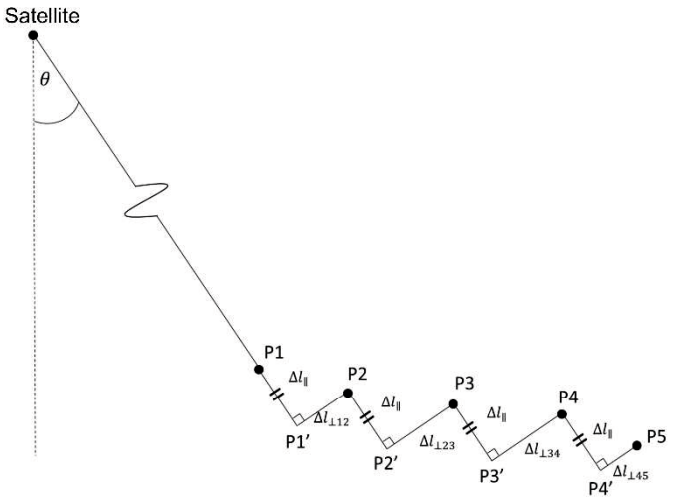

Figure 6.6. Expected surface mapping of new InSAR approach.

A new approach for estimating the topographic height has been presented in this chapter. A comparison of the conventional and the new approaches has been explained. The new approach was tested using ALOS-PALSAR data. Although the results show scatter, it seems that this new approach will provide good results if the input phase difference is smooth (fewer noises).

Chapter 7. Conclusions and Recommendations for Future Research

7.1 General conclusions

DInSAR is a useful tool for monitoring slope stability, such as that in open-pit mine areas. The main characteristic of open-pit mines is the large change in topography that occurs in the mine itself. This change induces errors in the DInSAR results. These errors were investigated in Chapter 3 by utilizing different DEMs in the DInSAR process. One of the solutions for reducing these errors is to use only SAR data pairs with very short perpendicular baseline lengths, i.e., less than 100 m - 150 m (for L-band SAR data). However, the number of SAR data pairs with short perpendicular baselines is very limited. To overcome this limitation, the use of highly accurate DEM data is needed. Employing a DEM that is up-to-date and highly accurate will reduce the errors in the DInSAR results.

SBAS-DInSAR presents a useful performance for monitoring ground subsidence due to underground salt mining, as presented in Chapter 4. It was found that SBAS-DInSAR can be used as a cost-effective tool and sustainable ground subsidence monitoring system, as long as the SAR data are available continuously. The SAR images in the study area in Chapter 4 are available every six days. They are provided by the Sentinel-1A and -1B satellites. Such very short temporal baselines produce very useful monitoring results.

The main limitation of the Sentinel-1 data is the high decorrelation in vegetated areas. This can be solved by combining the SAR data with the longer wavelengths provided by the ALOS-2 data. However, the number of ALOS-2 images is very limited. Typically, only 3-5 SAR images are obtained in a year.

In the case of monitoring slope stability and landslides, as presented in Chapter 5, SBAS-DInSAR can provide important displacement results if the slope displacement is very slow. It is difficult for DInSAR to measure large slope displacements, for example, landslides. This problem occurs when the displacement of the landslide exceed the maximum detectable displacement by the DInSAR system.

A new concept and equation for use with InSAR in estimating the topographic height was presented in Chapter 6.

7.2 Future research

Updating the DEMs is important for improving the accuracy of DInSAR, as mentioned in Chapter 3. The use of an Unmanned Aerial Vehicle (UAV) (like a drone) is promising for

producing accurate DEMs at a low cost in small mining areas. It would be very beneficial to combine tools in order to achieve the required measurement accuracy and meet the needs of practical applications in the mining field.

From the results of Chapter 4, it was indicated that the combination of DInSAR and GPS is useful for monitoring subsidence. Sentinel-1 data are updated at least every six days. It is appropriate to use such slow surface displacements (such as subsidence). In addition, to ensure the accuracy and consistency of DInSAR, the GPS results can be used to validate and assess the DInSAR results. The combination of DInSAR and GPS could be used as a sustainable and economical monitoring system.

Beyond those advantages of the DInSAR method, there is a limitation regarding the sensitivity of DInSAR for measuring horizontal displacements. Since the GPS results show that there are displacements in the horizontal direction, DInSAR should consider the horizontal displacement component. One possibility for solving this problem is to use a combination of ascending and descending SAR data. However, this solution requires the acquisition of both types of data (ascending and descending) and that they be acquired at the same time.

As mentioned in Chapter 5, DInSAR has low sensitivity in measuring horizontal displacements in the north-south direction due to the direction of the satellite orbit. One future solution is to utilize the ascending-descending data and the left-right looking sensor. Unfortunately, Sentinel-1 provides only the right-looking observation mode.

ALOS-2 is one of the SAR satellites which has a left-right looking observation mode. However, ALOS-2 lacks temporal coverage. It is difficult to implement it for continuous monitoring.

The results of the new concept and the equation of InSAR for estimating the topographic height are scattered. This is probably due to the value of the calculated phase differences. If this phase differences are scattered, the results of the new InSAR approach become scattered. Further studies on the phase difference calculation should be conducted.

References

Anh, T. van, Anh, N.D., Khac, D.V., Cuong, T.Q., 2015. Study of subsidence detection by DinSAR and evaluation of some factors to the outcome. Vietnam J. Earth Sci. 37, 344–354.

Arbanas, Z., Krkac, M., 2013. A Comprehensive Landslide Monitoring System: The Kostanjek Landslide, Croatia.

Bakalović, M., 2005. The City on a Grain of Salt (Historical Technical Brochure). Museum East. Bosnia, Tuzla.

Bamler, R., 1997. Digital Terrain Models from radar interferometry. Phogrammetric Week "97" 93–105.

Barla, G., 2018. Numerical modeling of deep-seated landslides interacting with man-made structures. J. Rock Mech. Geotech. Eng. 10, 1020–1036. https://doi.org/10.1016/j.jrmge.2018.08.006

Bečirević, D., Daria, D., Maganić, J., Opatić, K., Županović, L., 2013. Geodetic works in research and development plan in remediation of landslide Kostanjek. Ekscentar 16, 58–61.

Berardino, P., Fornaro, G., Lanari, R., Sansosti, E., 2002. A New Algorithm for Surface Deformation Monitoring Based on Small Baseline Differential SAR Interferograms. IEEE Int. Geosci. Remote Sens. Symp. 40, 2375–2383. https://doi.org/10.1109/TGRS.2002.803792

Bürgmann, R., Paul A. Rosen, Fielding, E.J., 2000. Synthetic aperture radar interferometry to measure Earth's surface topography and its deformation. Annu. Rev. Earth Planet Sci. 28, 169–209. https://doi.org/10.1146/annurev.earth.28.1.169

Čeliković, R., Imamović, E., 2016. Continuous GNSS movement monitoring in the zone of influence of Tuzla salt deposit. Int. Symp. Eng. Geod. 489–498.

Čeliković, R., Imamović, E., Salihović, R., Sušić, A., 2014. Prostorno vremenska analiza vertikalnih pomjeranja terena u Tuzli za period 2008-2012. Proc. GEO-EXPO 2014.

Chang, H.-C., Ge, L., Rizos, C., 2004. Environmental impact assessment of mining subsidence by using spaceborne radar interferometry 1–11.

Chaussard, E., Wdowinski, S., Cabral-Cano, E., Amelung, F., 2014. Land subsidence in central Mexico detected by ALOS InSAR time-series. Remote Sens. Environ. 140, 94–106. https://doi.org/10.1016/j.rse.2013.08.038

Chen, Y., Remy, D., Froger, J.L., Peltier, A., Villeneuve, N., Darrozes, J., Perfettini, H.,

Bonvalot, S., 2017. Long-term ground displacement observations using InSAR and GNSS at Piton de la Fournaise volcano between 2009 and 2014. Remote Sens. Environ. 194, 230–247. https://doi.org/10.1016/j.rse.2017.03.038

Chunxia, Z., Linlin, G., Dongchen, E., Hsingchung, C., 2005. A case study of using external DEM in InSAR DEM generation. Geo-Spatial Inf. Sci. 8, 14–18. https://doi.org/10.1007/BF02826985

Ciantia, M.O., Castellanza, R., Fernandez-Merodo, J.A., 2018. A 3D Numerical Approach to Assess the Temporal Evolution of Settlement Damage to Buildings on Cavities Subject to Weathering. Rock Mech. Rock Eng. 51, 2839–2862. https://doi.org/10.1007/s00603-018-1468-3

Cicić, S., 2002. Geological composition and tectonic terrain of Bosnia and Herzegovina (in Bosnian). Geol. Guideb. through Bosnia Herzegovina.

Costantini, M., 1998. A novel phase unwrapping method based on network programming. IEEE Trans. Geosci. Remote Sens. 36, 813–821. https://doi.org/10.1109/36.673674

Delle Piane, L., Perello, P., Baietto, A., Giorza, A., Musso, A., Gabriele, P., Baster, I., 2016. Mature vs. Active deep-seated landslides: A comparison through two case histories in the alps. Rock Mech. Rock Eng. 49, 2189–2216. https://doi.org/10.1007/s00603-016-0919-y

Du, Z., Ge, L., Li, X., Hay-Man Ng, A., 2016. Subsidence monitoring over the Southern Coalfield, Australia using both L-Band and C-Band SAR time series analysis. Remote Sens. 8, 1–16. https://doi.org/10.3390/rs8070543

Eriksen, H.Ø., Lauknes, T.R., Larsen, Y., Corner, G.D., Bergh, S.G., Dehls, J., Kierulf, H.P., 2017. Visualizing and interpreting surface displacement patterns on unstable slopes using multi-geometry satellite SAR interferometry (2D InSAR). Remote Sens. Environ. 191, 297–312. https://doi.org/10.1016/j.rse.2016.12.024

Ferhatbegovic, Z., 2004. Geological features of the central part of the Tuzla basin (Dissertation). Fac. Min. Geol. Civ. Eng. Univ. Tuzla.

Ferretti, A., 2014. Satellite InSAR Data: Reservoir Monitoring from Space, Education tour series. EAGE Publications.

Ferretti, A., Monti-guarnieri, A., Prati, C., Rocca, F., Massonnet, D. (CNES), 2007. InSAR processing: a mathematical approach (Part C). Insa. Princ. Guidel. SAR Interferom. Process. Interpret. 120–234.

Ferretti, A., Prati, C., Rocca, F., 2000. Nonlinear subsidence rate estimation using permanent scatterers in differential SAR interferometry. IEEE Trans. Geosci. Remote Sens. 38,

2202–2212. https://doi.org/10.1109/36.868878

Fialko, Y., Simons, M., Agnew, D., 2001. The complete (3-D) surface displacement field in the epicentral area of the 1999 Mw7.1 Hector Mine earthquake, California, from space geodetic observations. Geophys. Res. Lett. 28, 3063–3066. https://doi.org/10.1029/2001GL013174

Gaber, A., Darwish, N., Koch, M., 2017. Minimizing the residual topography effect on interferograms to improve DInSAR results: Estimating land subsidence in Port-Said City, Egypt. Remote Sens. 9, 1–22. https://doi.org/10.3390/rs9070752

Goldstein, R., 1995. Atmospheric limitations to repeat-track radar interferometry. Geophys. Res. Lett. 22, 2517–2520. https://doi.org/10.1029/95GL02475

Goldstein, R.M., Werner, C.L., 1998. Radar interferogram filtering for geophysical applications. Geophys. Res. Lett. 25, 4035–4038. https://doi.org/10.1029/1998GL900033

Google Earth, 2011. Google Earth Image at 40°27’10.22"N 141°32’12.62"E (Japan) on April 5, 2011 [WWW Document]. URL https://earth.google.com/ (accessed 1.20.16).

Graham, L.C., 1974. Synthetic Interferometer Radar for Topographic Mapping. Proc. IEEE 62, 763–768. https://doi.org/10.1109/PROC.1974.9516

GSI, 2016. Description of Digital Elevation Models produced by Geospatial Information Authority of Japan (GSI) [WWW Document]. URL https://fgd.gsi.go.jp/otherdata/spec/DEMgaiyo.pdf (accessed 1.20.16).

GSI, 2002. Aerial photo (file name: TO20021X-C2-20) [WWW Document]. URL http://mapps.gsi.go.jp/contentsImageDisplay.do?specificationId=144504&isDetail=true (accessed 1.20.16).

Guido, F.L., Antonellini, M., Picotti, V., 2015. Modeling ground displacement above reservoirs undergoing fluid withdrawal/injection based on an ellipsoidal inhomogeneity model. Int. J. Rock Mech. Min. Sci. 79, 63–69. https://doi.org/10.1016/j.ijrmms.2015.08.010

Hanssen, R.F., 2001. Radar Interferometry: Data Interpretation and Error Analysis. https://doi.org/10.1007/0-306-47633-9

He, L., Wu, L., Liu, S., Wang, Z., Su, C., Liu, S.N., 2015. Mapping two-dimensional deformation field time-series of large slope by coupling DInSAR-SBAS with MAI-SBAS. Remote Sens. 7, 12440–12458. https://doi.org/10.3390/rs70912440

Herrera, G., Tomás, R., Vicente, F., Lopez-Sanchez, J.M., Mallorquí, J.J., Mulas, J., 2010. Mapping ground movements in open pit mining areas using differential SAR

interferometry. Int. J. Rock Mech. Min. Sci. 47, 1114–1125. https://doi.org/10.1016/j.ijrmms.2010.07.006

Hirabayashi, K., Shimizu, N., Ono, M., Masunari, T., Sato, W., Iwasaki, T., 2009. GPS displacement monitoring in large slopes at a limestone quarry and improvements in meteorological measurement errors. Annu. Conf. Gen. Assem. Korean Soc. Rock Mech. 10, 325–333.

Hofmann-Wellenhof, B., Lichtenegger, H., Collins, J., 2001. Global Positioning System: Theory and Practice, 5th ed. Springer, Berlin. https://doi.org/10.1007/978-3-7091-6199-9

Hrvatović, H., 2006. Geological Guidebook through Bosnia and Herzegovina.

Ibreljić, I., Kudumović, F., Ahmetbegović, S., 2007. Economy and ecology of natural resources in Tuzla area (Bosnia and Herzegovina) in the past and future projections. Proc. "Joint Congr. Eur. Reg. Sci. Assoc. ASRDLF (Association Sci. Reg. Lang. Fr.

Janna, C., Castelletto, N., Ferronato, M., Gambolati, G., Teatini, P., 2012. A geomechanical transversely isotropic model of the Po River basin using PSInSAR derived horizontal displacement. Int. J. Rock Mech. Min. Sci. 51, 105–118. https://doi.org/10.1016/j.ijrmms.2012.01.015

Jarosz, A., Zahiri, H., 2007. Integration of InSAR and GIS for Monitoring of Subsidence Induced by Block Caving Mining Integration of InSAR and GIS for Monitoring of Subsidence Induced by Block Caving Mining. Integr. Vlsi J. 13–17. https://doi.org/10.1002/eji.200324259

JAXA-EORC, 2008. ALOS data users handbook revision C. Japan Aerosp. Explor. Agency.

Jo, M.J., Jung, H.S., Yun, S.H., 2017. Retrieving precise three-dimensional deformation on the 2014 M6.0 South Napa Earthquake by Joint Inversion of Multi-Sensor SAR. Sci. Rep. 7, 1–10. https://doi.org/10.1038/s41598-017-06018-0

Jokanovic, B., 1952. Zbornik radova. Teh. Sk. u Beogradu 1, 107–118.

Jovanović, O., 1980. Genesis of Pretortonian Miocene sediments in North Bosnia, between Una and Orina River (in Serbian). Geol. Glas. .

Katzer, F., 1903. Historijsko rasvijanje i danasnje stanje geoloskog proucavanja Bosne I Hercegovine. Glas. muz. BiH. Sep. otis Sarajev.

Klein, E., Vigny, C., Fleitout, L., Grandin, R., Jolivet, R., Rivera, E., Métois, M., 2017. A comprehensive analysis of the Illapel 2015 Mw8.3 earthquake from GPS and InSAR data. Earth Planet. Sci. Lett. 469, 123–134. https://doi.org/10.1016/j.epsl.2017.04.010

Krkač, M., 2015. A phenomenological model of the Kostanjek Landslide monitoring

parameter. Dr. Thesis. University of Zagreb.

Krkač, M., Arbanas, S.M., Arbanas, Ž., Bernat, S., Špehar, K., Watanabe, N., Nagai, O., Sassa, K., Marui, H., Furuya, G., Wang, C., Rubinić, J., Matsunami, K., 2014. Review of monitoring parameters of the Kostanjek Landslide (Zagreb, Croatia). Proc. World Landslide Forum 3 1, 1–7.

Krkač, M., Mihalić Arbanas, S., Arbanas, Ž., Bernat, S., Špehar, K., 2015. The Konstanjek Landslide in the City of Zagreb: Forecasting and Protective. Eng. Geol. Soc. Territ. 5, 715–719. https://doi.org/10.1007/978-3-319-09048-1_139

Lanari, R., Casu, F., Manzo, M., Zeni, G., Berardino, P., Manunta, M., Pepe, A., 2007. An overview of the Small BAseline Subset algorithm: A DInSAR technique for surface deformation analysis. Pure Appl. Geophys. https://doi.org/10.1007/s00024-007-0192-9

Liu, G., Guo, H., Perski, Z., Fan, J., Bai, S., Yan, S., Song, R., 2016a. Monitoring the slope movement of the Shuping landslide in the Three Gorges Reservoir of China, using X-band time series SAR interferometry. Adv. Sp. Res. 57, 2487–2495. https://doi.org/10.1016/j.asr.2016.03.043

Liu, G., Guo, H., Yue, H., Perski, Z., Yan, S., Song, R., Fan, J., Ruan, Z., 2016b. Modified four-pass differential SAR interferometry for estimating mountain glacier surface velocity fields. Remote Sens. Lett. 7, 1–10. https://doi.org/10.1080/2150704X.2015.1094588

Liu, Y., Xu, C., Li, Z., Wen, Y., Forrest, D., 2011. Interseismic slip rate of the Garze-Yushu fault belt in the Tibetan Plateau from C-band InSAR observations between 2003 and 2010. Adv. Sp. Res. 48, 2005–2015. https://doi.org/10.1016/j.asr.2011.08.020

Mancini, F., Stecchi, F., Gabbianelli, G., 2009a. GIS-based assessment of risk due to salt mining activities at Tuzla (Bosnia and Herzegovina). Eng. Geol. 109, 170–182. https://doi.org/10.1016/j.enggeo.2009.06.018

Mancini, F., Stecchi, F., Zanni, M., Gabbianelli, G., 2009b. Monitoring ground subsidence induced by salt mining in the city of Tuzla (Bosnia and Herzegovina). Environ. Geol. 58, 381–389. https://doi.org/10.1007/s00254-008-1597-1

Massonnet, D. (CNES), Feigl, K.L., 1998. Radar interferometry and its application to changes in the Earth's surface. Rev. Geophys. 36, 441–500.

Moghaddam, N.F., Sahebi, M.R., Matkan, A.A., Roostaei, M., 2013. Subsidence rate monitoring of Aghajari oil field based on Differential SAR Interferometry. Adv. Sp. Res. 51, 2285–2296. https://doi.org/10.1016/j.asr.2013.01.023

Mura, J.C., Paradella, W.R., Gama, F.F., Silva, G.G., Galo, M., Camargo, P.O., Silva, A.Q., Silva, A., 2016. Monitoring of non-linear ground movement in an open pit iron mine based on an integration of advanced DInSAR techniques using TerraSAR-X data. Remote Sens. 8. https://doi.org/10.3390/rs8050409

Nakashima, S., Namba, T., Itagaki, S., Soda, H., Iwasaki, T., Shimizu, N., Ono, M., 2014. Tropospheric delay correction of GPS displacement measurements in the presence of large height differences using fixed-point observation. J. MMIJ 130, 479–487.

Nakashima, S., Shimizu, N., Hirabayashi, K., Masunari, T., Iwasaki, T., Ono, M., 2012. Effects of correction of atmospheric delays on GPS displacement measurements in large slopes 128.

Ng, A.H.M., Ge, L., Li, X., 2015. Assessments of land subsidence in the Gippsland Basin of Australia using ALOS PALSAR data. Remote Sens. Environ. 159, 86–101. https://doi.org/10.1016/j.rse.2014.12.003

Nitti, D.O., Hanssen, R.F., Refice, A., Bovenga, F., Nutricato, R., 2011. Impact of DEM-assisted coregistration on high resolution SAR interferometry. IEEE Trans. Geosci. Remote Sens. 49, 1127–1144.

Paradella, W.R., Ferretti, A., Mura, J.C., Colombo, D., Gama, F.F., Tamburini, A., Santos, A.R., Novali, F., Galo, M., Camargo, P.O., Silva, A.Q., Silva, G.G., Silva, A., Gomes, L.L., 2015. Mapping surface deformation in open pit iron mines of Carajás Province (Amazon Region) using an integrated SAR analysis. Eng. Geol. 193, 61–78. https://doi.org/10.1016/j.enggeo.2015.04.015

Pepe, A., Calò, F., 2017. A review of Interferometric Synthetic Aperture RADAR (InSAR) Multi-Track Approaches for the retrieval of Earth's surface displacements. Appl. Sci. 7, 1264. https://doi.org/10.3390/app7121264

Polcari, M., Palano, M., Fernández, J., Samsonov, S. V., Stramondo, S., Zerbini, S., 2016. 3D displacement field retrieved by integrating sentinel-1 InSAR and GPS data: The 2014 south Napa earthquake. Eur. J. Remote Sens. 49, 1–13. https://doi.org/10.5721/EuJRS20164901

Rabus, B., Eineder, M., Roth, A., Bamler, R., 2003. The shuttle radar topography mission - A new class of digital elevation models acquired by spaceborne radar. ISPRS J. Photogramm. Remote Sens. 57, 241–262. https://doi.org/10.1016/S0924-2716(02)00124-7

Rocca, F., Prati, C., Guarnieri, A.M., Ferretti, A., 2000. SAR interferometry and its applications. Surv. Geophys. 21, 159–176. https://doi.org/10.1023/A:1006710731155

Rodriguez, E., Morris, C., Belz, J., 2006. An assessment of the SRTM topographic products. Photogramm. Eng. Remote Sensing 72, 249–260. https://doi.org/0099-1112/06/7203–0249/$3.00/0

Rott, H., Nagler, T., 2006. The contribution of radar interferometry to the assessment of landslide hazards. Adv. Sp. Res. 37, 710–719. https://doi.org/10.1016/j.asr.2005.06.059

Rutqvist, J., Rinaldi, A.P., Cappa, F., Jeanne, P., Mazzoldi, A., Urpi, L., Guglielmi, Y., Vilarrasa, V., 2016. Fault activation and induced seismicity in geological carbon storage – Lessons learned from recent modeling studies. J. Rock Mech. Geotech. Eng. 8, 789–804. https://doi.org/10.1016/j.jrmge.2016.09.001

Sandwell, D.T., Myer, D., Mellors, R., Shimada, M., Brooks, B., Foster, J., 2008. Accuracy and resolution of ALOS interferometry: Vector deformation maps of the father's day intrusion at Kilauea. IEEE Trans. Geosci. Remote Sens. 46, 3524–3534. https://doi.org/10.1109/TGRS.2008.2000634

SARMAP, 2016. SARscape's basic module tutorial 1–42.

Schlögel, R., Doubre, C., Malet, J.P., Masson, F., 2015. Landslide deformation monitoring with ALOS/PALSAR imagery: A D-InSAR geomorphological interpretation method. Geomorphology 231, 314–330. https://doi.org/10.1016/j.geomorph.2014.11.031

Shimizu, N., 1999. Displacement monitoring by using Global Positioning System for assessment of rock slope stability. Proc. 9th Int. Congr. Rock Mech. 1435–8.

Shimizu, N., Nakashima, S., Masunari, T., 2014. ISRM Suggested Method for monitoring rock displacements using the Global Positioning System (GPS). Rock Mech. Rock Eng. 313–328. https://doi.org/10.1007/s00603-013-0521-5

Singhroy, V., Molch, K., 2004. Characterizing and monitoring rockslides from SAR techniques. Adv. Sp. Res. 33, 290–295. https://doi.org/10.1016/S0273-1177(03)00470-8

Soklić, I., 1982. Stratigraphy and age of salt formations in Tuzla (in Croatian). Radevi AnuBiH, Odj. teh. Nauk.

Soklić, I., 1964. Origin and structures of the Tuzla basin. Geol. Glas.

Soklić, I., 1959. Miocene paleogeography and origin of salt deposits in Tuzla (in Croatian) . Geol. Guideb. through Bosnia Herzegovina.

Sowter, A., Warren, M., 2005. Reducing the DEM error effect in differential interferometry. Eur. Sp. Agency, (Special Publ. ESA SP.

Stecchi, F., 2008. Tuzla City (BIH): An example of geohazard induced by salt extraction.

Alma. University of Bologna. https://doi.org/10.6092/unibo/amsdottorato/1033

Stecchi, F., Antonellini, M., Gabbianelli, G., 2009. Curvature analysis as a tool for subsidence-related risk zones identification in the city of Tuzla (BiH). Geomorphology 107, 316–325. https://doi.org/10.1016/j.geomorph.2008.12.013

Stevanović, P., 1977. Geology of the Bosnia and Herzegovina, Book 3 — Cenozoic periods. In: Hrvatović. Geol. Guideb. through Bosnia Herzegovina.

Stramondo, S., Bozzano, F., Marra, F., Wegmuller, U., Cinti, F.R., Moro, M., Saroli, M., 2008. Subsidence induced by urbanisation in the city of Rome detected by advanced InSAR technique and geotechnical investigations. Remote Sens. Environ. 112, 3160–3172. https://doi.org/10.1016/j.rse.2008.03.008

Tachikawa, T., Kaku, M., Iwasaki, A., Gesch, D.B., Oimoen, M.J., Zhang, Z., Danielson, J.J., Krieger, T., Curtis, B., Haase, J., Abrams, M., Carabajal, C., 2011. ASTER Global Digital Elevation Model Version 2 - summary of validation results.

Tadono, T., Ishida, H., Oda, F., Naito, S., Minakawa, K., Iwamoto, H., 2014. Precise global DEM generation by ALOS PRISM. ISPRS Ann. Photogramm. Remote Sens. Spat. Inf. Sci. II–4, 71–76. https://doi.org/10.5194/isprsannals-II-4-71-2014

Takaku, J., Tadono, T., Tsutsui, K., 2014. Generation of high resolution global DSM from ALOS PRISM. Int. Arch. Photogramm. Remote Sens. Spat. Inf. Sci. - ISPRS Arch. 40, 243–248. https://doi.org/10.5194/isprsarchives-XL-4-243-2014

Tanaka, T., Parwata, I.N.S., Yastika, P.E., 2020. SAR Interferometry by Radar Principle (in press). IEEE Geosci. Remote Sens. Mag.

Tao, Q., Gao, T., Liu, G., Wang, Z., 2017. Effect of external digital elevation model on monitoring of mine subsidence by two-pass differential interferometric synthetic aperture radar. J. Appl. Remote Sens. 11, 026037. https://doi.org/10.1117/1.JRS.11.026037

Tari, V., Pamić, J., 1998. Geodynamic evolution of the northern Dinarides and the southern part of the Pannonian Basin. Tectonophysics.

Tizzani, P., Berardino, P., Casu, F., Euillades, P., Manzo, M., Ricciardi, G.P., Zeni, G., Lanari, R., 2007. Surface deformation of Long Valley caldera and Mono Basin, California, investigated with the SBAS-InSAR approach. Remote Sens. Environ. 108, 277–289. https://doi.org/10.1016/j.rse.2006.11.015

Tomić, B., Nurić, A., Nuhanović, S., 2005. Ground subsidence above the flooded “Tušanj” salt mine. Rudarstvo.

Tomiyama, N., Koike, K., Omura, M., 2004. Detection of topographic changes associated

with volcanic activities of Mt. Hossho using D-InSAR. Adv. Sp. Res. 33, 279–283. https://doi.org/10.1016/S0273-1177(03)00483-6

Vervoort, A., Declercq, P.Y., 2018. Upward surface movement above deep coal mines after closure and flooding of underground workings. Int. J. Min. Sci. Technol. 28, 53–59. https://doi.org/10.1016/j.ijmst.2017.11.008

Vrabac, S., 2005. Istorijska geologija. Univ. Tuzla.

Vrabac, S., 1999. Facial and biostratigraphic characteristics of Badenian and Sarmatian in North Bosnia (in Bosnian). Geol. Guideb. through Bosnia Herzegovina.

Wang, H., Liu-Zeng, J., Ng, A.H.-M., Ge, L., Javed, F., Long, F., Aoudia, A., Feng, J., Shao, Z., 2017. Sentinel-1 observations of the 2016 Menyuan earthquake: A buried reverse event linked to the left-lateral Haiyuan fault. Int. J. Appl. Earth Obs. Geoinf. 61, 14–21. https://doi.org/https://doi.org/10.1016/j.jag.2017.04.011

Wempen, J.M., McCarter, M.K., 2017. Comparison of L-band and X-band differential interferometric synthetic aperture radar for mine subsidence monitoring in central Utah. Int. J. Min. Sci. Technol. 27, 159–163. https://doi.org/10.1016/j.ijmst.2016.11.012

Wnuk, K., Wauthier, C., 2017. Surface deformation induced by magmatic processes at Pacaya Volcano, Guatemala revealed by InSAR. J. Volcanol. Geotherm. Res. c. https://doi.org/10.1016/j.jvolgeores.2017.06.024

Woo, K.S., Eberhardt, E., Rabus, B., Stead, D., Vyazmensky, A., 2012. Integration of field characterisation, mine production and InSAR monitoring data to constrain and calibrate 3-D numerical modelling of block caving-induced subsidence. Int. J. Rock Mech. Min. Sci. 53, 166–178. https://doi.org/10.1016/j.ijrmms.2012.05.008

Yastika, P.E., Shimizu, N., Abidin, H.Z., 2019. Monitoring of long-term land subsidence from 2003 to 2017 in coastal area of Semarang, Indonesia by SBAS DInSAR analyses using Envisat-ASAR, ALOS-PALSAR, and Sentinel-1A SAR data. Adv. Sp. Res. 63, 1719–1736. https://doi.org/10.1016/j.asr.2018.11.008

Yuan, W., Wang, Q., Fan, J., Li, H., 2017. Mining land subsidence monitoring using sentinel-1 SAR data. Int. Arch. Photogramm. Remote Sens. Spat. Inf. Sci. - ISPRS Arch. 42, 655–658. https://doi.org/10.5194/isprs-archives-XLII-2-W7-655-2017

Zan, F. De, Guarnieri, A.M., 2006. TOPSAR: Terrain Observation by Progressive Scans. IEEE Trans. Geosci. Remote Sens. 44, 2352–2360. https://doi.org/10.1109/TGRS.2006.873853

Zebker, H.A., Goldstein, R.M., 1986. Topographic mapping from interferometric synthetic aperture radar observations. J. Geophys. Res. 91, 4993.

https://doi.org/10.1029/JB091iB05p04993

Zhang, A., Lu, J., Kim, J.W., 2018. Detecting mining-induced ground deformation and associated hazards using spaceborne InSAR techniques. Geomatics, Nat. Hazards Risk 9, 211–223. https://doi.org/10.1080/19475705.2017.1415229

Zhu, W., Zhang, Q., Ding, X., Zhao, C., Yang, C., Qu, F., Qu, W., 2014. Landslide monitoring by combining of CR-InSAR and GPS techniques. Adv. Sp. Res. 53, 430–439. https://doi.org/10.1016/j.asr.2013.12.003

Zink, M., 2015. TanDEM-x mission status. Int. Arch. Photogramm. Remote Sens. Spat. Inf. Sci. - ISPRS Arch. 40, 1345–1352. https://doi.org/10.5194/isprsarchives-XL-7-W3-1345-2015

Appendix

A.1. List of Sentinel-1 data used in Tuzla, Bosnia and Herzegovina

Table. A - 1. List of Sentinel-1A and -1B SAR data for SBAS-DInSAR analysis in Tuzla, Bosnia and Herzegovina (Track No. 51, Descending direction, data type/format: Interferometric wide (IW) in SLC format).

No.	Platform	Frame number	Acquisition date (YYYY-MM-DD)	No.	Platform	Frame number	Acquisition date (YYYY-MM-DD)	No.	Platform	Frame number	Acquisition date (YYYY-MM-DD)	No.	Platform	Frame number	Acquisition date (YYYY-MM-DD)
1	Sentinel-1A	443	2014-10-09	51	Sentinel-1B	442	2016-10-16	101	Sentinel-1B	445	2017-09-05	151	Sentinel-1B	443	2018-08-07
2	Sentinel-1A	442	2014-10-21	52	Sentinel-1A	445	2016-10-22	102	Sentinel-1B	445	2017-09-17	152	Sentinel-1B	443	2018-08-19
3	Sentinel-1A	442	2014-12-08	53	Sentinel-1B	442	2016-10-28	103	Sentinel-1B	445	2017-09-29	153	Sentinel-1A	443	2018-08-25
4	Sentinel-1A	442	2014-12-20	54	Sentinel-1A	445	2016-11-03	104	Sentinel-1B	445	2017-10-11	154	Sentinel-1B	443	2018-08-31
5	Sentinel-1A	442	2015-01-01	55	Sentinel-1B	443	2016-11-09	105	Sentinel-1A	443	2017-10-17	155	Sentinel-1A	443	2018-09-06
6	Sentinel-1A	442	2015-01-25	56	Sentinel-1A	445	2016-11-15	106	Sentinel-1B	445	2017-10-23	156	Sentinel-1B	443	2018-09-12
7	Sentinel-1A	442	2015-02-06	57	Sentinel-1B	443	2016-11-21	107	Sentinel-1B	445	2017-11-04	157	Sentinel-1A	443	2018-09-18
8	Sentinel-1A	442	2015-02-18	58	Sentinel-1A	445	2016-11-27	108	Sentinel-1A	443	2017-11-10	158	Sentinel-1B	443	2018-09-24
9	Sentinel-1A	442	2015-03-02	59	Sentinel-1B	443	2016-12-03	109	Sentinel-1B	445	2017-11-16	159	Sentinel-1A	443	2018-09-30
10	Sentinel-1A	442	2015-03-14	60	Sentinel-1A	445	2016-12-09	110	Sentinel-1A	443	2017-11-22	160	Sentinel-1B	443	2018-10-06
11	Sentinel-1A	442	2015-03-26	61	Sentinel-1B	443	2016-12-15	111	Sentinel-1B	443	2017-11-28	161	Sentinel-1A	443	2018-10-12
12	Sentinel-1A	442	2015-04-07	62	Sentinel-1A	445	2016-12-21	112	Sentinel-1B	443	2017-12-10	162	Sentinel-1B	443	2018-10-18
13	Sentinel-1A	442	2015-05-01	63	Sentinel-1B	443	2016-12-27	113	Sentinel-1A	443	2017-12-16	163	Sentinel-1A	443	2018-10-24
14	Sentinel-1A	443	2015-05-13	64	Sentinel-1A	445	2017-01-02	114	Sentinel-1B	443	2017-12-22	164	Sentinel-1B	443	2018-10-30
15	Sentinel-1A	442	2015-05-25	65	Sentinel-1B	443	2017-01-08	115	Sentinel-1A	443	2017-12-28	165	Sentinel-1A	443	2018-11-05
16	Sentinel-1A	442	2015-06-06	66	Sentinel-1A	445	2017-01-14	116	Sentinel-1B	443	2018-01-03	166	Sentinel-1B	443	2018-11-11
17	Sentinel-1A	443	2015-06-18	67	Sentinel-1B	443	2017-01-20	117	Sentinel-1A	443	2018-01-09	167	Sentinel-1A	443	2018-11-17
18	Sentinel-1A	442	2015-06-30	68	Sentinel-1B	443	2017-02-01	118	Sentinel-1B	443	2018-01-15	168	Sentinel-1B	442	2018-11-23
19	Sentinel-1A	442	2015-07-12	69	Sentinel-1A	445	2017-02-07	119	Sentinel-1A	443	2018-01-21	169	Sentinel-1A	443	2018-11-29
20	Sentinel-1A	442	2015-07-24	70	Sentinel-1B	443	2017-02-13	120	Sentinel-1B	443	2018-01-27	170	Sentinel-1B	442	2018-12-05
21	Sentinel-1A	442	2015-08-17	71	Sentinel-1A	445	2017-02-19	121	Sentinel-1A	443	2018-02-02	171	Sentinel-1A	443	2018-12-11
22	Sentinel-1A	444	2015-08-29	72	Sentinel-1B	443	2017-02-25	122	Sentinel-1B	443	2018-02-08	172	Sentinel-1B	442	2018-12-17
23	Sentinel-1A	442	2015-09-10	73	Sentinel-1A	445	2017-03-03	123	Sentinel-1A	443	2018-02-14	173	Sentinel-1A	443	2018-12-23
24	Sentinel-1A	442	2015-10-04	74	Sentinel-1B	443	2017-03-09	124	Sentinel-1B	443	2018-02-20	174	Sentinel-1B	442	2018-12-29
25	Sentinel-1A	442	2015-10-16	75	Sentinel-1A	445	2017-03-15	125	Sentinel-1A	443	2018-02-26	175	Sentinel-1A	443	2019-01-04
26	Sentinel-1A	442	2015-10-28	76	Sentinel-1B	443	2017-03-21	126	Sentinel-1B	443	2018-03-04	176	Sentinel-1B	442	2019-01-10
27	Sentinel-1A	445	2015-11-09	77	Sentinel-1A	445	2017-03-27	127	Sentinel-1A	443	2018-03-10	177	Sentinel-1A	443	2019-01-16
28	Sentinel-1A	445	2015-11-21	78	Sentinel-1B	443	2017-04-02	128	Sentinel-1B	443	2018-03-16	178	Sentinel-1B	442	2019-01-22
29	Sentinel-1A	444	2015-12-03	79	Sentinel-1A	445	2017-04-08	129	Sentinel-1A	443	2018-03-22	179	Sentinel-1A	443	2019-01-28
30	Sentinel-1A	445	2015-12-15	80	Sentinel-1A	445	2017-04-20	130	Sentinel-1B	443	2018-03-28	180	Sentinel-1B	442	2019-02-03
31	Sentinel-1A	445	2016-01-08	81	Sentinel-1B	443	2017-04-26	131	Sentinel-1A	446	2018-04-03	181	Sentinel-1A	443	2019-02-09
32	Sentinel-1A	444	2016-01-20	82	Sentinel-1A	445	2017-05-02	132	Sentinel-1B	442	2018-04-09	182	Sentinel-1B	442	2019-02-15
33	Sentinel-1A	446	2016-02-01	83	Sentinel-1B	442	2017-05-08	133	Sentinel-1A	446	2018-04-15	183	Sentinel-1A	443	2019-02-21
34	Sentinel-1A	445	2016-02-25	84	Sentinel-1A	445	2017-05-14	134	Sentinel-1B	442	2018-04-21	184	Sentinel-1B	442	2019-02-27
35	Sentinel-1A	446	2016-03-20	85	Sentinel-1B	442	2017-05-20	135	Sentinel-1A	446	2018-04-27	185	Sentinel-1A	443	2019-03-05
36	Sentinel-1A	445	2016-04-13	86	Sentinel-1A	443	2017-05-26	136	Sentinel-1B	442	2018-05-03	186	Sentinel-1B	442	2019-03-11
37	Sentinel-1A	445	2016-04-25	87	Sentinel-1B	445	2017-06-01	137	Sentinel-1A	446	2018-05-09	187	Sentinel-1A	443	2019-03-17
38	Sentinel-1A	445	2016-05-19	88	Sentinel-1A	443	2017-06-07	138	Sentinel-1B	442	2018-05-15	188	Sentinel-1B	442	2019-03-23
39	Sentinel-1A	443	2016-05-31	89	Sentinel-1B	445	2017-06-13	139	Sentinel-1A	446	2018-05-21	189	Sentinel-1A	443	2019-03-29
40	Sentinel-1A	445	2016-06-12	90	Sentinel-1A	443	2017-06-19	140	Sentinel-1B	446	2018-05-27	190	Sentinel-1B	442	2019-04-04
41	Sentinel-1A	445	2016-07-06	91	Sentinel-1B	445	2017-06-25	141	Sentinel-1B	443	2018-06-08	191	Sentinel-1A	443	2019-04-10
42	Sentinel-1A	443	2016-07-18	92	Sentinel-1A	443	2017-07-01	142	Sentinel-1A	443	2018-06-14	192	Sentinel-1B	442	2019-04-16
43	Sentinel-1A	445	2016-07-30	93	Sentinel-1A	443	2017-07-13	143	Sentinel-1B	443	2018-06-20	193	Sentinel-1A	443	2019-04-22
44	Sentinel-1A	443	2016-08-11	94	Sentinel-1B	445	2017-07-19	144	Sentinel-1A	443	2018-06-26	194	Sentinel-1B	442	2019-04-28
45	Sentinel-1A	445	2016-08-23	95	Sentinel-1A	443	2017-07-25	145	Sentinel-1B	443	2018-07-02	195	Sentinel-1A	443	2019-05-04
46	Sentinel-1A	445	2016-09-04	96	Sentinel-1B	445	2017-07-31	146	Sentinel-1B	443	2018-07-08	196	Sentinel-1B	442	2019-05-10
47	Sentinel-1A	445	2016-09-16	97	Sentinel-1A	443	2017-08-06	147	Sentinel-1A	443	2018-07-14	197	Sentinel-1A	443	2019-05-16
48	Sentinel-1A	445	2016-09-28	98	Sentinel-1B	445	2017-08-12	148	Sentinel-1B	443	2018-07-20	198	Sentinel-1B	443	2019-05-22
49	Sentinel-1B	442	2016-10-04	99	Sentinel-1B	445	2017-08-24	149	Sentinel-1A	443	2018-07-26	199	Sentinel-1A	443	2019-05-28
50	Sentinel-1A	445	2016-10-10	100	Sentinel-1A	443	2017-08-30	150	Sentinel-1B	443	2018-08-01				

A.2. List of Sentinel-1 data used in Kostanjek in Zagreb, Croatia

Table. A - 2. List of Sentinel-1A and -1B SAR data for SBAS-DInSAR analysis in Kostanjek in Zagreb, Croatia (Track No. 146, Ascending direction, data type/format: Interferometric wide (IW) in SLC format).

No.	Platform	Frame number	Acquisition date (YYYY-MM-DD)	No.	Platform	Frame number	Acquisition date (YYYY-MM-DD)	No.	Platform	Frame number	Acquisition date (YYYY-MM-DD)	No.	Platform	Frame number	Acquisition date (YYYY-MM-DD)
1	Sentinel-1A	148	2014-10-03	41	Sentinel-1A	145	2016-02-07	81	Sentinel-1A	147	2017-02-01	121	Sentinel-1A	148	2017-09-29
2	Sentinel-1A	148	2014-10-15	42	Sentinel-1A	143	2016-02-19	82	Sentinel-1B	144	2017-02-07	122	Sentinel-1B	143	2017-10-05
3	Sentinel-1A	148	2014-10-27	43	Sentinel-1A	145	2016-03-02	83	Sentinel-1A	147	2017-02-13	123	Sentinel-1A	148	2017-10-11
4	Sentinel-1A	148	2014-11-08	44	Sentinel-1A	145	2016-03-14	84	Sentinel-1B	144	2017-02-19	124	Sentinel-1B	143	2017-10-17
5	Sentinel-1A	148	2014-11-20	45	Sentinel-1A	145	2016-03-26	85	Sentinel-1A	147	2017-02-25	125	Sentinel-1A	148	2017-10-23
6	Sentinel-1A	148	2014-12-02	46	Sentinel-1A	144	2016-04-07	86	Sentinel-1B	144	2017-03-03	126	Sentinel-1B	143	2017-10-29
7	Sentinel-1A	148	2014-12-14	47	Sentinel-1A	145	2016-04-19	87	Sentinel-1A	147	2017-03-09	127	Sentinel-1A	148	2017-11-04
8	Sentinel-1A	148	2014-12-26	48	Sentinel-1A	144	2016-05-01	88	Sentinel-1B	144	2017-03-15	128	Sentinel-1B	143	2017-11-10
9	Sentinel-1A	148	2015-01-07	49	Sentinel-1A	145	2016-05-13	89	Sentinel-1A	147	2017-03-21	129	Sentinel-1A	148	2017-11-16
10	Sentinel-1A	148	2015-01-19	50	Sentinel-1A	145	2016-05-25	90	Sentinel-1B	144	2017-03-27	130	Sentinel-1B	143	2017-11-22
11	Sentinel-1A	148	2015-01-31	51	Sentinel-1A	148	2016-06-06	91	Sentinel-1A	147	2017-04-02	131	Sentinel-1A	148	2017-11-28
12	Sentinel-1A	148	2015-02-12	52	Sentinel-1A	147	2016-06-30	92	Sentinel-1B	144	2017-04-08	132	Sentinel-1B	143	2017-12-04
13	Sentinel-1A	148	2015-02-24	53	Sentinel-1A	147	2016-07-12	93	Sentinel-1A	147	2017-04-14	133	Sentinel-1A	148	2017-12-10
14	Sentinel-1A	148	2015-03-08	54	Sentinel-1A	147	2016-07-24	94	Sentinel-1B	144	2017-04-20	134	Sentinel-1B	143	2017-12-16
15	Sentinel-1A	148	2015-03-20	55	Sentinel-1A	147	2016-08-05	95	Sentinel-1A	147	2017-04-26	135	Sentinel-1A	148	2017-12-22
16	Sentinel-1A	148	2015-04-01	56	Sentinel-1A	147	2016-08-17	96	Sentinel-1B	144	2017-05-02	136	Sentinel-1B	143	2017-12-28
17	Sentinel-1A	148	2015-04-13	57	Sentinel-1A	146	2016-08-29	97	Sentinel-1A	147	2017-05-08	137	Sentinel-1A	148	2018-01-03
18	Sentinel-1A	148	2015-04-25	58	Sentinel-1A	147	2016-09-10	98	Sentinel-1B	144	2017-05-14	138	Sentinel-1B	143	2018-01-09
19	Sentinel-1A	145	2015-05-07	59	Sentinel-1A	147	2016-09-22	99	Sentinel-1A	147	2017-05-20	139	Sentinel-1A	148	2018-01-15
20	Sentinel-1A	148	2015-05-19	60	Sentinel-1B	144	2016-09-28	100	Sentinel-1B	144	2017-05-26	140	Sentinel-1B	143	2018-01-21
21	Sentinel-1A	148	2015-05-31	61	Sentinel-1A	147	2016-10-04	101	Sentinel-1A	148	2017-06-01	141	Sentinel-1A	148	2018-01-27
22	Sentinel-1A	148	2015-06-12	62	Sentinel-1B	144	2016-10-10	102	Sentinel-1B	148	2017-06-07	142	Sentinel-1B	143	2018-02-02
23	Sentinel-1A	148	2015-07-06	63	Sentinel-1A	147	2016-10-16	103	Sentinel-1A	148	2017-06-13	143	Sentinel-1A	148	2018-02-08
24	Sentinel-1A	148	2015-07-18	64	Sentinel-1B	143	2016-10-22	104	Sentinel-1B	143	2017-06-19	144	Sentinel-1B	143	2018-02-14
25	Sentinel-1A	148	2015-07-30	65	Sentinel-1A	147	2016-10-28	105	Sentinel-1A	148	2017-06-25	145	Sentinel-1A	148	2018-02-20
26	Sentinel-1A	147	2015-08-11	66	Sentinel-1B	143	2016-11-03	106	Sentinel-1B	143	2017-07-01				
27	Sentinel-1A	147	2015-08-23	67	Sentinel-1A	147	2016-11-09	107	Sentinel-1A	148	2017-07-07				
28	Sentinel-1A	147	2015-09-04	68	Sentinel-1B	143	2016-11-15	108	Sentinel-1B	143	2017-07-13				
29	Sentinel-1A	147	2015-09-16	69	Sentinel-1A	147	2016-11-21	109	Sentinel-1A	148	2017-07-19				
30	Sentinel-1A	147	2015-09-28	70	Sentinel-1B	143	2016-11-27	110	Sentinel-1B	148	2017-07-25				
31	Sentinel-1A	148	2015-10-10	71	Sentinel-1A	147	2016-12-03	111	Sentinel-1A	148	2017-07-31				
32	Sentinel-1A	147	2015-10-22	72	Sentinel-1B	143	2016-12-09	112	Sentinel-1B	148	2017-08-06				
33	Sentinel-1A	147	2015-11-03	73	Sentinel-1A	147	2016-12-15	113	Sentinel-1A	148	2017-08-12				
34	Sentinel-1A	144	2015-11-15	74	Sentinel-1B	144	2016-12-21	114	Sentinel-1B	148	2017-08-18				
35	Sentinel-1A	145	2015-11-27	75	Sentinel-1A	147	2016-12-27	115	Sentinel-1A	148	2017-08-24				
36	Sentinel-1A	144	2015-12-09	76	Sentinel-1B	144	2017-01-02	116	Sentinel-1B	143	2017-08-30				
37	Sentinel-1A	145	2015-12-21	77	Sentinel-1A	147	2017-01-08	117	Sentinel-1A	148	2017-09-05				
38	Sentinel-1A	144	2016-01-02	78	Sentinel-1B	144	2017-01-14	118	Sentinel-1B	143	2017-09-11				
39	Sentinel-1A	145	2016-01-14	79	Sentinel-1A	147	2017-01-20	119	Sentinel-1A	148	2017-09-17				
40	Sentinel-1A	144	2016-01-26	80	Sentinel-1B	144	2017-01-26	120	Sentinel-1B	143	2017-09-23				

A.3. List of Sentinel-1 used in Hrvatska Kostajnica, Croatia

Table. A - 3. List of Sentinel-1A and -1B SAR data for SBAS-DInSAR analysis in Hrvatska Kostajnica, Croatia (Track No. 24, Descending direction, data type/format: Interferometric wide (IW) in SLC format).

No.	Platform	Frame number	Acquisition date (YYYY-MM-DD)	No.	Platform	Frame number	Acquisition date (YYYY-MM-DD)	No.	Platform	Frame number	Acquisition date (YYYY-MM-DD)	No.	Platform	Frame number	Acquisition date (YYYY-MM-DD)
1	Sentinel-1A	442	2014-10-14	41	Sentinel-1A	442	2016-06-05	81	Sentinel-1A	440	2017-04-13	121	Sentinel-1A	442	2017-12-21
2	Sentinel-1A	442	2014-10-26	42	Sentinel-1A	442	2016-06-29	82	Sentinel-1B	443	2017-04-19	122	Sentinel-1B	442	2017-12-27
3	Sentinel-1A	442	2014-12-01	43	Sentinel-1A	440	2016-07-11	83	Sentinel-1A	440	2017-04-25	123	Sentinel-1A	442	2018-01-02
4	Sentinel-1A	442	2014-12-25	44	Sentinel-1A	442	2016-07-23	84	Sentinel-1B	443	2017-05-01	124	Sentinel-1B	442	2018-01-08
5	Sentinel-1A	442	2015-01-18	45	Sentinel-1A	440	2016-08-04	85	Sentinel-1A	440	2017-05-07	125	Sentinel-1A	442	2018-01-14
6	Sentinel-1A	442	2015-01-30	46	Sentinel-1A	442	2016-08-16	86	Sentinel-1B	442	2017-05-13	126	Sentinel-1B	442	2018-01-20
7	Sentinel-1A	442	2015-02-23	47	Sentinel-1A	440	2016-09-09	87	Sentinel-1A	440	2017-05-19	127	Sentinel-1A	442	2018-01-26
8	Sentinel-1A	442	2015-03-07	48	Sentinel-1A	440	2016-09-21	88	Sentinel-1B	442	2017-05-25	128	Sentinel-1B	442	2018-02-01
9	Sentinel-1A	442	2015-03-19	49	Sentinel-1B	442	2016-09-27	89	Sentinel-1A	440	2017-05-31	129	Sentinel-1A	442	2018-02-07
10	Sentinel-1A	442	2015-03-31	50	Sentinel-1A	440	2016-10-03	90	Sentinel-1B	440	2017-06-06	130	Sentinel-1B	442	2018-02-13
11	Sentinel-1A	442	2015-04-12	51	Sentinel-1B	442	2016-10-09	91	Sentinel-1A	442	2017-06-12	131	Sentinel-1A	442	2018-02-19
12	Sentinel-1A	442	2015-05-06	52	Sentinel-1A	440	2016-10-15	92	Sentinel-1B	440	2017-06-18	132	Sentinel-1B	442	2018-02-25
13	Sentinel-1A	442	2015-05-18	53	Sentinel-1B	442	2016-10-21	93	Sentinel-1A	442	2017-06-24	133	Sentinel-1A	442	2018-03-03
14	Sentinel-1A	442	2015-05-30	54	Sentinel-1A	440	2016-10-27	94	Sentinel-1B	440	2017-06-30	134	Sentinel-1B	442	2018-03-09
15	Sentinel-1A	443	2015-06-11	55	Sentinel-1B	442	2016-11-02	95	Sentinel-1A	442	2017-07-06	135	Sentinel-1A	442	2018-03-15
16	Sentinel-1A	442	2015-06-23	56	Sentinel-1A	440	2016-11-08	96	Sentinel-1B	440	2017-07-12	136	Sentinel-1B	442	2018-03-21
17	Sentinel-1A	442	2015-07-17	57	Sentinel-1B	442	2016-11-14	97	Sentinel-1B	440	2017-07-24	137	Sentinel-1A	442	2018-03-27
18	Sentinel-1A	442	2015-07-29	58	Sentinel-1A	440	2016-11-20	98	Sentinel-1A	442	2017-07-30	138	Sentinel-1B	442	2018-04-02
19	Sentinel-1A	443	2015-08-22	59	Sentinel-1B	442	2016-11-26	99	Sentinel-1B	440	2017-08-05	139	Sentinel-1A	440	2018-04-08
20	Sentinel-1A	442	2015-09-03	60	Sentinel-1A	440	2016-12-02	100	Sentinel-1A	442	2017-08-11	140	Sentinel-1B	442	2018-04-14
21	Sentinel-1A	442	2015-09-15	61	Sentinel-1B	442	2016-12-08	101	Sentinel-1B	440	2017-08-17	141	Sentinel-1A	440	2018-04-20
22	Sentinel-1A	442	2015-10-21	62	Sentinel-1A	440	2016-12-14	102	Sentinel-1B	440	2017-08-29	142	Sentinel-1B	442	2018-04-26
23	Sentinel-1A	442	2015-11-02	63	Sentinel-1B	442	2016-12-20	103	Sentinel-1A	442	2017-09-04	143	Sentinel-1A	440	2018-05-02
24	Sentinel-1A	442	2015-11-14	64	Sentinel-1A	440	2016-12-26	104	Sentinel-1B	440	2017-09-10	144	Sentinel-1B	442	2018-05-08
25	Sentinel-1A	442	2015-11-26	65	Sentinel-1A	440	2017-01-07	105	Sentinel-1A	442	2017-09-16	145	Sentinel-1A	440	2018-05-14
26	Sentinel-1A	442	2015-12-08	66	Sentinel-1B	443	2017-01-13	106	Sentinel-1B	440	2017-09-22	146	Sentinel-1B	442	2018-05-20
27	Sentinel-1A	442	2015-12-20	67	Sentinel-1A	440	2017-01-19	107	Sentinel-1A	442	2017-09-28	147	Sentinel-1A	440	2018-05-26
28	Sentinel-1A	442	2016-01-01	68	Sentinel-1B	443	2017-01-25	108	Sentinel-1B	440	2017-10-04	148	Sentinel-1B	440	2018-06-01
29	Sentinel-1A	442	2016-01-13	69	Sentinel-1A	440	2017-01-31	109	Sentinel-1A	442	2017-10-10	149	Sentinel-1A	440	2018-06-07
30	Sentinel-1A	442	2016-01-25	70	Sentinel-1B	443	2017-02-06	110	Sentinel-1B	440	2017-10-16	150	Sentinel-1B	443	2018-06-13
31	Sentinel-1A	443	2016-02-06	71	Sentinel-1A	440	2017-02-12	111	Sentinel-1A	442	2017-10-22				
32	Sentinel-1A	442	2016-02-18	72	Sentinel-1B	443	2017-02-18	112	Sentinel-1B	440	2017-10-28				
33	Sentinel-1A	442	2016-03-01	73	Sentinel-1A	440	2017-02-24	113	Sentinel-1A	442	2017-11-03				
34	Sentinel-1A	442	2016-03-13	74	Sentinel-1B	443	2017-03-02	114	Sentinel-1B	440	2017-11-09				
35	Sentinel-1A	443	2016-03-25	75	Sentinel-1A	440	2017-03-08	115	Sentinel-1A	442	2017-11-15				
36	Sentinel-1A	442	2016-04-06	76	Sentinel-1B	443	2017-03-14	116	Sentinel-1B	440	2017-11-21				
37	Sentinel-1A	443	2016-04-18	77	Sentinel-1A	440	2017-03-20	117	Sentinel-1A	442	2017-11-27				
38	Sentinel-1A	442	2016-04-30	78	Sentinel-1B	443	2017-03-26	118	Sentinel-1B	442	2017-12-03				
39	Sentinel-1A	443	2016-05-12	79	Sentinel-1A	440	2017-04-01	119	Sentinel-1A	442	2017-12-09				
40	Sentinel-1A	443	2016-05-24	80	Sentinel-1B	443	2017-04-07	120	Sentinel-1B	442	2017-12-15				